Improvements to the limb scattering stratospheric aerosol record

A Thesis Submitted to the
College of Graduate and Postdoctoral Studies
in Partial Fulfillment of the Requirements
for the degree of Doctor of Philosophy
in the Department of Physics and Engineering Physics
University of Saskatchewan
Saskatoon

By

Landon Rieger

Permission to Use

In presenting this thesis in partial fulfilment of the requirements for a Postgraduate degree from the University of Saskatchewan, I agree that the Libraries of this University may make it freely available for inspection. I further agree that permission for copying of this thesis in any manner, in whole or in part, for scholarly purposes may be granted by the professor or professors who supervised my thesis work or, in their absence, by the Head of the Department or the Dean of the College in which my thesis work was done. It is understood that any copying or publication or use of this thesis or parts thereof for financial gain shall not be allowed without my written permission. It is also understood that due recognition shall be given to me and to the University of Saskatchewan in any scholarly use which may be made of any material in my thesis.

Requests for permission to copy or to make other use of material in this thesis in whole or part should be addressed to:

Head of the Department of Physics and Engineering Physics
Department of Physics and Engineering Physics
University of Saskatchewan
Physics Building, 116 Science Place
Saskatoon, Saskatchewan S7N 5E2
Canada

Dean
College of Graduate and Postdoctoral Studies
University of Saskatchewan
116 Thorvaldson Building, 110 Science Place
Saskatoon, Saskatchewan S7N 5C9
Canada

Abstract

In the last decade stratospheric aerosols have gained considerable attention due to the influence of a series of moderate volcanic eruptions. The eruptions have been explosive enough to inject aerosols and precursors into the stratosphere and cause minor but important radiative and chemical effects, impacting projections and modelling of the global climate. Improved understanding of these effects requires accurate measurements of aerosol levels at spatial and temporal scales that resolve the rapidly changing conditions after events such as volcanic eruptions while also providing global information. This has been enabled by the advent of satellite profiling observations beginning in the 1980s that are able to produce global, vertically resolved measurements of stratospheric aerosols. These records have helped improve estimates of radiative forcing but remain uncertain in key aspects, including the magnitude of the biases between different measurement systems, errors in records due to retrieval assumptions, and aerosol levels in the upper troposphere and lower stratosphere. This work quantifies and addresses these limitations using three studies.

First, biases are explored between the two longest satellite-based stratospheric aerosol records: SAGE II from 1984-2005 and OSIRIS from 2001-present. Biases are found to be relatively small, approximately 10%, in the majority of the stratosphere, and a merged aerosol record spanning 35 years is produced by adjusting for these measurement biases. This work produced an aerosol climatology suitable for use in climate models, but did not determine the reasons for the biases. The second study compares two instruments and their retrievals, OSIRIS and SCIAMACHY, to investigate the major sources of error. It is found that errors in the a priori assumptions including particle size and the aerosol profile at high altitudes cause the majority of biases, while differences in the retrieval techniques and the radiative transfer models have mostly negligible impacts. The final study uses these results to develop a new multi-wavelength retrieval for OSIRIS measurements that aims to minimize the errors from a priori assumptions and improve retrieval sensitivity in the upper troposphere and lower stratosphere. This is used to produce the publicly available version 7 OSIRIS aerosol product, and is validated using comparisons with SAGE measurements as well as satellite lidar observations. Significant reductions in particle size biases are found with this new

algorithm, and an updated cloud filter allows for retrievals at lower altitudes than previously possible.

Acknowledgements

I would like to extend my sincerest thanks to my advisors, Drs. Adam Bourassa and Doug Degenstein. Their knowledge and insights have provided invaluable guidance on this work, and I am deeply appreciative of their patience and support throughout not only my PhD, but my entire time at the University of Saskatchewan. Additionally, they have put together a remarkable group of students and researchers to whom I also owe a debt of gratitude. The members of 312 have acted as sounding board, teacher, and source of genuine enjoyment during this work and have made it a great place to work.

My time at IUP was both productive and illuminating in regards to many aspects of this work, and credit for this goes to Drs. Alexei Rozanov, John P. Burrows and the other graduate students there. While their insights helped this work tremendously, I would also like to thank them for their hospitality that made me feel at home in Bremen. In particular, I would like to thank Elizaveta Malinina, who tolerated long and occasionally even fruitful discussions on limb scattering, and made the second paper of this work possible.

Lastly, I would like to thank my family and friends, who have provided their support throughout this work and diversions when needed most.

For Liza,

who has motivated me, supported me, and inspired me, and with whom I now write the next chapter.

Contents

List of Tables

List of Figures

List of Abbreviations

AERONET	AErosol RObotic NETwork
AOD	Aerosol Optical Depth
BRDF	bidirectional Reflectance Distribution Function
CALIPSO	Cloud-Aerosol Lidar and Infrared Pathfinder Satellite Observation
CALIPSO-GOCCP	GCM Oriented Cloud CALIPSO Product
CLAES	Cryogenic Limb Array Etalon Spectrometer
ECMWF	European Center for Medium-range Weather Forecasting
FWHM	Full Width at Half Maximum
GloSSAC	Global Space-based Stratospheric Aerosol Climatology
GOMOS	Global Ozone Monitoring by Occultation of Stars
GP	Garmisch-Partenkirchen
HALOE	Halogen Occultation Experiment
IUP	Institute of Environmental Physics
MART	Multiplicative Algebraic Reconstruction Technique
MERRA	Modern-Era Retrospective analysis for Research and Applications
MLO	Mauno Loa Observatory
NCEP	National Center for Environmental Prediction
OHP	Observatoire de Haute-Provence
OMPS-LP	Ozone Mapping and Profiler Suite - Limb Profiler
OPC	Optical Particle Counter
OSIRIS	Optical Spectrograph and InfraRed Imaging System
PALMS	Particle Analysis by Laser Mass Spectrometry
PSC	Polar Stratospheric Clouds
SAGE	Stratospheric Aerosol and Gas Experiment
SAM	Stratopsheric Aerosol Measurement
SCIAMACHY	SCanning Imaging Absorption SpectroMeter for Atmospheric CHartographY
SOFIE	Solar Occulation For Ice Experiment
SSA	Single Scattering Angle
SZA	Solar Zenith Angle
UTLS	Upper Troposphere and Lower Stratopshere

Chapter 1

Introduction

The term *aerosol* encompasses a wide range of particles with different sources, compositions, and life cycles. Solid particulate from oceans, deserts, and biomass burning mix with liquid droplets of water, acid, and organic constituents to create complex compositions that result in a wide array of chemical reactions. Despite comprising a miniscule fraction of the total atmosphere they play a prominent role in Earth's climate, interacting both chemically and radiatively and affecting everything from temperature to human health. Generally, these aerosols are relatively short-lived in the atmosphere, being scavenged by clouds and rain, and sedimenting out due to weather and the rapid overturning of the troposphere. However, particles reaching the much more stable stratosphere can persist for months or years, multiplying their potential impacts.

While stratospheric aerosols are only a small subset of aerosols in the atmosphere, they play an important role in Earth's climate, scattering light away from Earth to create a cooling effect, and enhancing ozone loss. Understanding the climate therefore requires accurate knowledge of aerosols and necessitates global measurements only possible with satellite measurements. While crucial in realizing the extent of stratospheric aerosols, remote measurements from satellites instruments are inherently complicated. Partly, this is due to the broad spectral signature and the large number of microphysical unknowns that make the measurements fundamentally different from most trace gas retrievals such as ozone, and partly it is due to the inherent complexity of the signals measured that depend not only on aerosol concentration but a multitude of additional parameters.

Despite the difficulties, high quality, satellite-based global records have emerged, and play an integral role in refining and quantifying the global climatic impact of stratospheric aerosols. Broadly, this work seeks to extend and improve the current satellite records, in particular

from measurements of limb scattered sunlight spectra. This technique has provided leading aerosol datasets since 2001, and remains an essential method going forward. To lay the basis for work presented in this thesis, Chapter 2 discusses the relevant background information, beginning with general information about stratospheric aerosols, their properties, and the major sources, sinks, and dynamical processes that influence them. Interpreting remote aerosol measurements requires understanding of the radiative processes involved, and this is discussed in Section 2.2. The most prevalent satellite aerosol records and measurement techniques are then presented in Section 2.3. Lastly, Chapter 2 provides an overview of the mathematical techniques used to derive aerosol properties from the observations.

The remainder of this work is composed of three published papers, with an introduction to each to provide context in the broader scope of this work. The first, contained in Chapter 3, investigates the possibility of merging the OSIRIS limb scattering aerosol record with the long-standing occultation record of SAGE II. This work was directly instigated by work in climate modelling that required improved measurements that extended past the occultation records up to the current day, and this work aims to provide a long-term continuous aerosol record to that end. The second paper, presented as Chapter 4 here, investigates deficiencies in the current limb scattering aerosol records through simulation studies and comparison between two independent datasets. This work helped to improve understanding of the major biases in the retrievals, and led directly to the third paper which focuses on improving the OSIRIS record by reducing a major cause of these biases. Chapter 5 is the final paper which develops and analyzes a new limb scattering retrieval algorithm and applies it to the OSIRIS observations. The new retrieval is designed to minimize biases from a priori assumptions and increase sensitivity at lower altitudes and these improvements are tested through comparisons to other satellites measurements. The final chapter discusses the impact of this work, and questions that remain unanswered.

Chapter 2

Background

2.1 Stratospheric Aerosol

In late 1959 and 1960 a series of balloon launches discovered the presence of a ubiquitous layer of submicron sized particles in the 12 to 25 km altitude range (Junge *et al.,* 1961; Chagnon *et al.,* 1961). Analysis determined the composition to be primarily sulfur compounds in a liquid state, and many subsequent in situ measurements have confirmed the presence and composition of what has come to be known as the Junge layer. Although Chagnon *et al.* (1961) commented on the remarkable stability of the layer over their year long campaign, later measurements have shown that the background state can be punctuated by large injections from volcanic eruptions and other sources. For example, in June 1991 Mount Pinatubo erupted, injecting approximately 10 Tg of sulfur into the stratosphere and elevating aerosol levels by over a factor of ten from background conditions (Guo *et al.,* 2004). However, much smaller eruptions can also reach the stratosphere with noticeable impacts, and over the last decade several minor eruptions have been the focus of intense study (Bourassa *et al.,* 2010; Vernier *et al.,* 2011; Solomon *et al.,* 2011; Bourassa *et al.,* 2012b; Santer *et al.,* 2014; Andersson *et al.,* 2015; Vernier *et al.,* 2016, e.g.). The climate impact of stratospheric aerosols is dictated by many factors including the chemical composition, concentration, and dynamical and microphysical processes that lead to distribution and removal. This section discusses these impacts and the basics of formation and distribution of aerosols in the stratosphere that lead to them.

2.1.1 Aerosol Microphysics

Stratospheric aerosol makeup comes from mostly two sources: large scale exchange processes with the troposphere which brings aerosol precursors into the stratosphere, and explosive volcanic eruptions that inject aerosol particles and sulfur compounds directly to high altitudes (Holton *et al.,* 1995; Robock, 2000). In both cases the majority of stratospheric aerosols are liquid droplets composed of approximately 25% water and 75% sulfuric acid (Rosen, 1971; Carslaw *et al.,* 1995). The primary precursor gases are carbonyl sulfide (OCS) and sulfur dioxide (SO_2) that enter the stratosphere from the tropical tropopause region through vertical and isentropic transport to higher latitudes (Brock *et al.,* 1995; Fueglistaler *et al.,* 2009). OCS is produced in the oceans with secondary anthropogenic and soil emissions and is the largest reservoir of sulfur in the stratosphere due its long lifetime. After reaching the stratosphere it is converted to SO_2 by photolysis and molecular oxygen and provides about half the sulfur that is converted to aerosols (Sheng *et al.,* 2015). Although a much smaller reservoir, sulfur dioxide also contributes approximately half of the sulfur for stratospheric aerosol, even during volcanically quiescent periods. Produced by anthropogenic emissions and continually outgassing volcanic vents, SO_2 is primarily converted to sulfuric acid through the reactions:

$$\begin{aligned} SO_2 + OH &\longrightarrow HSO_3 \\ HSO_3 + O_2 + M &\longrightarrow SO_3 + HO_2 \\ SO_3 + H_2O &\longrightarrow H_2SO_4 \end{aligned} \tag{2.1}$$

The microphysical properties of stratospheric aerosols are governed by the chemical makeup of the stratosphere as well as the processes of condensation, coagulation, evaporation and sedimentation. The vapour pressure in the stratosphere is generally insufficient for H_2SO_4 to nucleate homogenously with other H_2SO_4 and H_2O molecules (Hamill *et al.,* 1982). However, meteoritic particles and ions are also abundant in the stratosphere and provide sites for heterogeneous nucleation (Curtius *et al.,* 2005). The supersaturation supports condensational growth of the particles until approximately 35 km where temperatures and pressures favour evaporation. As particles grow through condensation and coagulation, sedimentation plays an increasingly important role, removing the largest droplets (Hamill *et al.,* 1977).

Together, these processes create a complex array of particle sizes that can vary with altitude, latitude and time. Early work often assumed particles followed a gamma distribution, and some recent work has used this assumption as well (Chen *et al.,* 2018). However, the assumption of a lognormal size distribution has become the norm and continues to dominate the field. Lognormal distributions have the form

$$\frac{dn(r)}{dr} = \frac{N}{r\ln(\sigma_g)\sqrt{2\pi}} \exp\left(-\frac{(\ln r - \ln r_g)^2}{2\ln(\sigma_g)^2}\right), \tag{2.2}$$

where r is the particle radius, r_g is the median radius, σ, is the width and N is the number concentration. There is some theoretical basis to predict a lognormal distribution of particle sizes (Granqvist *et al.,* 1976; Kiss *et al.,* 1999), but most evidence in the stratosphere relies on in situ particle measurements from high altitude balloons. The most extensive of these records uses Optical Particle Counters (OPC) to measure particles in 6-10 size bins and now includes over 100 launches spanning over 40 years (Deshler *et al.,* 2003). These measurements are fit using a lognormal distribution, or when applicable a combination of two lognormal distributions, as is sometimes the case after large volcanic eruptions. An example OPC measurement from 19.5 km on October 21, 2008 is shown in Figure 2.1. The orange points indicate the number of particles measured with radii larger than r, and the solid line indicates the cumulative lognormal distribution fit to the measurements. The shaded region shows the retrieved lognormal distribution. While the lognormal distribution generally provides a good fit to the available data, measurements of particles with radii below 150 nm are extremely limited, and Poisson counting errors of large particles limit the ability to verify the accuracy of the lognormal assumption.

Recent aircraft campaigns have made detailed analyses of aerosol particles in the upper troposphere and lower stratosphere, or UTLS, and have painted a more complex picture of the chemical makeup. Particle Analysis by Laser Mass Spectrometry (PALMS) measurements have shown that near the tropopause a large fraction of the aerosols can include organic matter as well as sulfuric acid and water (Murphy *et al.,* 2007). Sulfur-organic mixes including soot, bromine, iodine and ammonium comprise most of the total particle mass near the tropopause. While the concentration of non-sulfuric components decreases rapidly with height, these particles can be an important component of the total aerosol loading in the

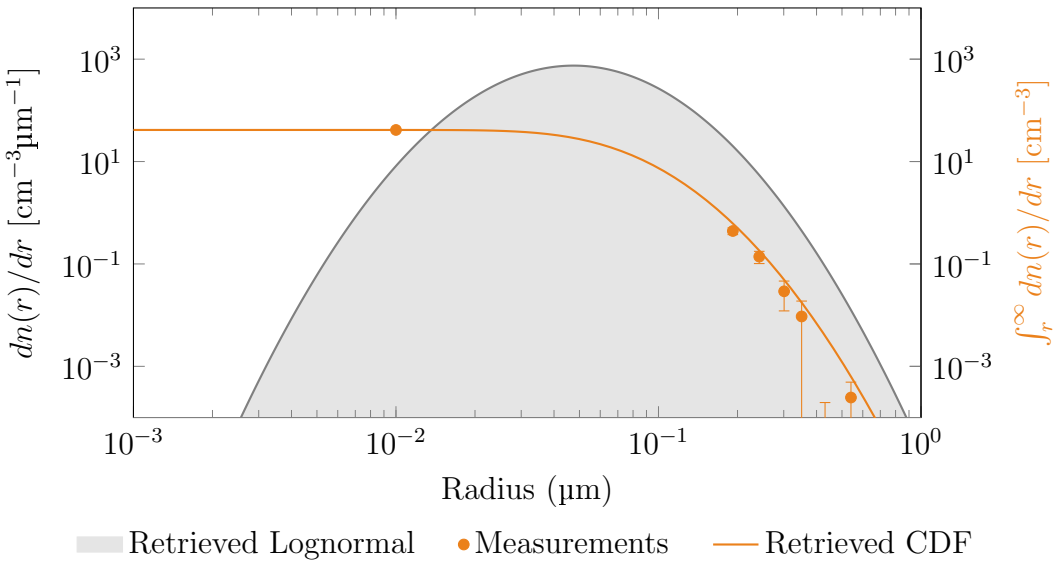

Figure 2.1: Lognormal size distributions fit to optical particle counter measurements for a measurement at 19.5 km altitude from October 2008. The gray line shows the differential fine mode distribution and the black line the differential coarse mode distribution, both assumed to be lognormal. Figure recreated from Deshler *et al.* (2003).

UTLS, especially in the mid-to high latitudes where isentropic mixing from the tropics can incorporate tropospheric material (Murphy *et al.,* 2014). Some volcanic eruptions can also inject ash particles into the stratosphere (Vernier *et al.,* 2016), further complicating composition assumptions. Although balloon and aircraft measurements have provided an invaluable dataset of microphysical properties, the measurements are inherently limited in number with a few measurements per year at a handful of locations. To produce a global picture of aerosols requires the use of remote sensing techniques from satellite platforms.

2.1.2 Climate Effects

Broadly, the impact of stratospheric aerosols on the climate can be broken into two categories: direct impacts on the Earth's radiative budget caused by the increase in scattering and absorption by aerosol particles, and indirect effects precipitated by the interaction of aerosols with clouds, ozone chemistry and land changes.

Aerosols play an important role in the radiative forcing of the atmosphere with several competing effects. Directly, aerosols scatter sunlight, increasing Earth's albedo and reducing warming of the surface (Lacis *et al.,* 1992). Aerosols also absorb and emit upwelling infrared

radiation, leading to warming that partially offsets the cooling effects (Kiehl *et al.,* 1993). The radiative forcing produced by these effects is relatively small and negative when aerosols are at low, background levels (Solomon *et al.,* 2011; Schmidt *et al.,* 2018). However, large amplifications of the background level occur during volcanically active periods, such as that produced by the eruption of Mt. Pinatubo in 1991. Pinatubo injected approximately 20 million tons of SO_2 into the stratosphere and the effect was a global cooling of approximately 0.5°C near the surface and a heating of the stratosphere by more than 2°C for months following the eruption (McCormick *et al.,* 1995; Robock, 2000). The lifetime of these volcanically active periods is also quite long, with the aerosols taking years to return to background levels.

Following the Mt. Pinatubo eruption stratospheric intrusions were remarkably limited, and stratospheric aerosol relaxed to its lowest measured levels until Mount Ruang marked the start of a series of smaller eruptions in 2002. Despite the much smaller magnitude of these eruptions, they have been large enough to penetrate the tropopause, injecting SO_2 into the stratosphere, and have steadily increased the level of aerosol over background conditions (Vernier *et al.,* 2011). Due to the smaller magnitude, the effect of these smaller eruptions is not as clear, but multiple studies have indicated a modest impact that should not be ignored in climate models (Solomon *et al.,* 2011; Fyfe *et al.,* 2013a; Haywood *et al.,* 2014). In response to the climate effects seen after volcanic eruptions, geo-engineering schemes have been proposed which use large amounts of SO_2 injected into the stratosphere to help offset global warming (Rasch *et al.,* 2008b; Govindasamy *et al.,* 2003; Wigley, 2006; Rasch *et al.,* 2008a). This has further stimulated the study of anthropogenic emissions and smaller volcanic eruptions.

In addition to direct radiative processes, stratospheric aerosols can influence several responses that affect the forcing estimates. One of the most important feedback mechanisms for radiative forcing is aerosols' effect on cloud formation and growth (Boucher *et al.,* 2013). As aerosols sediment out of the stratosphere and into the troposphere they affect cloud droplet composition through numerous pathways, including acting as nucleation sites to favour smaller droplets and whiter clouds that reflect more radiation but also changes the lifetime of the droplets (Lohmann *et al.,* 2005). Additionally, aerosols heat the UTLS region, decreasing homogeneous nucleation rates of cirrus clouds. This potentially leads to thinner

cirrus clouds, and Kuebbeler *et al.* (2012) found that the increased emittance of long-wave radiation dominated over the decreased reflectance of shortwave radiation, causing an overall cooling effect. While the above studies have estimated the impacts on cloud-aerosol interactions, the error bars remain relatively large due to the inherent difficulty of cloud simulations (Haerter *et al.,* 2009; Fan *et al.,* 2016).

Stratospheric aerosols also provide a surface for heterogeneous chemistry, leading to increased ozone and NO_x loss. In particular, the polar vortex allows temperatures to drop low enough for HNO_3 to condense onto existing sulfuric acid particles, leading to the reaction

$$HCl + ClONO_2 \rightarrow HNO_3 + Cl_2 \tag{2.3}$$

This frees Cl_2 to be photolyzed into ozone destroying Cl, while at the same time trapping NO_2 that would aid in the removal of Cl (Solomon *et al.,* 1986). This reduces the UV radiation absorbed at higher altitudes and changes the temperature profile of the stratosphere, inducing circulation changes as well as direct heating effects (Tilmes *et al.,* 2009; Heckendorn *et al.,* 2009). Although the ozone effect is relatively small in terms of radiative forcing, at -0.1 W/m^2, the UV-B concentration can increase by 10 % at the surface at high latitudes (Pitari *et al.,* 2014). In addition to atmospheric coupling, aerosols can also couple to land cover changes. Stratospheric aerosols affect the radiation at lower altitudes, increasing diffuse light while decreasing direct solar radiation. This increases plant growth, reducing atmospheric CO_2 and resulting in a cooling effect (Mercado *et al.,* 2009). While this effect is not expected to be large after small or moderate eruptions, it has been experimentally observed after large eruptions such as Pinatubo (Gu *et al.,* 2003).

Better understanding and quantifying these effects requires improved models, but also high quality, global aerosol measurements that have been the goal of a range of space-based techniques. However, to understand the remote sensing measurements, as well as their advantages and limitations, requires a small diversion into radiative transfer theory, which is the focus of the next section.

2.2 Radiative Transfer

Propagation of radiation through various media has long been the focus of intense study, and the general problem of radiative transfer has been applied to a wide variety of fields. The difficulty of solving Maxwell's equations directly for a complicated system has meant each field generally relies on a series of approximations applicable to their respective problem, with heuristic arguments and definitions convenient to the particular field. The following section describes the scattering and absorption mechanisms that dominate radiative interactions at solar wavelengths, in particular those relevant for stratospheric aerosols. While emission events can be important at infrared wavelengths, only optical measurements are considered in this work, and so emission processes are omitted in the following discussion.

2.2.1 The Radiative Transfer Equation

In atmospheric science a common measurement is the intensity of the electric field, or *irradiance*, defined as the radiative power per unit area. If directional information is included, this is known as the *radiance*, the irradiance per unit solid angle. Additionally, spectral information is often incorporated in the measurements, yielding the common unit of *spectral radiance*. For a surface this is defined as

$$I = \frac{\partial \mathcal{E}}{\partial \Omega \partial \lambda \partial A \cos(\theta) \partial t}, \tag{2.4}$$

where $\mathcal{E}$ is the energy, Ω is the solid angle, λ the wavelength, and $A\cos(\theta)$ is the projected area. Measurements of radiance lend themselves well to a description of the electric field in terms of the stokes vector,

$$\vec{I}(\vec{r}, \hat{n}) = \begin{pmatrix} I(\vec{r}, \hat{n}) \\ Q(\vec{r}, \hat{n}) \\ U(\vec{r}, \hat{n}) \\ V(\vec{r}, \hat{n}) \end{pmatrix}. \tag{2.5}$$

If an electric field, $\mathbf{E}$, is propagating orthogonal to the x and y directions, then the first element of the stokes vector, I, is the total intensity

$$I = |E_x|^2 + |E_y|^2. \tag{2.6}$$

The remaining three elements are described by the prevalence of different polarized components,

$$\begin{aligned} Q &= |E_x|^2 - |E_y|^2 \\ U &= 2\mathrm{Re}(E_x E_y^*) \\ V &= -2i\mathrm{Re}(E_x E_y^*). \end{aligned} \tag{2.7}$$

$\vec{I}$ is a function of both position, $\vec{r}$, and direction, $\hat{n}$. One of the simplest events to consider is scattering by a single particle, as in Figure 2.2.

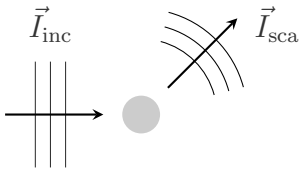

Figure 2.2: Graphical depiction of scattering by a single particle.

If an incoming plane wave, $\vec{I}_{\mathrm{inc}}$, in the direction, n_{inc}, interacts with the particle, then at sufficient distance the scattered radiation in direction, n_{sca}, is a spherical wave and the scattering process can be represented as,

$$\vec{I}_{\mathrm{sca}} = \frac{1}{r^2}\mathbf{Z}(\hat{n}_{\mathrm{inc}}, \hat{n}_{\mathrm{sca}})\vec{I}_{\mathrm{inc}} \tag{2.8}$$

where $\vec{I}_{\mathrm{sca}}$ is the spectral radiance of the scattered radiation, and $\mathbf{Z}$ is the 4×4 scattering matrix that describes the transformation and depends on both the incoming and outgoing direction. If an observer is directly behind the object with respect to the incoming plane wave, then in addition to the scattered light the incoming wave and its attenuation must also be accounted for. The 4×4 extinction matrix, $\mathbf{K}(\hat{n}_{\mathrm{inc}})$, describes how each element of the Stokes vector is attenuated and transformed by the particle, and in the exact forward scattering case, where $\hat{n} = \hat{n}_{\mathrm{inc}}$, the spectral radiance is

$$\vec{I}_{\mathrm{obs}}(\vec{r}, \hat{n}) = \vec{I}_{\mathrm{inc}} + \frac{1}{r^2}\mathbf{Z}(\hat{n}, \hat{n})\vec{I}_{\mathrm{inc}} - \mathbf{K}(\vec{r}_i, \hat{n})\vec{I}_{\mathrm{inc}}. \tag{2.9}$$

If many particles are present then in addition to the individual scattered fields, the interactions of the scattered fields must also be accounted for. Computing this interaction, also known as *multiple scattering*, can quickly become infeasible, even for numerical approaches,

as the number of particles grows. Mishchenko (2002) derived a method where a macroscopic approach is taken and a collection of particles are analyzed in a statistical framework. To aid in the solution the position and orientation of the particles are assumed to be uncorrelated and several approximations are made that greatly simplify the problem. First, it is assumed that particles are sufficiently rarefied that scattering occurs only in the far-field regime. This allows each scatterer to be treated as a point source with a spherical outgoing wave. Second, when computing the scattered field from a particle, it is assumed that the particle does not affect the incoming radiation field, also known as the Twersky approximation (Twersky, 1964). This has the geometric interpretation that light rays do not scatter off of the same particle more than once. Lastly, it is assumed that the particles are randomly positioned within the scattering volume, and that averaging is done over a sufficiently long time period that all particle states are sampled.

With these assumptions, it is possible to write a closed form of the scattering by a collection of particles with an average number density, n. The radiative transfer equation (RTE) describing the time-averaged stokes vector is

$$\hat{n} \cdot \nabla \vec{I}(\vec{r}, \hat{n}) = -n\mathbf{K}(\vec{r}, \hat{n})\vec{I}(\vec{r}, \hat{n}) + n \int \mathbf{Z}(\vec{r}, \hat{n}', \hat{n})\vec{I}(\vec{r}, \hat{n}')d\hat{n}' + n\mathbf{Z}(\vec{r}, \hat{n}_{\text{inc}}, \hat{n})\vec{I}_{\text{inc}}(\vec{r}), \quad (2.10)$$

The first term on the right side describes how much radiation is removed from the line of sight by scattering and absorption. The second term integrates the incoming diffuse radiation from all directions $\hat{n}'$ that is scattered into the direction $\hat{n}$ over all solid angles. The final term is the single scattered contribution from the attenuated incoming beam.

2.2.2 Simplifications and a Phenomenological Approach

Derivation of the vector radiative transfer equation from fundamental laws illuminates the assumptions implicit in Equation 2.10, but it was only relatively recently that this was accomplished. Previously, derivation relied on phenomenological arguments, that while not as rigorous, do provide some insight into the underlying processes, and underpin much of the nomenclature and analysis of earlier measurement systems, and is therefore worth exploring briefly. The classic derivation generally begins with a pencil of radiation impinging on an infinitesimally thin slice of material that causes some scattering and absorption, as in Figure

2.3. For this analysis polarization is typically ignored and the spectral radiance is treated as the scalar field, I. Similarly, the extinction matrix, $\mathbf{K}$ is often assumed to be independent of direction and taken to be the first element of the matrix, K_{11}. This quantity is often referred to as the optical cross section, or simply cross section, σ, and has units of area. The cross section is often broken into separate components, σ_{sca}, which reflects the probability of light scattering off of the particle, and σ_{abs} which indicates the probability of light being absorbed. The total, or extinction cross section, σ, is then the sum of the two components. While these scalar assumptions are generally acceptable for measurements of the total intensity in typical atmospheric settings, it cannot always be ignored for systems that include polarization information, such as some lidars, as discussed later.

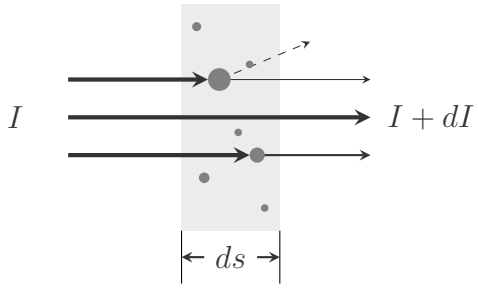

Figure 2.3: Graphical depiction of the attenuation and scattering of an incoming beam of light as it interacts with an infinitesimally thin medium.

As the beam of radiation interacts with the medium, the change in intensity is assumed to be proportional to the density of particles, n, their cross section, and the incoming radiance. The linear differential equation describing the attenuation is then,

$$\frac{dI}{ds} = -n\sigma I. \tag{2.11}$$

The number density and cross section together define the *extinction*

$$k = n\sigma,$$

which indicates the relative change in intensity per unit path length. Solving 2.11, the radiance is exponentially attenuated when passing through a uniform medium as,

$$I = I_{\text{inc}} e^{-n\sigma s}, \tag{2.12}$$

where s is the path length through the medium and I_{inc} is the intensity of the incoming beam. This is commonly written as

$$I = I_{\text{inc}} e^{-\tau}, \tag{2.13}$$

where τ is the *optical depth* of the medium along the path. If more than one type of particle is present, then the optical depth is the sum over each species,

$$\tau = \sum_i n_i \sigma_i s. \tag{2.14}$$

Typically, the number density and optical properties may vary throughout the medium, so properties such as the optical depth must be integrated along the path as

$$\tau(s_0, s_1) = \int_{s_0}^{s_1} n(s)\sigma(s) ds. \tag{2.15}$$

In addition to light being scattered out of the observer line of sight, it may also be scattered into it. This is accounted for by incorporating an additional source of radiation, J, in Equation 2.11, as

$$\frac{dI}{ds} = -n\sigma I + J. \tag{2.16}$$

The source term, J, is the sum of any diffuse incoming light over all angles, I_{diff}, scattered into the line of sight direction,

$$J(\hat{n}) = k_{\text{sca}} \int_{4\pi} I_{\text{diff}}(\hat{n}') p(\hat{n}', \hat{n}) d\hat{n}', \tag{2.17}$$

where p is the phase function describing the probability of light being scattered from direction $\hat{n}'$ into direction $\hat{n}$. The phase function is normalized such that the integral over all angles is equal to 4π,

$$\frac{1}{4\pi} \int_{\Omega} p(\hat{n}', \hat{n}) d\hat{n}' = 1. \tag{2.18}$$

If a volume of particles is to be considered, then radiation sources and attenuation must be integrated along the observer line of sight, $\vec{s}$, that passes through the volume, as shown in Figure 2.4. Note that because a single path through the medium is defined, the position along the path, s defines both the position, $\vec{r}$, and direction, $\hat{n}$. Integrating along the path, yields the spectral radiance as seen by the observer at s_1 as

$$I(s_1) = I(s_0) e^{-\tau(s_0, s_1)} + \int_{s_0}^{s_1} J(s) e^{-\tau(s, s_1)} ds. \tag{2.19}$$

Equation 2.19 is the scalar analogue of Equation 2.10.

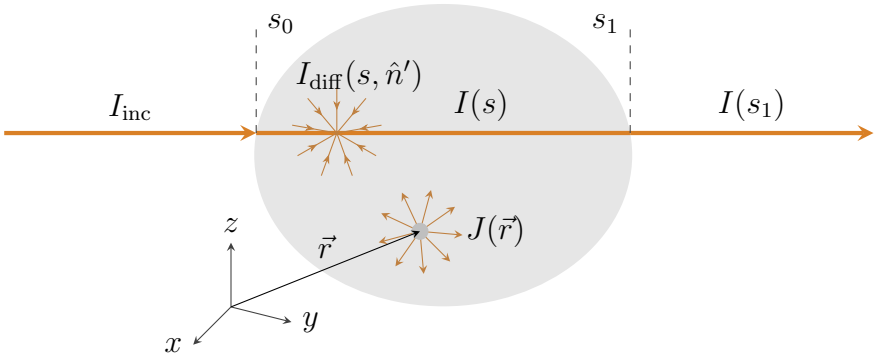

Figure 2.4: Graphical depiction of the integration performed along the line of sight.

2.2.3 Radiative Transfer Models

Simulating radiation in Earth's atmosphere is computationally a very expensive task, and many codes exist to solve the radiative transfer equation using a variety of approaches. The main difficulty arises from the diffuse scattering term, I_{diff}, in Equation 2.17 which requires solving the equation at all points in the atmosphere. One common approach is the method of successive order, where the radiation field arising from light scattered once is first computed, this in turn is used to generate the field from the radiation that has scattered twice, and so on (Chandrasekhar, 1960). Assuming a scalar radiance, the singly scattered source, J_{ss} is given by

$$\vec{J}_{\text{ss}}(s, \hat{n}) = F_{\text{sun}} k_{\text{sca}}(\vec{r}) p(\vec{r}, \Theta) e^{-\tau(\text{sun}, \vec{r})}, \tag{2.20}$$

where the solar irradiance, F_{sun}, is attenuated from the source to the point $\vec{r}$ and scattered. The single scattered radiance, I_{ss} as seen by an observer looking through the atmosphere is then given by

$$I_{\text{ss}}(s_1) = I(s_0) e^{-\tau(s_0, s_1)} + \int_{s_0}^{s_1} F_{\text{sun}} k_{\text{sca}}(\vec{r}) p(\vec{r}, \Theta) e^{-\tau(\text{sun}, \vec{r})} e^{-\tau(s, s_1)} ds.. \tag{2.21}$$

This serves as the initial value to compute the higher orders of scatter.

If the path, $\vec{s}$ intersects the Earth's surface then the outgoing radiance from the surface, $I(\hat{n}_{s_0})$, is determined from computing the scattered component over all incoming directions as

$$I(\hat{n}_{\text{out}}) = \int_{2\pi} I(\hat{n}_{\text{inc}}) f(\hat{n}_{\text{out}}, \hat{n}_{\text{inc}}) d\hat{n}_{\text{inc}}, \tag{2.22}$$

where f is the bidirectional reflectance distribution function (BRDF) that describes how the surface reflects light. Earth's surface is often modelled as Lambertian, which states that the reflectance of a surface is proportional to the cosine of the angle from the surface normal and results in the brightness of a surface being independent of viewing angle. In this case the BRDF is

$$f_{\text{lambertian}} = \frac{a}{\pi}, \tag{2.23}$$

where a is a scalar value between 0 and 1. The observed single scattered radiance from a Lambertian surface is

$$I(\vec{r}) = \frac{a}{\pi} F_{\text{sun}}(\hat{n}') \cos(\theta_{\text{SZA}}) e^{-\tau(\text{sun},\vec{r})}, \tag{2.24}$$

where θ_{SZA} is the solar zenith angle, the angle between surface normal and the incoming solar irradiance.

A second approach is to use Monte-Carlo methods to solve the radiative transfer equation, simulating large numbers of individual photon interactions as they propagate through the medium (Metropolis *et al.,* 1949). This technique has the advantage that scattering events are not calculated on a discretized grid, leading to potentially more accurate solutions. However, while often used as benchmark for successive order algorithms, this method is generally far more computationally expensive, so is not typically used on an operational basis. The radiative transfer model used most extensively in this work is SASKTRAN (Bourassa *et al.,* 2008; Zawada *et al.,* 2015; Zawada *et al.,* 2017). Both a successive orders and Monte-Carlo solver are included with SASKTRAN, although this work uses only the successive orders method.

2.2.4 Aerosol Optical Properties.

The aerosol component of a remote sensing signal propagates through Equation 2.10 via the aerosol number density, phase function and cross section values. This section explores the optical properties of typical stratospheric aerosol compositions and their impact on potential measurements. Generally, stratospheric aerosols have very little absorption in the visible and near infrared wavelengths, so ozone and NO_2 are much more important for radiative transfer considerations in terms of absorption. Although exceptions to this can occur when

ash from volcanoes (Vernier *et al.,* 2016) or soot from forest fires (Haarig *et al.,* 2018) enters the stratosphere. Figure 2.5 shows the index of refraction for a typical sulfur composition of stratospheric aerosols. Absorption only becomes important past approximately 2 microns.

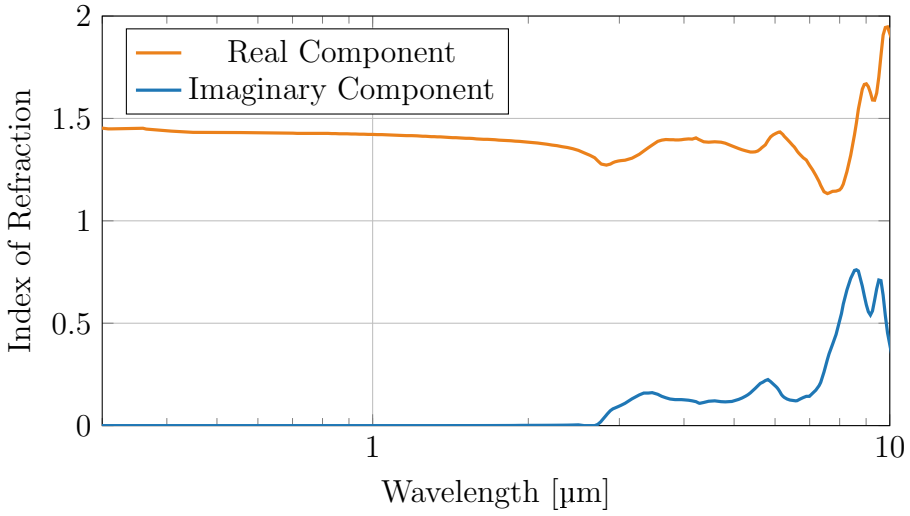

Figure 2.5: Index of refraction for a 75/25 mix of H_2SO_4 and H_2O. Data from Palmer *et al.* (1975).

At visible wavelengths the aerosol signal is dominated by scattering rather than absorption with the scattering cross section depending very strongly on the particle's *size parameter*, x, defined as,

$$x = \frac{2\pi r}{\lambda}, \tag{2.25}$$

where r is the particle radius and λ is the radiation wavelength. The cross section for a range of spherical particles is shown in Figure 2.6. For small particles with a size parameter $\ll 1$ the cross section scales with r^6, and with λ^{-4}. For larger, spherical particles, the scattering and absorption properties can be determined from Mie theory (Mie, 1908). In this region, resonances become apparent and the cross section no longer monotonically increases with the size parameter. If a collection of particles is present, then the average cross section is weighted by the number of particles at each size as

$$\bar{\sigma} = \frac{\int_0^\infty \sigma(r)\frac{dn}{dr}dr}{\int_0^\infty \frac{dn}{dr}dr}. \tag{2.26}$$

For arbitrarily shaped particles, scattering can depend on both the incoming and outgoing direction relative to the orientation of the particle. For atmospheric applications this can be

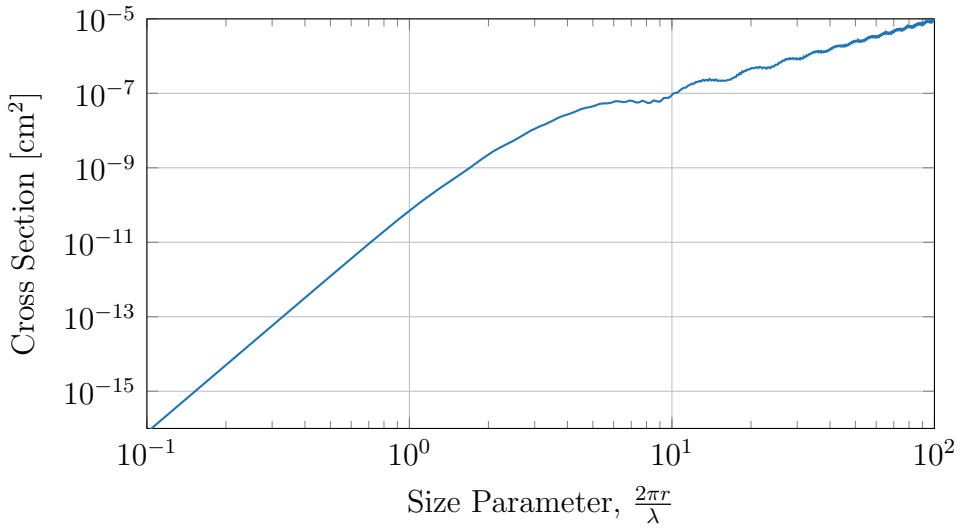

Figure 2.6: Scattering cross section as a function of the particle size parameter for particles with a real index of refraction of 1.44 and no absorption.

important when considering scattering by non-randomly oriented ice particles, but is rarely important in the stratosphere, where temperatures and compositions typically yield spherical particles. In this case, the scattering is symmetric about the incoming propagation direction, and the outgoing intensity depends only on the angle between the incoming and outgoing directions. The phase function can then be expressed as a function of the scattering angle, Θ, where,

$$\Theta = \cos^{-1}\left(\frac{\vec{r}_{\text{inc}} \cdot \vec{r}_{\text{sca}}}{||\vec{r}_{\text{inc}}||||\vec{r}_{\text{sca}}||}\right). \tag{2.27}$$

When the wavelength of radiation being considered is much longer than the radius of the particle, scattering of light is relatively isotropic, and the phase function is given by

$$p(\Theta) = \frac{3}{4}\left(1 + \cos^2(\Theta)\right). \tag{2.28}$$

This Rayleigh phase function describes the case of molecular scattering by air and is shown as the black curve in Figure 2.7. Larger particles scatter light much less isotropically, with strong forward scattering peaks and backscattering resonances. As an example, the phase function at a wavelength of 750 nm for a particle radius of 500 nm is shown in orange. If a collection of particles with different sizes exists, as is typically the case in the stratosphere, then the phase function is the extinction-weighted average over the particles,

$$\bar{p}(\Theta) = \frac{\int_0^\infty \sigma(r) p(\Theta) \frac{dn}{dr} dr}{\int_0^\infty \sigma(r) \frac{dn}{dr} dr}. \tag{2.29}$$

The phase function for a typical stratospheric lognormal distribution is shown in blue. The averaging tends to damp the resonances in the backscattering direction, although the forward scattering peaks remains for typical size distributions seen in the stratosphere.

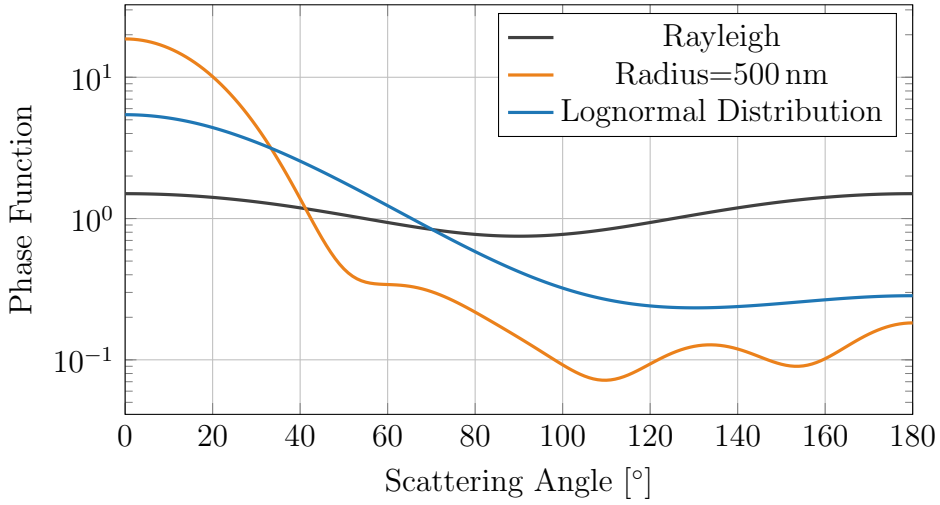

Figure 2.7: Phase functions for three different particle sizes. The Rayleigh phase function, eg. a particle with radii $\ll \lambda$ is shown in black. A particle with a radius of 500 nm is shown in orange. In blue, the phase function for a lognormal distribution with median radius of 100 nm and width of 1.5 is shown.

This has important implications for aerosol measurements as the aerosol signal from scattered light depends directly on the magnitude of the phase function at the scattering angle of the measurement. Instruments that take measurements with a large scattering angle will generally have smaller aerosol signals than instruments that measure in more forward scattering geometries. Additionally, the variability of the phase function with respect to particle size can change based on the scattering angle. Measurements near 60° tend to show smaller variability than at other angles so measurements at different geometries will have different sensitivity to any assumptions about the particle size. This effect is explored in much more detail in Chapter 4.

A note on derived parameters

Although the particle size distribution and composition fully defines the aerosol optical properties, these quantities are rarely available in practical applications, and so intermediate quantities between the raw spectral radiance and the size distribution are often reported.

Extinction along a path is a relatively straightforward quantity to both measure and interpret, and so has become a commonly reported quantity over a range of wavelengths. Since the wavelength dependence of the extinction is dictated by the particle size distribution and particle composition, it contains information on the aerosol microphysical properties. While particle size cannot generally be inferred exactly from extinction measurements, an empirical relationship called the Ångström coefficient, or Ångström exponent, is often used as an approximate guide to particle size. The Ångström coefficient, α is defined as the logarithmic ratios of extinction and wavelength as,

$$\frac{k(\lambda_1)}{k(\lambda_2)} = \left(\frac{\lambda_1}{\lambda_2}\right)^{-} \alpha. \tag{2.30}$$

As particles approach the Rayleigh limit the Ångström coefficient approaches four, with relatively monotonically increasing values up to size parameters of approximately one. Larger particles have a less clear relationship, with the coefficient dependent on the wavelengths being used. Additionally, the relationship is less certain when a collection of particles is being analyzed. Nonetheless, it remains in common use, and can provide an approximate indication of whether a signal is dominated by larger or smaller particles.

2.3 Stratospheric Aerosol Records

In addition to the balloon-borne optical particle counters several long-term records of stratospheric aerosol currently exist, and while in situ measurements provide detailed information on optical properties, the use of remote sensing is a far more commonly used technique. Ground based remote sensing measurements of aerosol have existed for decades, including the AErosol RObotic NETwork (AERONET), an array of sun photometers that measure attenuation and scattering in the atmosphere (Holben *et al.,* 1998). However, the nature of the measurements necessitates viewing the stratosphere through the aerosol filled troposphere, making disambiguation between tropospheric and stratospheric signals difficult. While some altitude resolution is possible, particularly under volcanic conditions (Ridley *et al.,* 2014), use of ground based sun photometers are generally limited to total column measurements. Lidars has been used from the ground to measure atmospheric parameters since the early

1960's (Goyer *et al.,* 1963; Fiocco *et al.,* 1964), and have progressed rapidly with increasing power, sensitivity, and the addition of polarization, Raman scattering, and differential absorption techniques. By pulsing the laser and sampling the return signal at MHz frequencies or higher, the atmosphere can be probed with vertical resolution of tens of meter. A handful of long-running stratospheric aerosol lidar records are available dating back to the mid-1970s, including from the Mauno Loa Observatory (MLO) (Barnes *et al.,* 1997), the Observatoire de Haute-Provence (OHP) (Khaykin *et al.,* 2017) and the Garmisch-Partenkirchen lidar (GP) in Germany (Trickl *et al.,* 2013). Together with balloon measurements these records provide excellent, time and altitude resolved pictures of the Junge layer, but are generally constrained to mid-latitude locations. This limited perspective has lead to difficulty in the attribution of increases in the Junge layer, with an early study attributing increases to biomass burning (Hofmann *et al.,* 2009). However, the use of satellite measurements afforded a truly global picture, and the much greater importance of small volcanic eruptions was later realized as the dominant factor in the increase of aerosol levels (Vernier *et al.,* 2011).

Several satellite instruments have been launched over the years, using a variety of remote sensing methods, that help contribute to this global picture. Table 2.1 show a selection of the most commonly referenced stratospheric aerosol datasets and the time span of the records. The following sections give an overview of the different satellite techniques and their advantages and disadvantages.

2.3.1 Occultation

The first space-based measurements of stratospheric aerosol came from solar occultation measurements, where as the satellite orbits it scans the solar disc as it rises and sets through the atmosphere. This measurement geometry is shown in Figure 2.8. By measuring the change in intensity as the sun passes through the atmosphere a vertical profile of the attenuation is measured. Taking the ratio of the measured spectral radiance, I to measurements above the atmosphere the optical depth along path j can be computed directly as

$$\ln\left(\frac{I_0}{I_j}\right) = \tau, \tag{2.31}$$

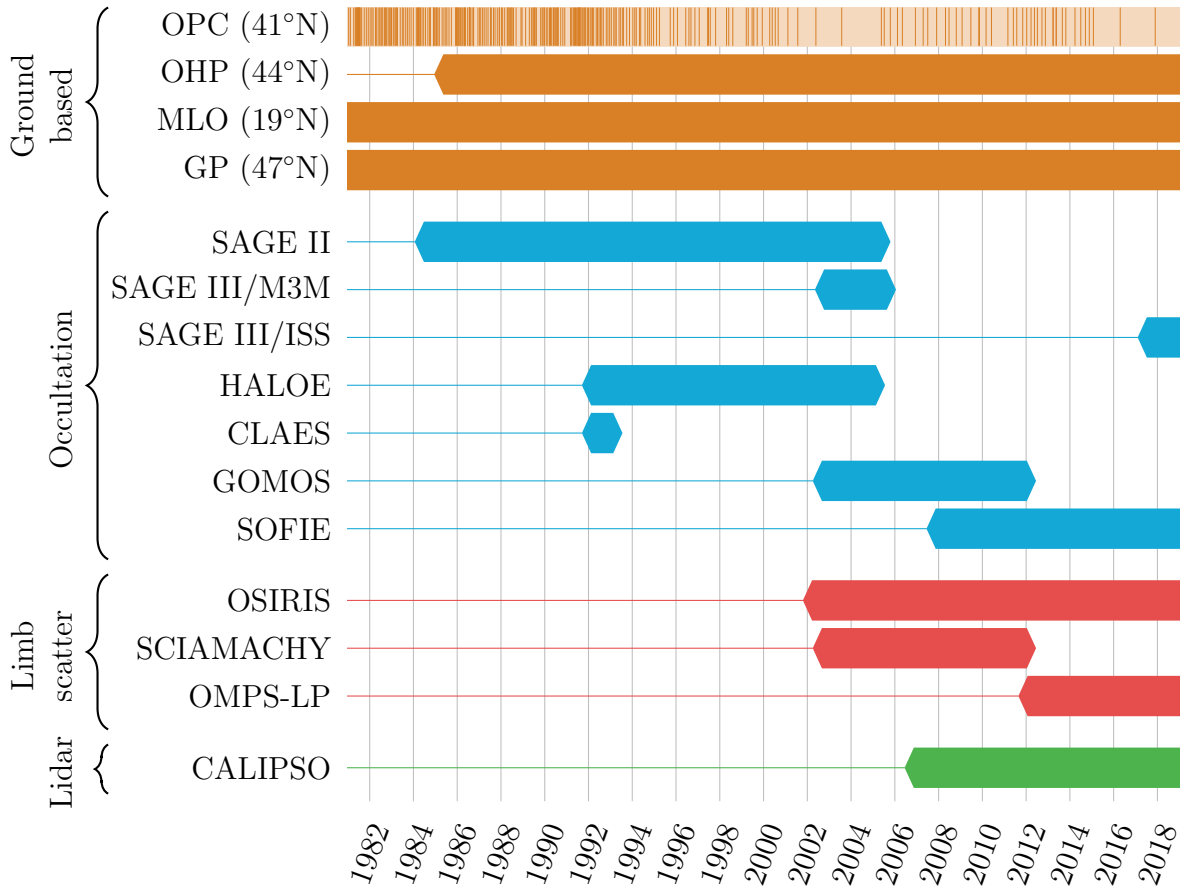

Table 2.1: Commonly used stratospheric aerosol records. Each vertical bar in the OPC record indicates one balloon flight. The remaining ground based records are lidars.

where I_0 is the exo-atmospheric measurement. If other atmospheric constituents are known, this provides a direct measure of the amount of scattering and absorption that is caused by aerosol particles along the path. The measurement at the highest layer of the atmosphere can be used directly with the geometric path length to determine the extinction at this layer, k_1. The extinction in the next lowest layer, k_2, can then be solved for directly as,

$$\ln\left(\frac{I_0}{I_2}\right) = k_1 \Delta s_1 + k_2 \Delta s_2, \tag{2.32}$$

where Δs_j is the path length through the j^{th} layer. Measurements at successively lower altitudes can then be "onion-peeled" to derive a vertical profile of aerosol extinction. This technique has many benefits including high signal-to-noise, inherent calibration with each scan due to the normalization with I_0, ease and directness of extinction inversion, and good vertical resolution. These advantages come at the cost of horizontal resolution, which is

typically on the order of several hundred kilometers, and sparsity of measurements. Because the satellite encounters a sunrise/sunset event only twice per orbit, a space-based occultation instrument will typically acquire approximately 30 vertical profiles per day, depending on the spacecraft altitude. Additionally, these profiles are not distributed equally over the globe, but are confined to a narrow latitude band that oscillates throughout the year, as shown in Figure 3.2. Although the quantity of extinction does not fully describe aerosol particles, and is only weakly related to the total aerosol mass through the size distribution, it provides much more direct information on the radiative forcing caused by aerosols. Additionally, the wavelength dependence of the extinction provides some information on particle size. Together with the robustness and longevity of occultation measurements, the extinction parameter has become a defacto standard of aerosol measurements.

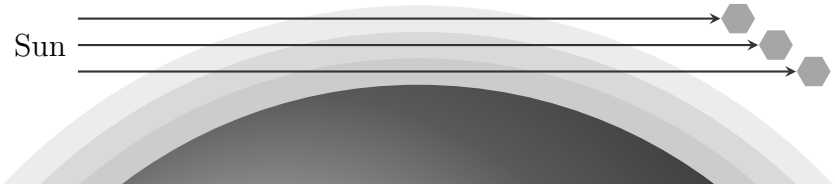

Figure 2.8: Occultation geometry showing a satellite taking measurements at various altitudes.

The first satellite instrument to implement this strategy was the Stratospheric Aerosol Measurement (SAM) II, launched in 1978 on the Nimbus 7 platform (McCormick *et al.,* 1979). SAM II took radiance measurements using a single channel sun photometer at a wavelength of 1 micron and provided coverage between ±64° and ±83° depending on the time of year with 27 profiles per day. SAM operated until 1993 and was followed by a series of Stratospheric Aerosol and Gas Experiments (SAGE) I, II, III/M3M, and recently III/ISS. SAGE II (Russell *et al.,* 1989) was launched in 1985 and built on the heritage of SAM II expanding the extinction measurements to wavelengths at 386, 452, 525 and 1020 nm. This allowed for derivation of some particle size parameters such as surface area density and effective radius, although the robustness of these products was much poorer than extinction. SAGE II provided global coverage on a monthly time-scale until 2005 when operations were

ceased. Following SAGE II was SAGE III/M3M (Thomason *et al.,* 2003), so named for its operation on the Meteor-3M platform from the end of 2001 to mid-2006. The third iteration also expanded the aerosol information, adding measurements at 1.53 µm. However, SAGE III/M3M was placed in a polar orbit, limiting coverage to mid-and-high latitudes. After SAGE III/M3M, it was over a decade before SAGE III/ISS was installed onto the international space station on February 9$^{\text{th}}$ 2017, leaving a large gap in the visible and near infrared solar occultation aerosol record.

Since the success of SAGE II, several additional occultation instruments have been launched for Earth observations with slightly different goals and measurement approaches. The Envisat platform housed several instruments including the Global Ozone Monitoring by Occultation of Stars, or GOMOS (Kyrölä *et al.,* 2004). Rather than using the sun a light source, GOMOS followed stars as they rose and set through atmosphere. This modification allows for much greater sampling and spatial coverage, as many more profiles can be taken per orbit, but the much weaker and more variable nature of star light makes determination of aerosol quantities subject to larger uncertainty. Occultation measurements further into the infrared have also been made, particularly from the Upper Atmosphere Research Satellite (UARS) with both the Halogen Occultation Experiment (HALOE) (Russell III *et al.,* 1993) and the much shorter lived Cryogenic Limb Array Etalon Spectrometer (CLAES) (Roche *et al.,* 1993). These instruments measured wavelengths ranging from 2.3 to 13 microns, and have been particularly useful in the Pinatubo period when extinction values were too large for optical instruments to measure (Thomason *et al.,* 2018). The Solar Occulation For Ice Experiment (Gordley *et al.,* 2009), operating since 2009, has also been used to look at stratospheric aerosols, but scans mainly the upper stratosphere and mesosphere, with a focus on meteoric dust and mesospheric clouds (Hervig *et al.,* 2009; Hervig *et al.,* 2017, e.g.).

2.3.2 Lidar

Although lidars allow for highly resolved measurements, interpretation of the signal from a lidar is less straightforward than that from an occultation measurement. The power at a lidar receiver from a scattering at altitude z is a function of the pulse energy, E_0, the speed of light, c, the receiver area, A, as well as the extinction along the path and the phase function

at the scattering altitude,

$$P(z) = E_0 \frac{cA}{2z^2} p(\Theta) k(z) e^{-2\int_0^z k(z')dz'}. \tag{2.33}$$

The difficulty arises from the multiplication of the extinction, by the phase function. If the optical properties are not known the phase function must be estimated, and the extinction cannot be determined directly, unlike for occultation measurements. As shown in Figure 2.9, the theory of operation of a lidar satellite is similar to a ground based lidar; however, there are two main advantages to a space-based lidar. First, and most importantly, is the possibility of global coverage on a daily basis. Second, the signal does not need to pass through the relatively thick and aerosol dense troposphere before scattering off of stratospheric aerosol, decreasing uncertainty in the optical depth to the scattering point. One difficulty in satellite lidars is the limited power relative to ground-based stations reduces the signal-to-noise. Since the path lengths through the atmosphere are only approximately as long as the vertical resolution, typically tens to hundreds of meters, the sensitivity to low levels of aerosols can be poor, requiring large amounts of averaging at high altitudes and during background volcanic conditions that can greatly reduce the resolution and signal to noise. An additional benefit of lidars is that, because the laser pulse is typically polarized, if the polarization of the return signal is also measured then the degree of depolarization by the atmosphere can be determined. This is important when distinguishing between clouds and aerosols, as scattering by ice particles will cause depolarization that does not occur from scattering by spherical particles.

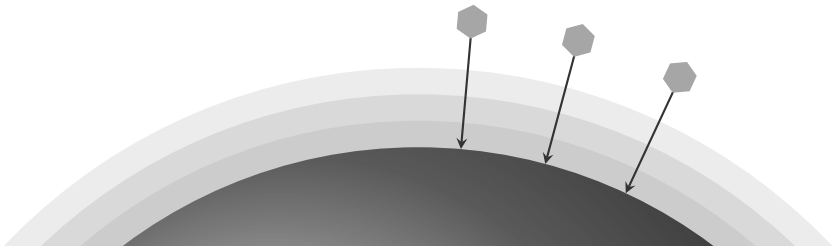

Figure 2.9: Lidar satellite taking several measurements along a ground track.

Despite the decades of success of ground based lidars, it wasn't until the launch of Ice,

Cloud and Land Elevation Satellite (ICESat) in 2003 (Zwally *et al.,* 2002) that a lidar had been used on a satellite for atmospheric measurements. Following ICESat, the Cloud-Aerosol lidar and Infrared Pathfinder Satellite Observation (CALIPSO) mission was launched in 2006 (Winker *et al.,* 2010). CALIPSO includes a Cloud-Aerosol Lidar with Orthogonal Polarization (CALIOP) with wavelengths at 532 and 1064 nm. Both the parallel and perpendicular component of the returning 532 nm signal are measured to help distinguish between liquid and solid particles, which can be of great importance when measuring aerosols in the presence of clouds. In addition to CALIPSO, the ADM-Aeolus lidar (Ansmann *et al.,* 2007) and Cloud-Aerosol Transport System (McGill *et al.,* 2015) were launched in 2015 and 2018 respectively. While ADM-Aeolus's primary mission is focused on wind speed measurements it also produces vertical profiles of clouds and aerosols in the lower stratosphere (Flamant *et al.,* 2008). ICESat-2 is a laser system with wavelengths at 532 and 1064 nm that was launched in September 2018 with a planned 5 year lifetime (Abdalati *et al.,* 2010). EarthCARE, planned for launch in 2021, will carry a UV laser and include measurements of the depolarization ratio for improved cloud and aerosol discrimination (Illingworth *et al.,* 2015).

2.3.3 Limb Scatter

Although occultation satellites have provided quality datasets for decades, the limited spatial and temporal sampling prompted the development of higher resolution techniques. Rather than scan the solar disc directly, the limb scattering technique scans the Earth's horizon when the sun is not directly in the field of view, as shown in Figure 2.10. Light from the sun is scattered throughout the atmosphere and off of the Earth's surface and into the instrument line of sight. This has similar advantages of the occultation technique, i.e., long path lengths for good signal-to-noise with comparable vertical resolution, and also allows measurements to be taken during any sunlit portion of the orbit. This translates to much higher sampling rates, typically hundreds to thousands per day, allowing for investigation of shorter lived events and reducing sampling biases when constructing climatologies. The complicating factor is that, unlike occultation and lidar techniques, the signal is no longer from a single source attenuated or backscattered to the instrument, but rather a diffuse field of scattered solar radiation that depends on the state of the atmosphere and geometry of the observation. This couples each

layer of the atmosphere both to those above it and those below it, and requires solving the radiative transfer equation (Eq. 2.10) to model the signal.

While accurate solutions to this problem are needed for scientific products, first order approximations can shed light on the sensitivity to aerosols and where difficulties in using limb scattering measurements arise. Although the multiple scattering signal can be large in some cases, the single scattered component often dominates. In this case the radiance originating from point s along the instrument line of sight is proportional to

$$I\tilde{k}(s)p(s,\Theta)e^{\int_s^{s_0} k(s')ds'}, \tag{2.34}$$

and shares many similarities with the lidar equation, where the signal depends on the magnitude of the extinction, but also the probability that light is scattered into the direction of the satellite. This makes the signal dependent directly on the phase function, and hence the aerosol optical properties. While this means the measurements include information on the phase function, in practice it makes unique determination of the extinction quantity more difficult, as uncertainty in the phase function causes uncertainty in the extinction. This effect is exacerbated relative to lidars as the scattering angle, Θ, in limb satellite measurements changes as a function of latitude and season along with the orbit, potentially aliasing these biases as physical and temporal features.

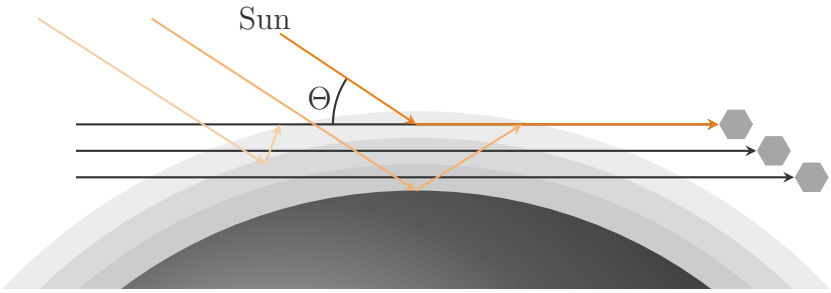

Figure 2.10: Limb geometry measurement technique: shown is a measurement at a single tangent altitude with single, multiple and surface scattered light rays.

Despite the potential challenges, satellite limb scattering measurements began not long after the first occultation measurements, with the Solar Mesosphere Explorer (SME) being launched in 1981 (Barth *et al.,* 1983). SME was equipped with five instruments including

spectrometers at 1.27, 1.86 and 6.8 µm that were used to retrieve aerosol profiles (Thomas *et al.,* 1983). Taking a simple approach of tumbling through space and scanning the horizon as it did so, SME was able to produce a global picture of stratospheric aerosols after the large El Chichón eruption (Eparvier *et al.,* 1994).

The Optical Spectrograph and Infrared Imaging System (OSIRIS) was launched in 2001 with a spectrometer measuring wavelengths from 280 to 810 nm (Llewellyn *et al.,* 2004). Placed into a near-terminator orbit, OSIRIS measures a single line of sight as the satellite nods, scanning the atmosphere from approximately 7 to 100 km altitude. OSIRIS measurements form the basis of this work and are discussed in further detail in subsequent chapters. Shortly following OSIRIS was the launch of the SCanning Imaging Absorption SpectroMeter for Atmospheric CHartographY in 2002 on the Envisat satellite (Bovensmann *et al.,* 1999). SCIAMACHY was similar to OSIRIS in many ways, using a scanning spectrometer to measure UV and visible profiles, but extended further into the infrared region, measuring wavelengths out to 2340 nm. Envisat operated until 2012 when communication was lost, but the limb scatter dataset has been used in numerous studies to derive aerosol extinction as well as particle size properties (Ernst *et al.,* 2012; von Savigny *et al.,* 2015; Malinina *et al.,* 2018). Following SCIAMACHY, the SAGE III instruments also incorporated a limb scattering mode, however to date the measurements have not been used to produce operational aerosol products. The Ozone Mapping and Profiler Suite - Limb Profiler (OMPS-LP) was launched in 2011, and began the next generation of limb scattering instruments (Flynn *et al.,* 2006). OMPS-LP measures vertical profiles from 280 to 1000 nm, but rather than scanning the limb takes three simultaneous vertical images. This allows for approximately 10 times more profiles per day than OSIRIS or SCIAMACHY, and allows for tomographic retrievals of aerosol and ozone (Zawada *et al.,* 2018).

Currently, OSIRIS and OMPS-LP are the only operational limb instruments dedicated to scattering measurements, but future missions with such instruments are planned, ensuring the continued importance of understanding and improving the technique. NASA has limb scattering instruments planned for the Joint Polar Satellite System (Goldberg *et al.,* 2013b), and the European Space Agency is also planning a limb imaging instrument, ALTIUS, that will take two dimensional spectrally resolved images of the limb (Fussen *et al.,* 2016).

2.4 The Inverse Problem

No matter the measurement system, aerosol quantities are not measured directly and the radiance, transmission, or backscattering ratio must be converted to a more interpretable quantity. This is not unique to the field of aerosol retrievals, and determination of the state of a system based on observations is broadly used in physics and typically referred to as the field of inverse problems. Broadly, the solution to inverse problems proceeds as follows:

1. Start with a model of the system, using an initial guess as to the state of the system.
2. Compare the output of the model with the observations and use the difference to update the state of the system.
3. Repeat step 2 until the model output and the observations have converged. At this point the state of the modelled system is said to be the retrieved state.

This process relies on few crucial aspects. First, is a measurement that is relatively insensitive to unknown quantities. For stratospheric aerosols this is typically a normalized profile of radiance, transmission or backscattering ratio, depending on the instrument. Next, is a model of the system in question that is capable of simulating these measurements, a *radiative transfer model*, or RTM, in the case of aerosols. Lastly, is a method of comparing the measurement and model to update the system state.

More mathematically, the forward problem is generally written as

$$\mathbf{y} = F(\mathbf{x}, \mathbf{b}) + \boldsymbol{\epsilon}, \tag{2.35}$$

where $\mathbf{y}$ is a set of observables generated from the system F, that depends on the desired state vector, $\mathbf{x}$, as well as additional parameters, $\mathbf{b}$. The measurements typically include some error, $\boldsymbol{\epsilon}$. For the work that follows the observables are composed of satellite measurements of radiance, while $\mathbf{x}$ is typically a vertical profile of extinction.

These problems can be broken into the broad categories of linear or nonlinear, and underdetermined or overdetermined. While atmospheric retrievals are generally both non-linear and underdetermined, it is useful to first briefly visit the solution techniques of linear problems. For this we adopt the notation that the $m \times n$ matrix $\mathbf{K}$, often called the Jacobian or

kernel, is the sensitivity of the observable to changes in the state.

$$K_{ij} = \frac{\partial y_i}{\partial x_j}. \tag{2.36}$$

In the case of a well-posed linear problem the solution is found from simple inversion,

$$\hat{\mathbf{x}} = \mathbf{K}^{-1}\mathbf{y}. \tag{2.37}$$

Here, $\hat{\mathbf{x}}$, is used to denote the retrieved state, rather than the true state, $\mathbf{x}$. If the system is overdetermined and has only a trivial null space, the state can be estimated directly as

$$\hat{\mathbf{x}} = \left(\mathbf{K}^{\mathrm{T}}\mathbf{K}\right)^{-1}\mathbf{K}^{\mathrm{T}}\mathbf{y}, \tag{2.38}$$

to obtain the well known linear least squares solution. This approach minimizes the cost function

$$\chi^2 = \left(\mathbf{y} - \mathbf{K}\hat{\mathbf{x}}\right)^{\mathrm{T}}\left(\mathbf{y} - \mathbf{K}\hat{\mathbf{x}}\right). \tag{2.39}$$

Additionally, if the measurement covariance, $\mathbf{S}_y$, is known then the weighted error can be minimized as

$$\chi^2 = \left(\mathbf{y} - \mathbf{K}\hat{\mathbf{x}}\right)^{\mathrm{T}}\mathbf{S}_y^{-1}\left(\mathbf{y} - \mathbf{K}\hat{\mathbf{x}}\right), \tag{2.40}$$

and the direct solution is

$$\hat{\mathbf{x}} = \left(\mathbf{K}^{\mathrm{T}}\mathbf{S}_y^{-1}\mathbf{K}\right)^{-1}\mathbf{K}^{\mathrm{T}}\mathbf{S}_y^{-1}\mathbf{y}. \tag{2.41}$$

Difficulties begin to arise if the problem is underdetermined, as is often the case in remote sensing applications. If the matrix $\mathbf{K}$ has a non-trivial null-space, then a solution cannot be uniquely determined. In this case, changes in $\mathbf{x}$ that are within the null-space are mapped to zero and the cost function, Eq. 2.40, is unchanged, leading to a family of possible solutions. To counter this, Tikhonov (1943) added a second term to the cost function that does not have the same null-space as $\mathbf{K}$, resulting in

$$\chi^2 = \left(\mathbf{y} - \mathbf{K}\hat{\mathbf{x}}\right)^{\mathrm{T}}\mathbf{S}_y^{-1}\left(\mathbf{y} - \mathbf{K}\hat{\mathbf{x}}\right) + \mathbf{x}^{\mathrm{T}}\mathbf{\Gamma}^{\mathrm{T}}\mathbf{\Gamma}\mathbf{x}. \tag{2.42}$$

The regularization matrix, $\mathbf{\Gamma}$ can be chosen to minimize a variety of effects, including the two-norm of $\hat{\mathbf{x}}$ by setting $\mathbf{\Gamma} = \mathbf{I}$, or oscillatory behavior by setting $\mathbf{\Gamma}$ as a numerical difference operator. In this case, the solution becomes

$$\hat{\mathbf{x}} = \left(\mathbf{K}^{\mathrm{T}}\mathbf{S}_y^{-1}\mathbf{K} + \mathbf{\Gamma}^{\mathrm{T}}\mathbf{\Gamma}\right)^{-1}\mathbf{K}^{\mathrm{T}}\mathbf{S}_y^{-1}\mathbf{y}. \tag{2.43}$$

This can also be very useful for ill-posed problems, where the solution is highly sensitive to any errors in $\mathbf{y}$. Also common in atmospheric retrievals is to incorporate a priori knowledge of the atmosphere into the retrieval. Deviations from the a priori assumption, $\mathbf{x}_a$, can be penalized in the cost function as,

$$\chi^2 = (\mathbf{y} - \mathbf{K}\hat{\mathbf{x}})^{\mathrm{T}} \mathbf{S}_y^{-1} (\mathbf{y} - \mathbf{K}\hat{\mathbf{x}}) + (\hat{\mathbf{x}} - \mathbf{x}_a)^{\mathrm{T}} \mathbf{\Gamma}^{\mathrm{T}} \mathbf{\Gamma} (\hat{\mathbf{x}} - \mathbf{x}_a). \tag{2.44}$$

In this case the solution is

$$\hat{\mathbf{x}} = \left(\mathbf{K}^{\mathrm{T}} \mathbf{S}_y^{-1} \mathbf{K} + \mathbf{\Gamma}^{\mathrm{T}} \mathbf{\Gamma}\right)^{-1} \left(\mathbf{K}^{\mathrm{T}} \mathbf{S}_y^{-1} \mathbf{y} + \mathbf{\Gamma}^{\mathrm{T}} \mathbf{\Gamma} \mathbf{x}_a\right). \tag{2.45}$$

Rodgers (2000) details this method using a Bayesian approach where the observations and a priori atmospheric state are represented as probability distributions, commonly assumed to be gaussians. This is often referred to as optimal estimation and has the nice result that the solution, $\hat{\mathbf{x}}$, is itself a probability distribution with estimates of the solution covariance. However, it relies on accurate representation of the a priori state, which is not necessarily available.

While Equation 2.45 provides a robust method of solving ill-posed linear problems, atmospheric retrievals are inherently nonlinear, with a Jacobian, $\mathbf{K}$ that depends on the state vector, $\mathbf{x}$. When this is the case the solution must be iterated until convergence is achieved,

$$\hat{\mathbf{x}}^{n+1} = \hat{\mathbf{x}}^n + \left(\mathbf{K}^{\mathrm{T}} \mathbf{S}_y^{-1} \mathbf{K} + \mathbf{\Gamma}^{\mathrm{T}} \mathbf{\Gamma}\right)^{-1} \left(\mathbf{K}^{\mathrm{T}} \mathbf{S}_y^{-1} \left(\mathbf{y} - F(\hat{\mathbf{x}}^n)\right) + \mathbf{\Gamma}^{\mathrm{T}} \mathbf{\Gamma} \left(\hat{\mathbf{x}}^n - \mathbf{x}_a\right)\right), \tag{2.46}$$

where the superscript n denotes the n^{th} iteration. However, for problems that are sufficiently nonlinear, the next iteration may overshoot the solution leading to slow convergence or increasing oscillations about the solution. To combat this, Levenberg (1944) and later Marquardt (1963) proposed a damping term be added,

$$\hat{\mathbf{x}}^{n+1} = \hat{\mathbf{x}}^n + \left(\mathbf{K}^{\mathrm{T}} \mathbf{S}_y^{-1} \mathbf{K} + \mathbf{\Gamma}^{\mathrm{T}} \mathbf{\Gamma} + \gamma \mathrm{diag}\left(\mathbf{K}^{\mathrm{T}} \mathbf{S}_y^{-1} \mathbf{K}\right)\right)^{-1} \left(\mathbf{K}^{\mathrm{T}} \mathbf{S}_y^{-1} \left(\mathbf{y} - F(\hat{\mathbf{x}}^n)\right) + \mathbf{\Gamma}^{\mathrm{T}} \mathbf{\Gamma} \left(\hat{\mathbf{x}}^n - \mathbf{x}_a\right)\right). \tag{2.47}$$

Each iteration then takes a smaller step in the direction of the gradient to avoid overshooting. The factor, γ is chosen to maintain the solution within an approximately linear regime at each iteration, and can be updated to allow for the largest step size possible that still improves the solution.

The Levenberg-Marquardt (LM) algorithm has become a popular technique that provides a robust method for determining the least squares or regularized least squares solution to non-linear problems. However, LM relies on an accurate measure of the Jacobian at each step, and requires computing the inverse of what can be a very large matrix. Algebraic reconstruction techniques (ART) were developed by Kaczmarz (1937) and have been used extensively in tomographic retrievals. To avoid the inverse calculation ART updates the state vector by iteratively projecting the solution onto the hyperplane defined by the next linear equation as

$$\hat{x}_j^{n+1} = \hat{x}_j^n + K_{ij} \frac{(y_i - F_i(\hat{\mathbf{x}}^n))}{\sum_j K_{ij}^2}, \tag{2.48}$$

where i is used to cycle through the rows $\mathbf{K}$. Landweber (1951) developed a simultaneous version of the algorithm that uses an average projection to avoid amplifying noise from individual projections,

$$\hat{x}_j^{n+1} = \hat{x}_j^n + w \sum_i K_{ij} \left(y_i - F_i(\hat{\mathbf{x}}^n)\right), \tag{2.49}$$

where w is a relaxation parameter used to damp the step size. If the state vector and the Jacobian are positive and we wish for the state to remain positive, then Gordon *et al.* (1970) noted that a multiplicative version can be used, where the update is computed as

$$\hat{x}_j^{n+1} = \hat{x}_j^n \left(\frac{y_i}{F_i(\hat{\mathbf{x}})} \right)^{m_i K_{ij}}, \tag{2.50}$$

where m_i is a factor that ensures the maximum value in each column of K is one. As with ART, MART has a simultaneous version, that uses all of the equations at each step. A variant of the simultaneous MART, also called the expectation maximization maximal likelihood (EMML) method (Dempster *et al.,* 1977) simplifies Equation 2.50 by replacing the exponentiation with a multiplier, W,

$$\hat{x}_j^{n+1} = \hat{x}_j^n \sum_i W_{ij} \frac{y_i}{F_i(\hat{\mathbf{x}})}. \tag{2.51}$$

The term $m_i K_{ij}$ is used as a multiplier instead, and collapsed into a single weighting matrix, $\mathbf{W}$. An import difference between the LM algorithm and MART is that while both methods aim to minimize differences between the model and the measurements, the quantities minimized are not identical. LM converges to the least squares solution, while MART minimizes

the Kullback-Liebler divergence (Byrne, 1993), defined as

$$KL(\mathbf{y}, \mathbf{F}) = -\sum_j y_j \log\left(\frac{y_j}{F_j(\hat{\mathbf{x}})}\right). \tag{2.52}$$

The MART technique is often applied to image reconstruction problems, especially those where signals are derived from Poisson counting as the solution converges to the maximal likelihood value. However, MART has also been applied to atmospheric limb measurements for both tomographic (Degenstein *et al.,* 2003) and non-tomographic retrievals (Degenstein *et al.,* 2009; Bourassa *et al.,* 2012a) that are used in this work. In these cases the weights, W, are fixed as an approximation to the Jacobian, avoiding the computation of the Jacobian.

Chapter 3

Merging the OSIRIS and SAGE II stratospheric aerosol records

[1]Rieger, L. A., [1]A. E. Bourassa, and [1]D. A. Degenstein (2015), Merging the OSIRIS and SAGE II stratospheric aerosol records, J. Geophys. Res. Atmos., 120, 8890–8904, doi: 10.1002/2015JD023133.

[1]Institute of Space and Atmospheric Studies, University of Saskatchewan, Saskatoon, Canada

Although the climate effects of eruptions such as Pinatubo were large enough to be evident through temperature decreases at the surface, heating in the stratosphere, and severe ozone loss, the impacts of smaller eruptions have been much more difficult to distinguish from natural background fluctuations. Simultaneously, over the last decade, climate models have predicted a warming that has generally exceeded observations and has been referred to as the "warming hiatus" (Fyfe *et al.,* 2013). Explanations of this effect have varied, including natural variability, changes in ocean circulations, and inaccuracies in the volcanic aerosol record (England *et al.,* 2014; Santer *et al.,* 2017).

The advent of global aerosol monitoring systems in the 1980's precipitated never-before-seen measurements of the large eruptions of El Chicon (1982), Neva del Ruiz (1985), and Mt. Pinatubo (1991). These instruments provided amazing detail of eruptions that had previously been too small to see in other historical records such as ice-cores and tree rings. Then, for a decade following Mt. Pinatubo a remarkably quiet period followed which allowed the stratospheric aerosol layer to relax to a "background" state.

While progress in aerosol measurements marched steadily forward, the advances were not initially incorporated into climate modelling. Models relied on cruder vertically integrated, and often globally averaged, stratospheric aerosol time series to estimate radiative forcing. In the Coupled Modelled Intercomparison Project 5, two datasets were largely used to incorporate radiative effects from stratospheric aerosols. The Ammann *et al.* (2003) record used historical records and a simple exponential aerosol model to derive aerosol optical depth as a function of latitude and time at a single wavelength. No satellite records were used directly in the model and after 1998 aerosol was assumed to remain at constant background levels. The Sato *et al.* (1993) record incorporated limited satellite data and provided aerosol extinction at four altitude levels, but did not use the full SAGE II record, and used a crude scaling for the post-SAGE era. These records are shown in Figure 3.1. The Ammann record has a much smaller optical depth of 10^{-4} during background levels, while the Sato records has a marked discontinuity in 1998 when the records switch from using the SAGE II measurements to OSIRIS.

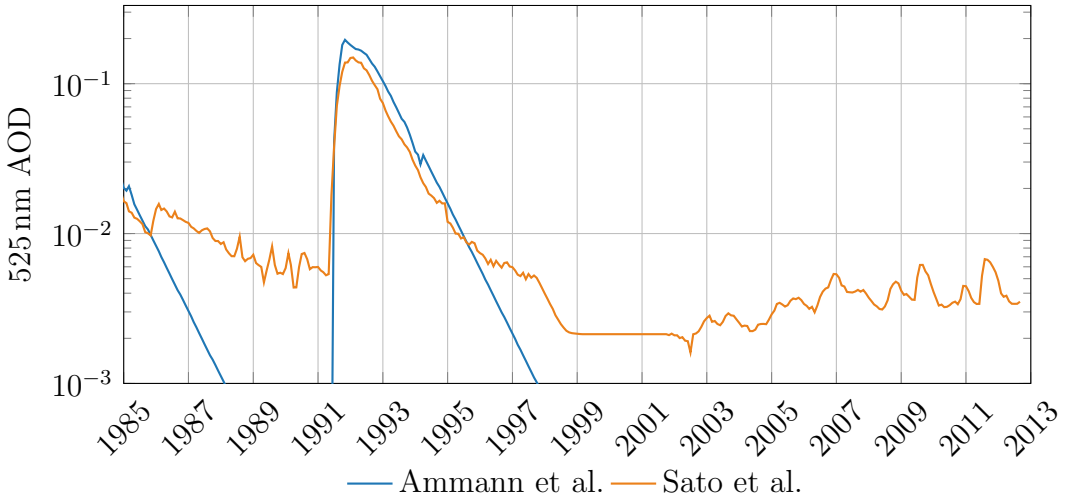

Figure 3.1: The globally averaged Ammann *et al.* (2003) and Sato *et al.* (1993) stratospheric aerosol records most commonly used in CMIP5, shown in blue and orange respectively.

A series of studies started to change this picture, and indicated stratospheric aerosols may be playing a role in the warming hiatus (Solomon *et al.,* 2011; Fyfe *et al.,* 2013a; Haywood *et al.,* 2014; Santer *et al.,* 2014). However, the datasets used in these studies were generally inconsistent, and there was a push from the modelling community to standardize

the aerosol inputs to help compare and constrain model evaluations. Towards that end, the following chapter explores extending the SAGE II stratospheric aerosol dataset from 2005 to the present using the OSIRIS instrument. Since publication the dataset developed in this work has been incorporated into the Global Space-based Stratospheric Aerosol Climatology (Thomason *et al.,* 2018) that provides the stratospheric aerosol forcing to all CMIP 6 climate models. While the manuscript presented in this chapter is largely my work in terms of analysis and manuscript preparation, my supervisors and co-authors have been crucial in its development. In addition to producing the OSIRIS aerosol data product used in this analysis, their help with the overall structure of the paper, as well as technical edits and help with revisions have greatly improved the manuscript.

3.1 Abstract

The Optical Spectrograph and InfraRed Imaging System (OSIRIS) instrument on the Odin satellite, launched in 2001 and currently operational, measures limb-scattered sunlight from which profiles of stratospheric aerosol extinction are retrieved. The Stratospheric Aerosol and Gas Experiment (SAGE) II was launched in 1984 and provided measurements of stratospheric aerosol extinction until mid-2005. This provides approximately 4 years of mission overlap which has allowed us to consistently extend the SAGE II version 7.00 record to the present using OSIRIS aerosol extinction retrievals. In this work we first compare coincident aerosol extinction observations during the overlap period by interpolating the SAGE II 525 nm and 1020 nm channels to the OSIRIS extinction wavelength of 750 nm. In the tropics to midlatitudes mean differences are typically less than 10 %, although larger biases are seen at higher latitudes and at altitudes outside the main aerosol layer. OSIRIS aerosol extinction retrievals at 750 nm are used to create a monthly time series zonally averaged in 5°bins and qualitatively compared to SAGE II 525nm observations averaged in the same way. The OSIRIS time series is then translated to 525nm with an Ångström exponent relation and bias corrected. For most locations, this provides agreement during the overlap time period to better than 15 %. Uncertainty in the resulting OSIRIS time series is estimated through a series of simulation studies over the range of aerosol particle size distributions observed by in situ

balloon instruments and is found to be approximately 20 % for background and moderately volcanic aerosol loading conditions for the majority of OSIRIS measurement conditions.

3.2 Introduction

The layer of aerosol in the stratosphere, often referred to as the Junge layer, plays an important role in the chemistry and radiative balance of the atmosphere. Composed primarily of hydrated sulfuric acid this layer scatters incoming light resulting in a cooling effect. Aerosols also play an important role in formation of polar stratospheric clouds and heterogeneous ozone chemistry. Much of this layer is naturally forming from sources of SO_2 and OCS and volcanic eruptions, the later of which can cause substantial increases in the layer over very short time scales. The importance of volcanic enhancements was particularly evident after the 1991 eruption of Mt. Pinatubo which caused a global cooling of nearly 0.5°C in the lower atmosphere (Soden *et al.,* 2002) and $0.1 - 0.3$°C at the surface (Thompson *et al.,* 2009; Canty *et al.,* 2013), but has been seen more recently with several small-to-moderate eruptions which have caused a sustained increase in the levels of stratospheric aerosols (Vernier *et al.,* 2011). These more recent eruptions may have also had a significant cooling effect when compared to background levels (Solomon *et al.,* 2011; Fyfe *et al.,* 2013a; Haywood *et al.,* 2014). The importance of this layer for radiative forcing and stratospheric chemistry, as well its large variability, make accurate, global aerosol records an important component of climate modelling.

Up-to-date, global, altitude and latitude resolved time series of stratospheric aerosol extinction are limited, and this work seeks to help extend the SAGE II extinction record to present by producing an OSIRIS time series that is consistent with the SAGE II extinction measurements across a wide range of altitudes and latitudes. The methodology employed here is to first explore the differences and possible biases of the OSIRIS 750 nm extinction measurements through a coincident comparison. This study, as well as an OSIRIS 750 nm extinction time series is presented in Section 3.3. In Section 3.4 the OSIRIS time series is converted to 525 nm and biases are corrected to produce 525 nm aerosol extinctions that extend the SAGE II record to the present. The merged time series is presented in Section 3.5

and results derived from this product are compared with other aerosol optical depth records. Section 3.6 explores the error due to particle size assumptions in the OSIRIS retrieval and conversion to 525 nm, with the importance of the Upper Troposphere and Lower Stratosphere (UTLS) region examined in Section 3.7. Finally, conclusions and recommendations are presented in Section 3.8.

3.2.1 SAGE II

The Stratospheric Aerosol and Gas Experiment (SAGE) II (Russell *et al.,* 1989) was launched in 1984 onboard the Earth Radiation Budget Satellite (ERBS) and was operational until mid 2005. ERBS had an orbit with a nominal altitude of 610 km and inclination of 57°. SAGE II is a 7-channel sun photometer with central wavelengths at 385, 448, 453, 525, 600, 940 and 1020 nm. Twice per orbit SAGE II rapidly scanned the solar disc as it rose/set through the atmosphere providing occultation measurements of atmospheric extinction with a vertical resolution of 1 km. Exo-atmospheric measurements provide an inherent calibration of each scan producing very stable measurements over the course of the 20 year mission. Each profile takes between 1.5 and 4 minutes to collect with up to 32 profiles per day at its peak, although the number of profiles was decreased to 16 after mid 2000. Combined with the ERBS orbit this provides measurements at 2 latitudes per day that shift over time, providing coverage from 80°S to 80°N every 1-2 months. Figure 3.2 shows the SAGE II latitude coverage throughout the year for 1995 and 2004. These years are typical of the coverage from 1985-2000 when SAGE II produces approximately 32 measurements per day, and post 2000 when measurements were decreased to 16 per day.

The SAGE II aerosol extinction retrieval algorithm has undergone several improvements since the version 6.2 algorithm, which was the standard product for many years. The version 6.2 algorithm translated the slant column transmission data from the 385, 453, 525 and 1020 nm channels into vertical profiles of aerosol extinction. The details of this algorithm are described in Chu *et al.,* 1989, however the basics are as follows. First, transmissions are converted to optical depths and the Rayleigh contribution is removed using meteorological data from NCEP and the Global Reference Atmospheric Model (GRAM-95). Next, the optical depths are inverted to extinction profiles on a 0.5 km grid using Twomey-Chahine

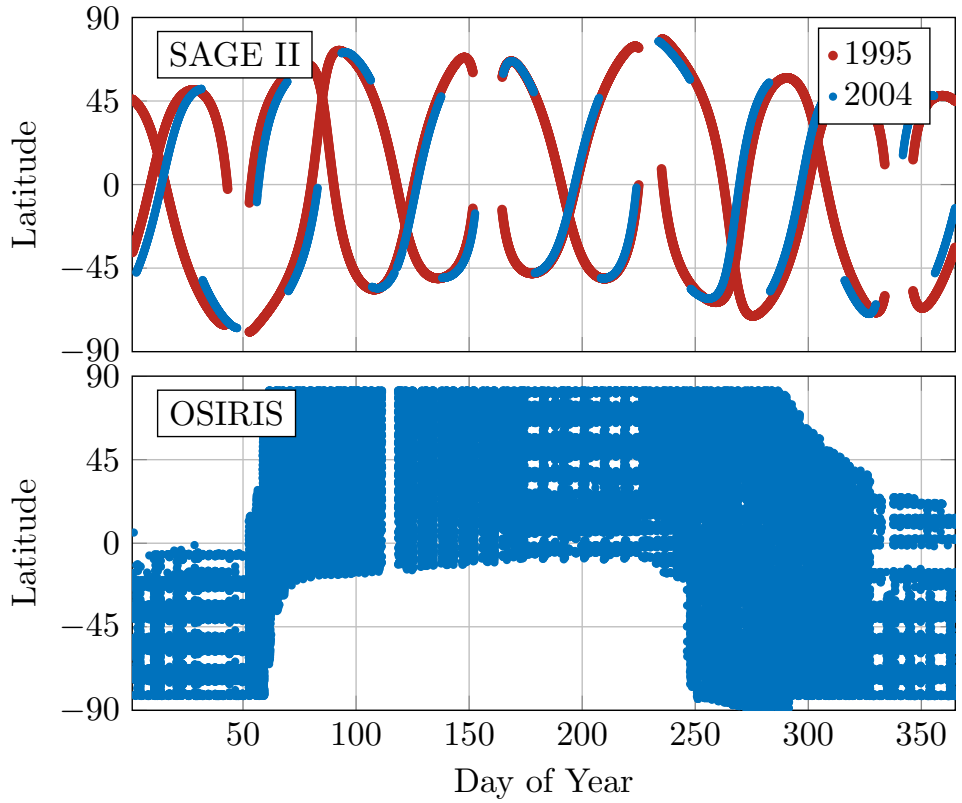

Figure 3.2: Latitude coverage of the SAGE II and OSIRIS orbits. Top panel shows the SAGE II latitude coverage in 1995 in red and 2004 in blue. The bottom panel shows the OSIRIS coverage in 2004.

relaxation (Twomey, 1975) with a 5 km altitude smoothing when extinction values fall below 2×10^{-5} km. The SAGE II retrievals have since been updated to version 7.00, details of which are discussed in Damadeo *et al.* (2013). The improved aerosol inversion is largely similar to version 6.2 with a few important differences. First, the ozone cross sections were changed, affecting the 525 nm inversion. Second, the meteorology data was changed to MERRA (Rienecker *et al.,* 2011). Finally, the Twomey-Chahine relaxation was replaced with a simple onion-peeling technique resulting in a general decrease in aerosol levels at altitudes above the main layer. All results from this paper use the version 7.00 aerosol extinction data.

3.2.2 OSIRIS

The Optical Spectrograph and InfraRed Imaging System (OSIRIS) is a limb scatter instrument launched in 2001 onboard the Odin satellite (Llewellyn *et al.,* 2004) and continues to operate successfully, retrieving O_3, NO_2 and aerosol extinction (McLinden *et al.,* 2012). Odin was placed into a sun-synchronous orbit at 600 km with ascending and descending node local times of 6PM and 6AM respectively, providing coverage from 82°S to 82°N, except in polar winter where lack of sunlight precludes measurements. The Optical Spectrograph (OS) is the primary instrument measuring between 284 and 810 nm with approximately 1.0 nm resolution. The OS measures scattered light along a single line of sight, which is scanned by nodding the satellite platform such that the tangent point scans from 7 to 75 km during typical operation. A scan takes approximately 90 seconds and provides vertical sampling every 2 km with a vertical resolution of approximately 1 km. This generally provides between 100 and 400 profiles per day, depending on the time of year, with a slight bias towards the northern hemisphere. Before 2007, the Odin observation modes were split between astronomy and aeronomy modes, switching between them every 2-3 days. After 2007 OSIRIS has been in full-time aeronomy mode, roughly doubling the amount of data. Figure 3.2 shows the OSIRIS latitude coverage for 2004. This coverage is typical, although it has improved slightly in later years due to Odin's orbital precession.

The OSIRIS inversion retrieves aerosol extinction at 750 nm on a 1 km grid with approximately 2 km resolution. This is done using a multiplicative relaxation technique similar to the Twomey-Chahine method. Details of the retrievals are discussed in Bourassa *et al.* (2007)

and Bourassa *et al.* (2012a), however a few points are worth highlighting here. The aerosol extinction retrieval is performed at 750 nm, as opposed to shorter wavelengths for several reasons. While the radiance measurements at 750 nm have approximately twice as much uncertainty as measurements near 525 nm, the sensitivity to aerosol at 750 nm is more than four times higher (and often more than that). This can be seen in supplemental Figure S1, where the gain matrices for aerosol retrievals performed at 750 and 525 nm are shown. At the peak of the aerosol layer, near 20 km, a 1% error in the 750 nm radiance will cause a 4% error in the retrieved extinction, while a 1% error in the 525 nm radiance will cause a 20% error in the retrieved extinction. This becomes even worse during high aerosol loading conditions and low altitudes when the shorter wavelengths become optically thick much sooner than 750 nm. This increased optical depth also limits the altitude range of shorter wavelength retrievals to higher altitudes. Additionally, increased ozone and NO_2 absorption near 525 nm have the potential to bias a 525 nm retrieval much more than one performed at 750 nm.

For the OSIRIS retrieval, modelling of the radiance signal is performed using SASKTRAN (Bourassa *et al.,* 2008) with meteorological data from ECMWF. Modelling of the limb scattered signal necessitates additional assumptions on the aerosol microphysics not required by occultation instruments. The standard OSIRIS aerosol retrieval, version 5.07, assumes a mix of 75% H_2SO_4 to 25% H_2O. In this retrieval aerosols are also assumed to have a lognormal particle size distribution with a mode width of 1.6 and mode radius of 80 nm. While these assumptions provide good results during volcanically quiescent periods (Bourassa *et al.,* 2012a) they are likely one of the major sources of bias in the OSIRIS retrievals, particularly during volcanic enhancements, when particle size can change markedly (Deshler *et al.,* 2003). While some particle size information has been retrieved with the OSIRIS version 6.00 algorithm (Rieger *et al.,* 2014), this requires use of the InfraRed Imager (IRI), which saturates at low altitudes and during periods of moderate volcanic loading. Because these locations and times can contain a bulk of the stratospheric aerosol they are of particular interest, and so the version 5.07 product is used for this merging.

While the measurement techniques vary, the OSIRIS and SAGE II instruments share many important characteristics. Both use similar wavelengths for the aerosol retrieval, both have approximately the same vertical resolution and range, with aerosol retrieved on an

altitude grid, as opposed to pressure. Since both instruments observe through the limb, both have path lengths of approximately 150 km through the tangent layer, leading to similar sensitivity to aerosol. Perhaps most important for merging purposes is the four years of mission overlap, with both instruments sampling the majority of the globe, providing a substantial amount of measurement overlap, both temporally and spatially.

3.3 Comparisons with SAGE II

3.3.1 Coincident Comparisons

Since the SAGE II and OSIRIS aerosol extinction products are not retrieved at the same wavelength, comparison of the two products is non-trivial. Either OSIRIS measurements must be converted to a SAGE II channel, or vice-versa. For this comparison study SAGE II measurements are converted to 750 nm using an interpolation in log-wavelength, log-extinction space (ie., the Ångström coefficient) between the SAGE II measurements at 525 and 1020 nm. While this provides a reasonable conversion factor, it is not without error, and this interpolation will tend to underestimate the true extinction by 8-12% percent, depending on the particle size distribution (see supplemental figure S2).

To test the agreement between SAGE II and OSIRIS 750 nm extinction profiles, coincident measurements were compared. Scans were considered to be coincident if the tangent point of the measurements were within $\pm 1^\circ$ latitude, ± 24 hours and ± 1000 km. If more than one scan was coincident only the closest in distance was used. The number of coincident measurements that meet this criteria depends on latitude, with sharp maxima near $\pm 60^\circ$ latitude. Typically, however, around 200 coincident scans are present for the four years of overlap for each 20° latitude bin. The SAGE II profiles are convolved using a triangular filter with a FWHM of 1 km to adjust the vertical resolution to that of OSIRIS which is approximately 2 km. This convolution has only a small effect on the mean differences, although does improve the standard deviations slightly. The OSIRIS version 5.07 extinction product is typically only used for altitudes where aerosol extinction does not exceed $2.5 \times 10^{-3}\,\mathrm{km}^{-1}$. However, the retrieval is still performed beyond this limit and including this data extends the OSIRIS

dataset to the tropopause. While this data is not typically used for stratospheric studies these lower altitudes can include a large amount of aerosols, and so are included in the work presented here. To avoid the largest outliers and clouds in the extended OSIRIS data, extinction values above $3 \times 10^{-2}\,\mathrm{km}^{-1}$ have been removed. This is also the approximate maximum level at which SAGE II can retrieve aerosol, and so helps to improve agreement between instruments.

Results are shown in Figure 3.3, with mean difference shown in black and standard deviation shown in gray. The 380 K surface and the thermal tropopause are derived from data from the NCEP database (Kalnay *et al.,* 1996), where the thermal tropopause is defined as the point at which the lapse rate falls below 2° C/km and hereafter is simply referred to as the tropopause. In the tropics and mid-latitudes agreement is quite good, typically within 10 % for the majority of the aerosol layer. At latitudes above 50°the agreement is poorer, with OSIRIS over-estimating extinction by around 25% at 15 km while underestimating at altitudes above 25 km. The cause of this general trend of overestimating at low altitudes and underestimating at high altitudes compared to SAGE II is currently unknown. Small particles, (Ångström coefficients > 3) were retrieved in the OSIRIS version 6.00 retrieval, without substantial change to the retrieved high-altitude extinction (typically less than 10% on average). Additionally, this bias persists under both forward and backscatter measurement conditions, suggesting that particle size is not the primary driver of the bias. The high altitude normalization is usually near 25 to 30 km at higher latitudes and this may also be decreasing the sensitivity to aerosols in the few kilometers below the normalization point. Altitudes below the tropopause exhibit much larger standard deviations and poor correlation (Figure 3.4) than altitudes above, but do not show substantially worse mean biases. This may be partially due to variability in the sampled air masses, although there are too few coincident measurements to compare substantially more restrictive criteria. Also worth noting is that no difference is seen in comparisons between SAGE II sunrise/sunset events, with any changes falling well below the standard deviations in Figure 3.3.

Correlations (r-value) between coincident SAGE II and OSIRIS measurements are shown in Figure 3.4. Generally correlation is better than 0.6 above the tropopause, even when biases between instruments are the largest. The notable decrease in correlation in the tropics around

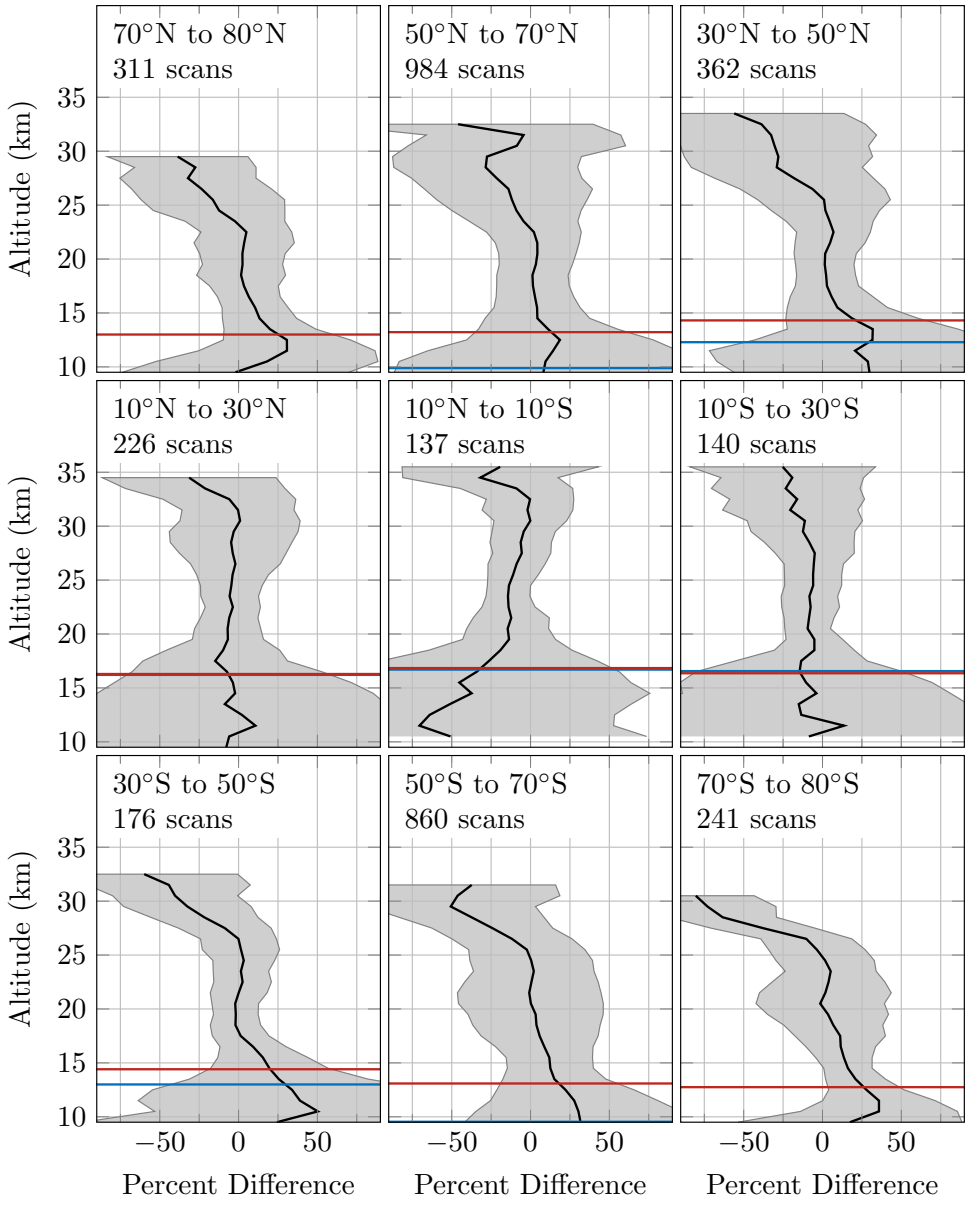

Figure 3.3: Comparison of coincident 750 nm extinction measurements at selected latitude bands. Percent difference calculated as (OSIRIS-SAGE II)/mean×100. Shaded regions show one standard deviation of the percent difference. Horizontal red and blue lines denote the average 380 K surface and tropopause respectively. In the tropics the blue line can be difficult to see as it lies nearly on top of the red line. Near the poles the mean tropopause (red line) is below 9.5 km

22-27 km is due largely to the particle size assumptions used in the OSIRIS retrievals. If the particle size is assumed incorrectly the retrieved aerosol extinction will have a dependence on the satellite measurement geometry. Due to the Odin orbit the scattering angle range is largest in the tropics, and this exhibits as a larger variance in the retrieved aerosol during these times (See Rieger *et al.* (2014) for a thorough discussion of this topic). In contrast, the natural variability in this region is relatively small, and the correlations are decreased as a result. Despite the poorer correlations in these regions, the agreement seen in Figure 3.3 is still within 10%.

3.3.2 OSIRIS Climatology

OSIRIS measurements now span over 14 years and cover much of the globe, providing a valuable dataset in their own right. Combined with the volume of measurements, (now over 800,000 profiles) this makes the production of an OSIRIS extinction time series at the native wavelength of 750 nm a worthwhile endeavour. For production of an OSIRIS time series, measurements were averaged into monthly bins with 5° latitude and one kilometer altitude resolution. This provides sufficient measurements in each bin, while keeping the bins small enough to avoid substantial spacial sampling biases. Extinction values were geometrically averaged to better capture the large variability in aerosol loading during the volcanically active periods. The top panel in Figure 3.5 shows the OSIRIS 750 nm extinction record between 10°N and 10°S. For reference the SAGE II data, averaged in the same way, are shown in the middle panel of Figure 3.5. In the SAGE II record the earlier years are dominated by Pinatubo eruption in 1991. Altitudes below 23 km often have extinctions too high to retrieve shortly after the eruption, visible as the missing block of data. Due to the sampling, months without data are also common. Although at a slightly different wavelength the OSIRIS time series shows all the same features as SAGE II during the overlap period, with the eruptions of Ruang/Raventador (late 2002) and Mt. Manam (early 2005) clearly visible in both. This is also evident in the aerosol optical depth, shown in the bottom panel. Here the SAGE II and and OSIRIS extinction have been integrated from the tropopause to 35 km. Although the absolute scales vary, both SAGE II and OSIRIS see similar increases in the relative magnitude of the AOD after the eruptions.

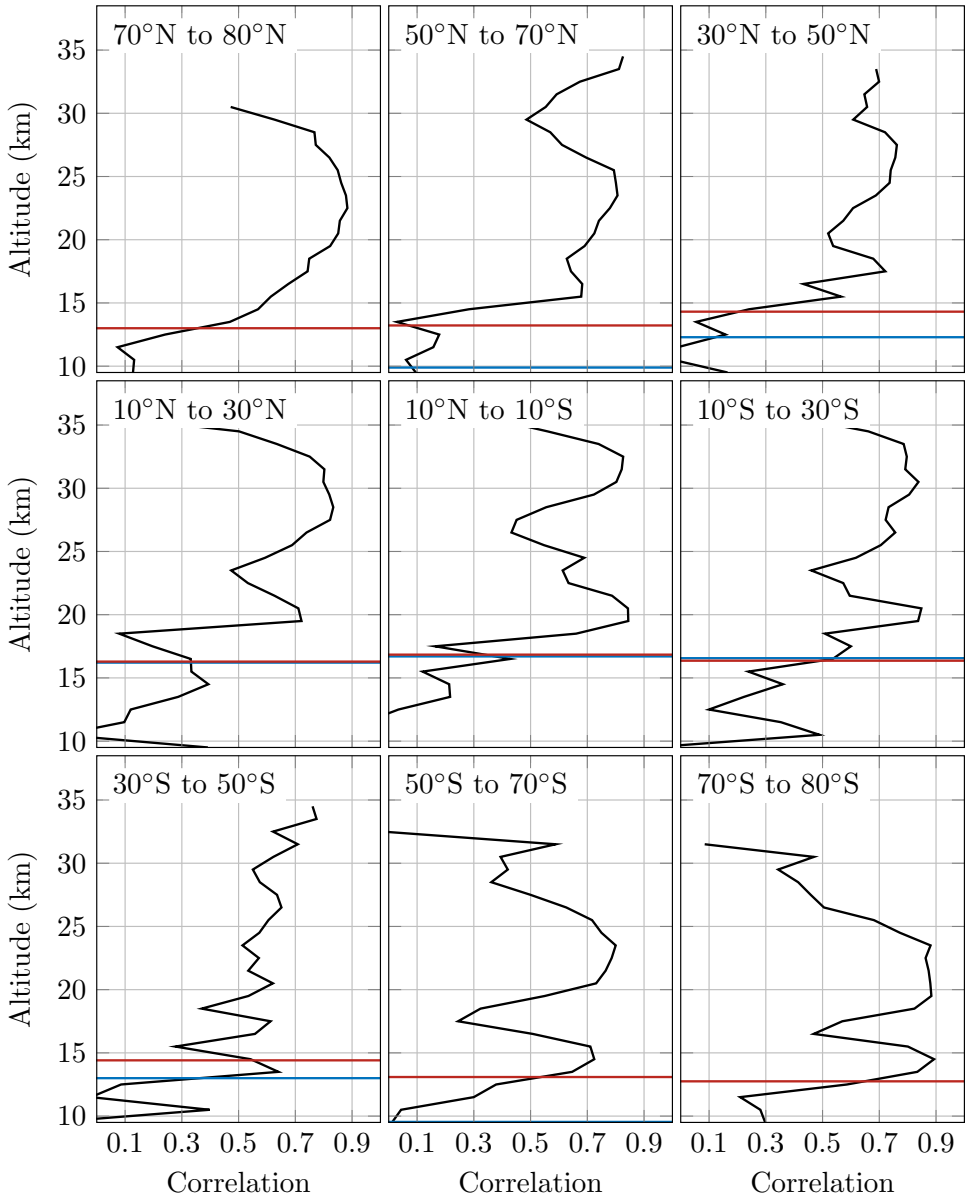

Figure 3.4: Correlation (r-values) of the coincident SAGE II and OSIRIS 750 nm extinction measurements. Horizontal red and blue lines denote the average 380 K surface and tropopause respectively.

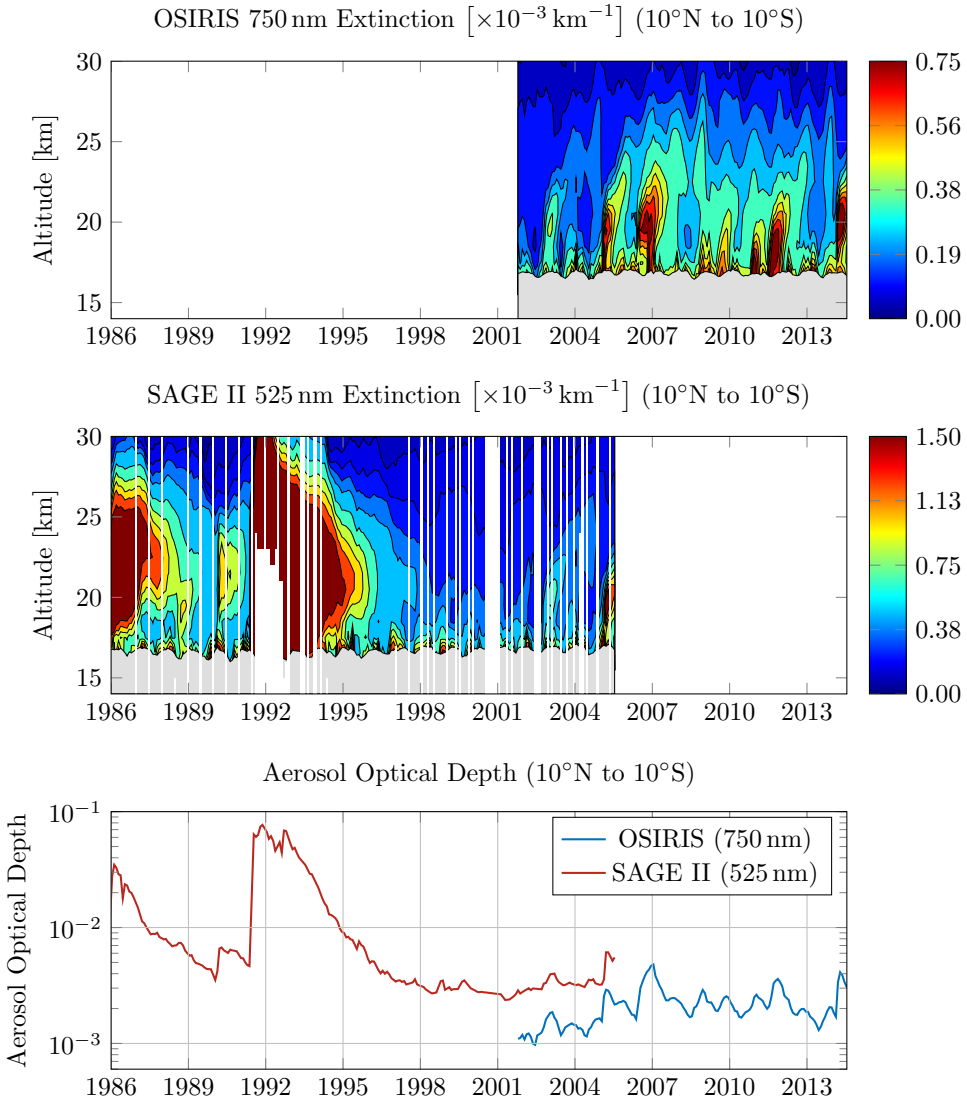

Figure 3.5: Top panel shows the monthly averaged OSIRIS aerosol extinction at 750 nm with altitudes below the tropopause shown in gray. Middle panel shows the monthly averaged SAGE II aerosol extinction at 525 nm. Bottom panel shows the OSIRIS and SAGE II aerosol optical depths, in blue and red respectively. Note the color scales are different for the OSIRIS and SAGE II plots due to the wavelength differences.

3.4 Merging Approach

The long duration of both the SAGE II and OSIRIS missions, as well as the four year overlap in measurements, provides an excellent opportunity to construct a single 30-year time series of altitude and latitude extinctions by merging the two data sets. Due to the heritage and vast number of previous studies using the SAGE II 525 nm time series, (eg., Thomason *et al.* (2008), Thomason *et al.* (2010), and Ernst *et al.* (2012)), as well as the standard usage of mid-visible optical depths in the modelling community (Driscoll *et al.,* 2012; Oman *et al.,* 2005; Ammann *et al.,* 2003), it is desirable not to modify the SAGE II data set in the merging with OSIRIS. The merging approach is then a two-step process: (1) translate the OSIRIS 750 nm extinction measurements to 525 nm, and (2) characterize and remove any altitude and latitude dependent bias in the OSIRIS data set using the four years of mission overlap.

The wavelength translation of the OSIRIS data from 750 nm to 525 nm requires knowledge or assumption of the particle size distribution. A very simplistic approach is to use the particle size distribution that is internally assumed in the OSIRIS retrieval, and is consistent with typical balloon-borne optical particle counter measurements in the stratosphere (Deshler *et al.,* 2003). This corresponds to an Ångström coefficient of 2.3, calculated from a lognormal particle size distribution with a mode radius of 80 nm and 1.6 mode width. Although it is feasible to consider a spatially and temporally varying particle size distribution for the conversion, robust measurements of this sort are simply not available. Our philosophy is to use this very simple scaling along with in-situ balloon data, though sparse, and the comparison to SAGE II during the four years of overlap to estimate the potential variability in this scaling as an uncertainty estimate in the merged OSIRIS data set.

With a constant Ångström coefficient of 2.3, the wavelength conversion is straightforward, with the OSIRIS extinction being multiplied by a conversion factor of 2.27 to produce extinction values at 525 nm. The 525 nm OSIRIS data are then bias corrected such that the average monthly mean is equal to that of SAGE II for each latitude-altitude bin. Mathematically, this is simply,

$$k_{\text{OS corrected}} = k_{\text{OS}} \frac{\text{mean}(k_{\text{SAGE}})}{\text{mean}(k_{\text{OS}})}$$

applied at each altitude and latitude bin. Where k is the 525 nm extinction and the bias correction is the ratio of the mean extinction values. Note that this bias correction does not change with time, so the time dependence of the OSIRIS measurements are unchanged by this correction. In addition to biases in the OSIRIS retrievals this scaling also corrects some of the deficiencies in using a constant Ångström coefficient with altitude and latitude. Any time-independent offset in the OSIRIS data, introduced by the retrieval or an incorrect wavelength conversion, will be removed by the bias correction.

The bias correction applied to OSIRIS data are shown in panel A of Figure 3.6. This picture largely agrees with the coincident comparisons shown in Figure 3.3, with the tropics agreeing well over the bulk of the stratosphere and a general trend of OSIRIS underestimating at higher altitudes while overestimating at lower altitudes. The exception to this is just above the tropopause in the tropics where OSIRIS has a slight low bias with respect to SAGE II due to cloud contamination. The OSIRIS limb scatter retrievals are more likely to saturate under cloudy conditions than the SAGE II occultation retrievals, leading to fewer values of very high extinction. Additionally, the assumed microphysics in the OSIRIS retrieval do not apply to clouds, leading to potentially large biases.

To test whether this simple scale factor corrects the biases in the OSIRIS retrievals the distributions of bias corrected OSIRIS extinction measurements at 525 nm can be compared to those of SAGE II at 525 nm. To provide sufficient measurements for comparison 10°latitude and one km altitude bins are used. However, the temporal sampling in each latitude bin is still quite different between the two instruments, as can be seen in Figure 3.2. To avoid temporal biases the measurements are weighted so that both OSIRIS and SAGE II have the same number of weighted samples in each one month period. Probability density functions of the weighted measurements can then be constructed from summing the weights in each extinction bin. For a given altitude and latitude the weight for an OSIRIS measurement in month j is the number of SAGE II measurements in that one month bin. Similarly, the weight for a SAGE II measurement in month j is the number of OSIRIS measurements in that bin, again for a particular altitude and latitude. While the following analysis of measurement distributions is inherently qualitative, it does provide an indication of whether the scaling method is appropriate, and locations where more systematic biases may be present.

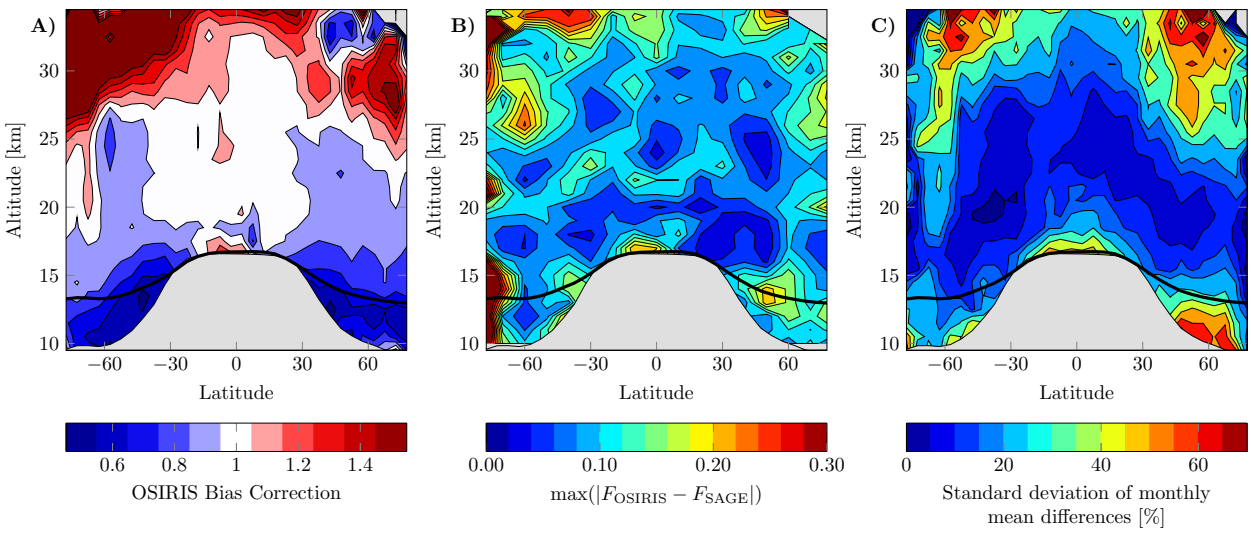

Figure 3.6: Panel A shows the scale factor applied to OSIRIS data as a function of latitude and altitude to perform the bias correction. Panel B shows the agreement between SAGE II and bias corrected OSIRIS extinction distributions, as indicated by the Kolmogrov-Smirnov metric. Panel C shows the standard deviation of percent differences between monthly mean values. Areas below the average tropopause are shown in gray, with the average 380 K potential temperature shown in black.

Figure 3.7 shows the OSIRIS and SAGE II extinction probability and cumulative distributions at four locations. Generally, agreement is good with both instruments measuring similar distributions of extinction values. This is true even when the distributions are heavily skewed, or even bimodal with both instruments capturing the long, low extinction tails in panels A and D as well as a small secondary peak in extinction around $10^{-3}\,\mathrm{km}^{-1}$ in panel C.

While this level of agreement is typical, there are some locations where a simple scaling to match the monthly means is not sufficient to align the measurement distributions. Four areas that display the worst agreement between measurement distributions are shown in Figure 3.8. In the high northern latitudes near 25 km both OSIRIS and SAGE II measure bimodal extinction distributions, and while measurements of higher extinction agree well, OSIRIS underestimates the values of small extinction. A similar feature occurs near the tropopause around 13 km altitudes. In the tropics near 23 km, and above 25 km around 60°S SAGE II measurements show very low variability that is not well matched by the OSIRIS measurements. These discrepancies are thought to be largely due to incorrect particle size

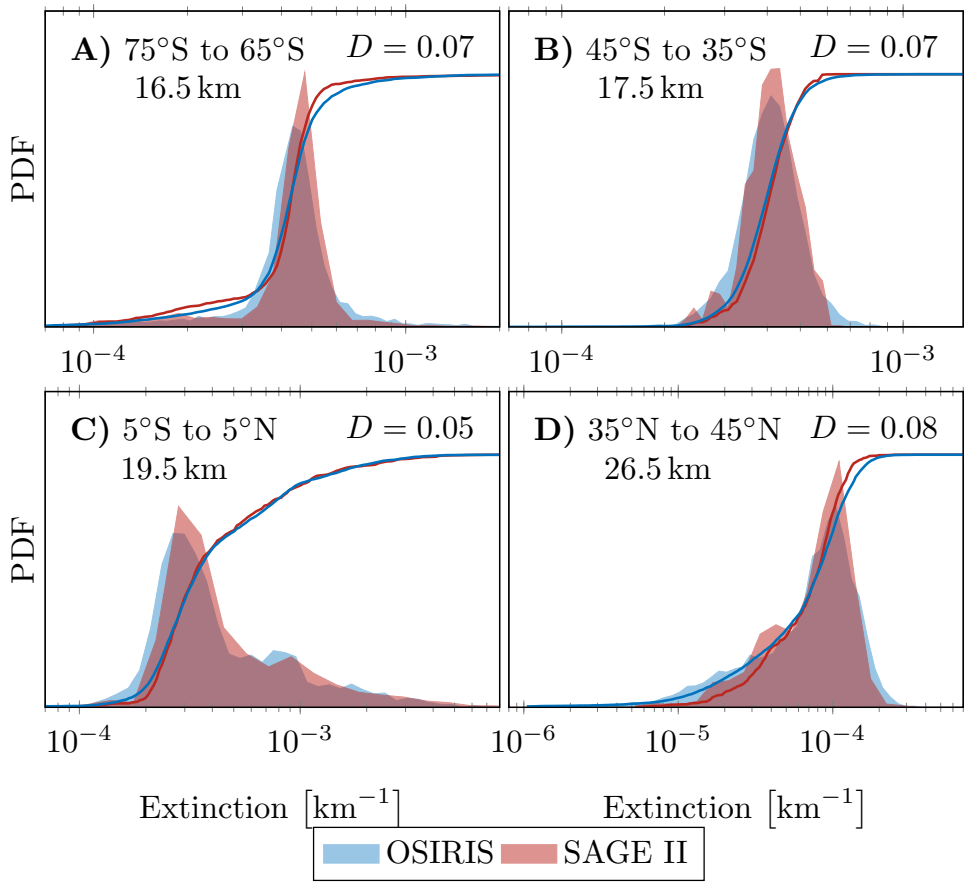

Figure 3.7: Measurement distributions of SAGE II and bias corrected OSIRIS 525 nm extinction retrievals at four representative latitude and altitude locations. Shaded regions show the probability distribution, with the solid lines showing the cumulative distributions. The D value in the upper right is the Kolmogrov-Smirnov metric computed on the cumulative distributions.

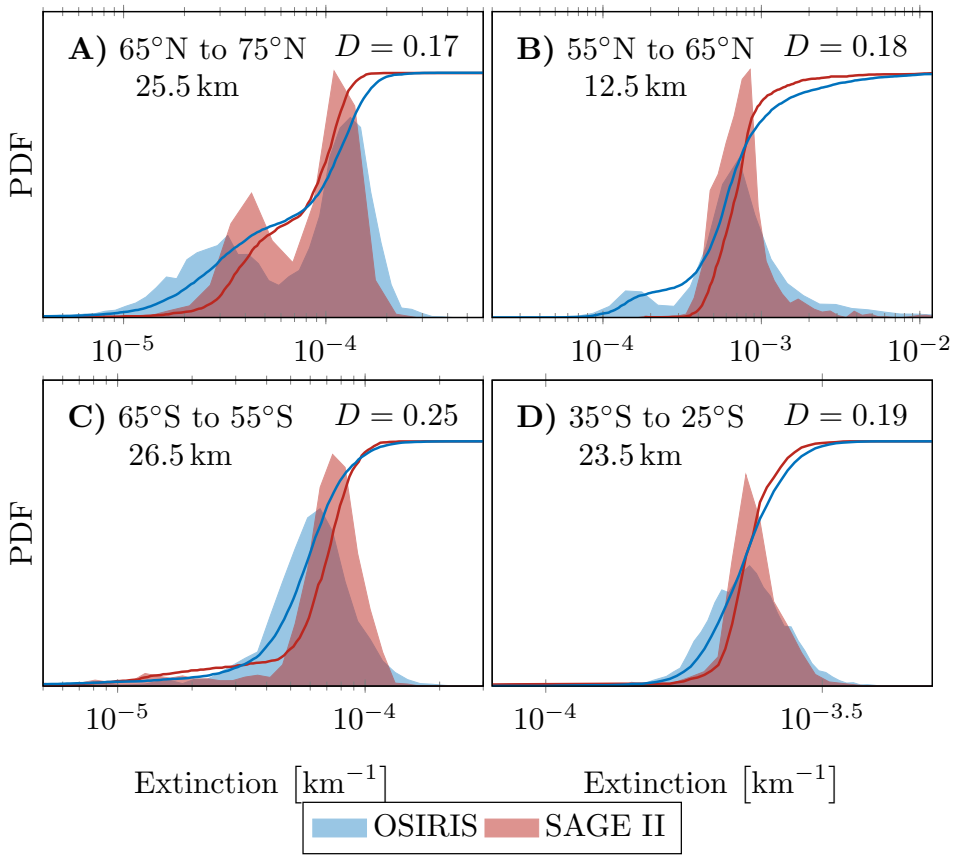

Figure 3.8: Same as 3.7, except at four locations that show the worst agreement after the bias correction has been applied.

assumptions in the OSIRIS retrieval. This is the same effect that caused the decrease in correlations in Figure 3.4 around 25 km altitudes in the tropics..

To see the extent of the agreement, and where problem areas occur, it is convenient to use a metric that compares two empirical distributions. One common statistical metric is the Kolmogorov-Smirnov (KS) test, which compares the maximum difference between two empirical cumulative probability distributions F_1 and F_2,

$$D = \max\left(|F_1 - F_2|\right).$$

While designed to test whether two empirical distributions have been drawn from the same underlying continuous distribution, the metric, D, provides a convenient measure of the similarity of two distributions, without the need to parameterize or bin the data. The D value as a function of altitude and latitude is shown in panel B of Figure 3.6. The

problem areas shown in Figure 3.8 are clearly visible in Figure 3.6, panel B, as increases in the Kolmogrov-Smirnov metric, D. Also visible is the generally good agreement between measurement distributions. As reference, the D values for the probability distributions shown in Figures 3.7 and 3.8 are given in the upper right corner of each panel. A few locations near the southern pole and altitudes higher than 30 km show poorer agreement, however this is due largely to the small number of samples in each bin, with typically only 2-4 months overlapping in these regions. Overall, this shows that the simple bias correction used to merge the data sets does a good job of capturing not only the mean values, but the measurement distributions as well.

3.5 Merged Time Series

The merged record is provided as a monthly averaged stratospheric aerosol extinction time series at 5°latitude and one kilometer altitude resolution. Also included at the same resolution is the uncorrected OSIRIS time series at 750 nm. These data sets are available for download as hdf5 files, at `odin-osiris.usask.ca` and will be updated periodically as new OSIRIS data become available. Additional details of the format are provided in the supplemental information, Text S1. The top panel of Figure 3.9 shows the merged aerosol extinction at 525 nm between 10°N and 10°S. This is a fairly typical slice of the extinction data provided in the merged product, although coverage does decrease at higher latitudes due to the sampling of the satellites, and missing months are more common.

This altitude, and latitude resolved time series can easily be used to create aerosol optical depths, as is shown in the middle panel of Figure 3.9. This panel shows the aerosol extinction at 525 nm integrated from 1 km above the 380 K surface to 35 km, ie. the aerosol optical depth, as a function of latitude. In both the extinction and aerosol optical depths the large volcanic eruptions of Nevado del Ruiz in 1985 and Pinatubo in 1991 are evident, as are several smaller eruptions in the last decade including Manam (2005), Kasatochi (2007), Sarychev (2008), Merapi (2010), Nabro (2011) and Kelut (2014).

For reference, results from the dataset produced here can also be compared with records from Sato *et al.* (1993) and Vernier *et al.* (2011). The aerosol optical depth record produced by

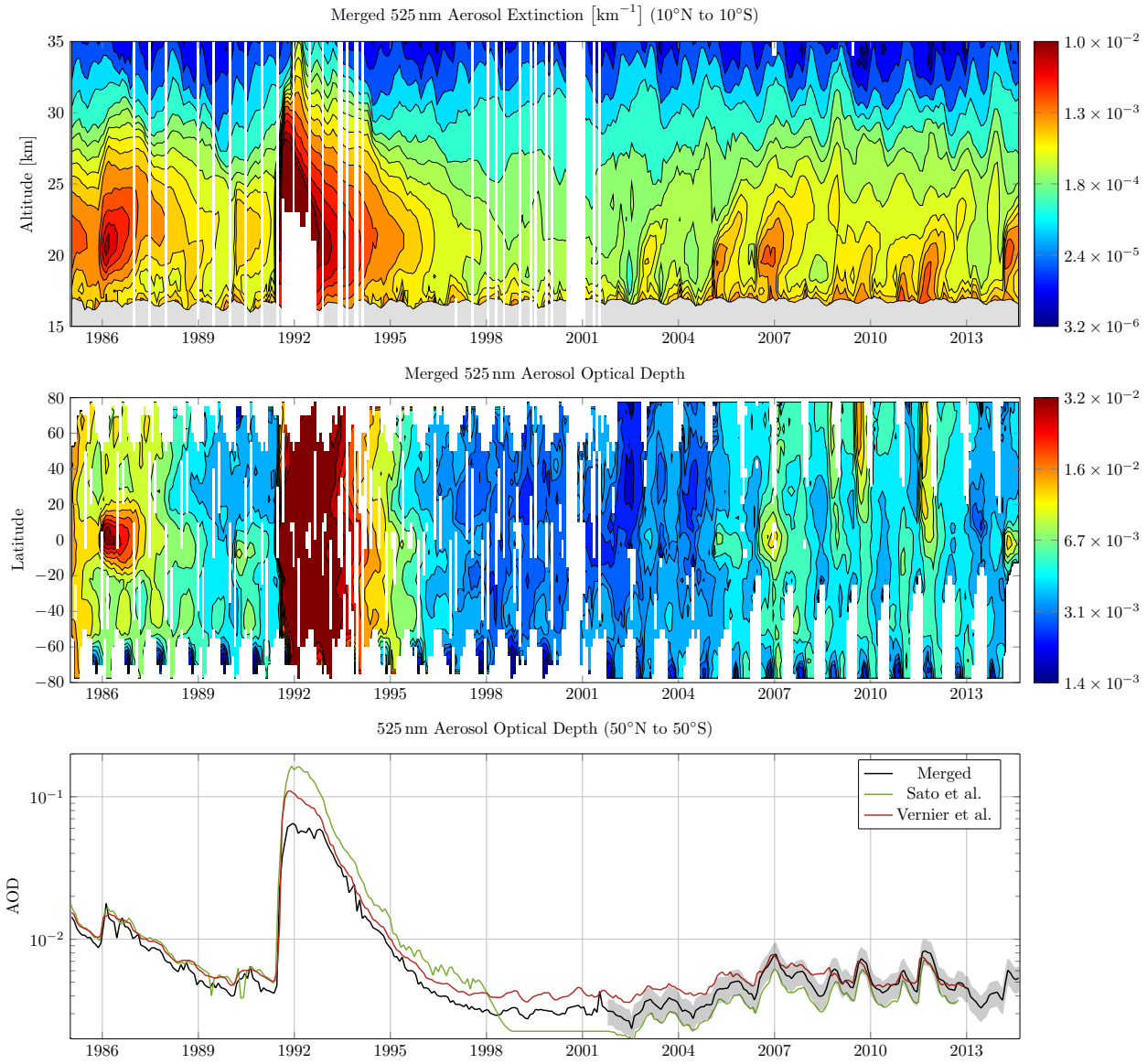

Figure 3.9: Top panel shows the merged 525 nm extinction averaged from 10°N to 10°S. Regions with missing data are shown in white. The middle panel shows the merged aerosol optical depth data set, from 1 km above 380 K to 35 km. Bottom panel shows the merged 525 nm aerosol optical depth between 50°S and 50°N calculated from 1 km above the 380 K surface to 35 km in black. The shaded region indicates the estimated error from the OSIRIS measurements. The Sato et al., and Vernier et al., data sets are shown in green and red respectively for comparison, although the altitude integration limits vary as does the filling method used for the Pinatubo time period (see text).

Sato et al. which used the version 6.2 SAGE II aerosol data among other sources is provided at 550 nm from http://data.giss.nasa.gov/modelforce/strataer. To account for this small wavelength difference the Sato et al. record has been scaled to 525 nm using a lognormal particle size distribution with mode width of 1.6 and mode radius of 80 nm. Due to the small wavelength shift the conversion is relatively insensitive to the particle size choice, with Ångström coefficients between 1 and 3 producing extinctions within 5% of the value used here. This record was originally constructed using several historical sources as well as the SAGE II data, and has since been updated using the OSIRIS data. For their analysis both SAGE II and OSIRIS were converted to 550 nm using a $1/\lambda$ relation, stratospheric aerosol optical depth was then calculated from 15 to 35 km in 5 km altitude bins using 7.5° latitude bins.

The Vernier et al. record was produced using primarily SAGE II, GOMOS (Vanhellemont *et al.,* 2010), and CALIPSO (Winker *et al.,* 2010) data and provides aerosol optical depths integrated from 15 km to 35 km altitude. An important note is that both the Sato et al. and Vernier et al. records have used additional data to fill the missing gaps after the Pinatubo eruption, when no SAGE II data are available. See Sato *et al.* (1993) and Thomason *et al.* (2006) for details on the filling techniques and limitations. As this work concentrates on extending the SAGE II extinction measurements with OSIRIS data, the missing SAGE II values are not filled here and profiles with missing data are flagged in the provided files. However, the data set provided is altitude and latitude resolved, allowing users to fill gaps with methods best suited to their work.

The bottom panel in Figure 3.9 shows the mean aerosol optical depth between 50°N and 50°S for the three aerosol records discussed here. In black is the merged SAGE II/OSIRIS integrated from 1 km above the 380 K potential temperature to 35 km. This was chosen to avoid the biases caused by clouds in the OSIRIS data set. For reference, a 20% error bar has been added to the AOD, representing the estimated uncertainty in the OSIRIS aerosol due to particle size assumptions. Determination of this value is discussed in the following section. Shown in green is the Sato et al. record, with the Vernier et al. record shown in red. Prior to 2001 the merging presented here is systematically lower than the other records. This is due to the altitude limits chosen for optical depth integration. The fixed 15 km of

Sato et al. and Vernier et al. extend below the 380 K surface in the tropics, increasing the aerosol loading. This effect is more pronounced in the early part of the 21^{st} century, when stratospheric extinction is small. The difference in filling (or lack thereof) between the three data sets is also apparent at the peak values of optical depth following the Pinatubo eruption.

Post 2001, the Sato et al. record shows all the same features as the merging work here since it consists entirely of OSIRIS data. However, Sato et al. is systematically lower by approximately 20% due to the lack of bias correction and $1/\lambda$ wavelength conversion. Between 2001 and 2006 the Vernier et al. AOD is slightly higher than the merged product, but with a magnitude that is consistent with the difference during the purely SAGE II period. In contrast, the agreement post 2006 is better, with differences typically much smaller than 20%, suggesting a changing bias between the records. Two factors likely contribute to this effect. Post 2006 the Vernier et al. record uses CALIPSO data, with GOMOS being used prior. As a backscatter instrument CALIPSO is also sensitive to particle size assumptions. As well, these instruments use very different measurement techniques (lidar vs. stellar occultation) and are sensitive to different loading conditions. Also, several moderate volcanic eruptions are evident post 2006, and this may be changing the particle size, and with it the OSIRIS bias.

3.6 Uncertainty Estimate for the Merged OSIRIS Time Series

The assumption of a constant particle size causes uncertainty in two ways. First, is the error in the 750 nm retrieval due to an incorrect phase function in the forward model. Second, is the conversion of the 750 nm extinction back to 525 nm. These errors are of course not independent, and are both corrected, to a degree, by the bias correction applied above. How well they are corrected depends on the variability of the true particle size, and how much this affects the retrieval and the wavelength conversion. The effect on the wavelength conversion is simple to estimate given known particle sizes, however determining the true particle size variability and its effect on the retrieval is considerably more complicated.

Although global measurements of stratospheric aerosol particle size are limited, the op-

tical particle counters launched by the University of Wyoming provide a good mid-latitude historical record, both during and after the SAGE II mission. The optical particle counters are used to derive several particle size parameters including the mode radius and mode width for both fine and coarse mode particles. These parameters were used to determine the Ångström coefficient as a function of altitude during the SAGE II/OSIRIS overlap period as well as between 2005 and 2013. Results are shown in Figure 3.10. The mean profiles for the fine mode parameters are relatively constant over the OSIRIS mission, with mode radius seeing a slight increase of approximately 0.01 to 0.02μm and a decrease of 0.1 to 0.2 in the mode width at altitudes below 20 km. However, the standard deviation has increased, particularly for the mode radius, likely indicating volcanic events with larger particles. This trend also holds for the Ångström coefficient which is consistently close to 2.3 below 25 km throughout the duration of the OSIRIS mission.

Overall, the variability in the Ångström coefficient is typically ± 0.5 for most altitudes with the mode radius varying between 40 and 120 nm and the mode width varying between 1.2 and 2. Additionally, the Wyoming data also shows a coarse mode, with considerably larger particles. Using these values we can estimate the error in the OSIRIS retrieval and wavelength conversion through a simulation study. The error in the retrieved product depends on the true particle size, but also measurement geometry, the surface albedo and extinction levels, making full exploration of the error space impractical. However, to estimate uncertainty in the more extreme cases, 10 scenarios each with 18 geometries and albedo values spanning the OSIRIS range were tested. This includes four particle size distributions with Ångström coefficients between approximately 2 and 3, at both volcanic and background extinction levels, as described in Table 1. Additionally, scenarios 9 and 10 test the retrieval when the "true" particle size is equal to the fine mode as measured by Deshler et al. between 2001 and 2005, and as shown in Figure 3.10.

For this study radiances were modelled using SASKTRAN with the values in Table 1 as the "true" atmosphere. These radiances were then processed using the standard OSIRIS retrieval algorithm (assuming a constant particle size of 80 nm and 1.6 mode width), and extinctions converted to 525 nm using an Ångström coefficient of 2.3, as in the analysis above. This study therefore estimates both the retrieval error, and the error due to the

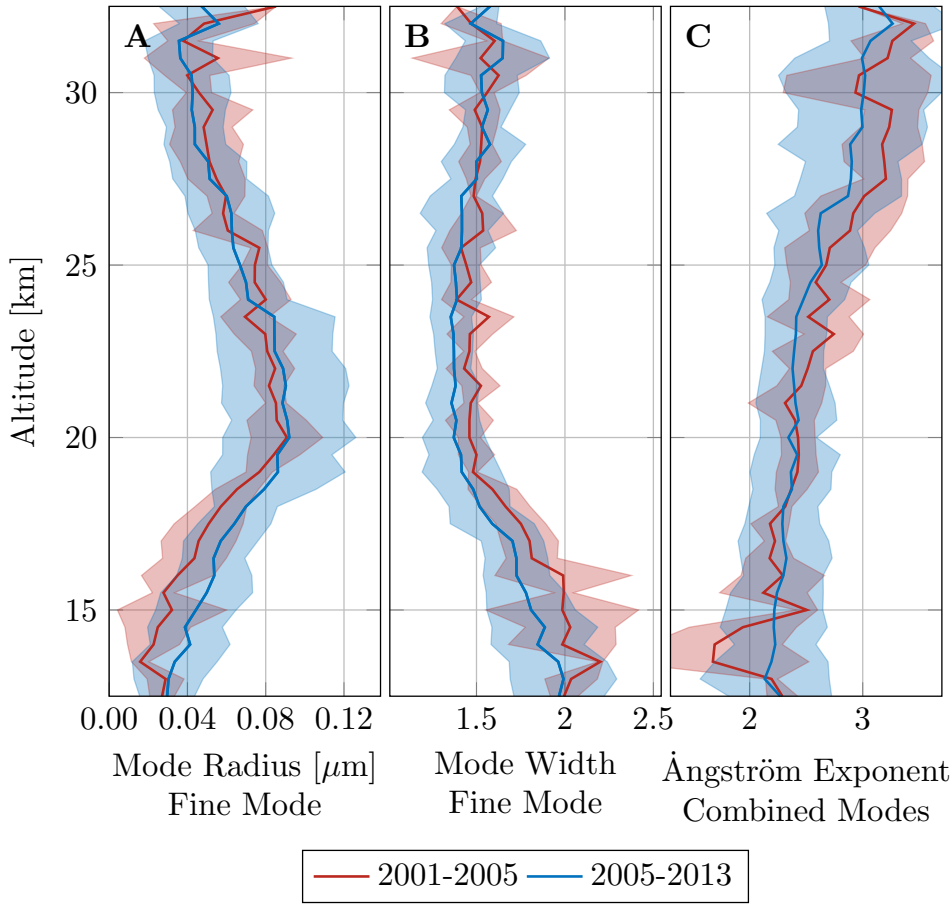

Figure 3.10: Data from the balloon measurements taken by the University of Wyoming. Panel A shows the mean median radius of the fine mode. Shaded regions show one standard deviation. Panel B shows the same with mode width. Panel C shows the the Ångström coefficient using both the fine and coarse mode distributions. In blue are the average measurements before 2005, with measurements from 2005-2013 shown in red.

Scenario	Extinction	Fine Mode		Coarse mode		Mode Fraction	Ångström	Mean Error [%]
		r_g [nm]	σ_g	r_g [nm]	σ_g			
1	Background	120	1.25	-	-	0	2.91	6.0
2	Background	120	1.25	300	1.15	0.5	2.24	-2.7
3	Background	40	1.80	-	-	0	2.55	-4.4
4	Background	40	1.80	300	1.15	0.5	2.02	-6.4
5	Volcanic	120	1.25	-	-	0	2.91	2.0
6	Volcanic	120	1.25	300	1.15	0.5	2.24	-2.0
7	Volcanic	40	1.80	-	-	0	2.55	-6.7
8	Volcanic	40	1.80	300	1.15	0.5	2.02	-6.4

Table 3.1: Scenarios used in the uncertainty study. Volcanic refers to extinction levels typical after the Nabro eruption, while Background is the mean extinction profile from 2002. Mode fraction is calculated as the extinction of the coarse mode divided by the total extinction, both at 750 nm. Mean error is calculated as the average error between 15 and 35 km from all geometries and albedo values for a scenario.

wavelength conversion in a properly coupled way. Typically, individual simulated retrievals are biased by no more than 20%, with the largest errors occurring under conditions when the Ångström coefficient is close to 3, and biases can exceed 50% for individual geometries. However, even in these worst cases the mean bias over all geometries and albedo values was less then 10%. Overall, the OSIRIS 525 nm extinctions biases due to particle size, even during the moderately volcanic periods of the last decade are unlikely to exceed to 20% on average. Although this occurring under certain measurement geometries and particle size conditions cannot be ruled out completely.

The uncertainty for the 2001-2005 period can also be estimated empirically by comparing the bias corrected monthly mean OSIRIS values to those of SAGE II. If the true particle size varies with time this will not be captured by the constant bias correction, and exhibit as a difference in the monthly averaged SAGE II and OSIRIS extinctions. Figure 3.11 shows the SAGE II bias corrected OSIRIS extinction time series at several altitudes and latitudes for the overlap period. Both records track the variability of the aerosol extremely closely, with seasonal cycles visible at high latitudes, volcanic eruptions at lower altitudes, and QBO at higher altitudes, all with similar magnitudes. Overall, the OSIRIS and SAGE II extinction values typically agree within 15%, even after the small volcanic eruptions of Ruang/Raventador in 2002 and Mt. Manam in 2005. The merged aerosol extinction is shown in black. When both OSIRIS and SAGE II are available the merged record is simply the average of the two measurements.

Figure 3.6, panel C, shows the standard deviation of the percent differences between monthly averaged, SAGE II and bias corrected OSIRIS data. For the bulk of the stratosphere monthly means agree very well, with standard deviations typically less than 15%, agreeing well with the error values from the simulation study. The exception to this is just above the tropopause in the tropics and below the 380 K surface at higher latitudes. Differences at these low altitude may not be due to particle size, but differences in the sampling. While scale factors and standard deviations are larger in this region, the shape of the measurement distributions still agree fairly well, suggesting both instruments are measuring similar conditions, only at different times, possibly due to the large variability of aerosols in these regions, exacerbated by cloudy conditions.

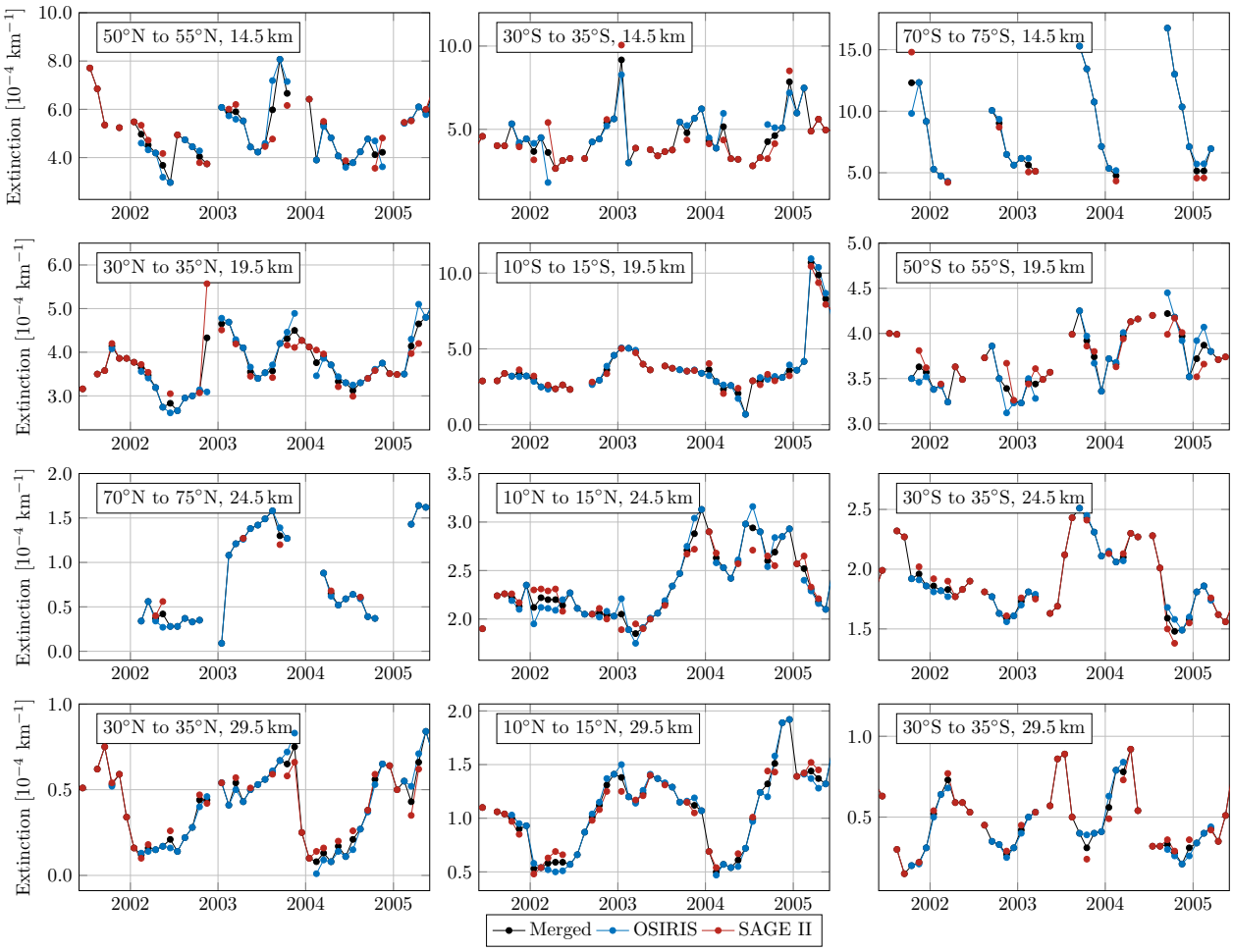

Figure 3.11: Examples of the agreement between SAGE II and bias corrected OSIRIS monthly mean 525 nm extinction values for a variety of altitude and latitude bins. SAGE II is shown in red with the OSIRIS in blue. The merged data set, which is the average of the two, when available, is shown in black.

Together the three panels in Figure 3.6 show where the merging is most reliable and where improvements are possible. Regions that have good monthly mean agreement but poorer agreement between measurement distributions are likely more affected by particle size assumptions, providing good measures of monthly variability but with changing biases as particle size and measurement geometries change. On the other hand, regions with high standard deviations but good agreement between distributions, such as those near the tropopause, may be reliable over longer time scales but have too dissimilar sampling to have reliable monthly means.

3.7 Upper Troposphere Lower Stratosphere Aerosols

The OSIRIS time series agrees well with SAGE II over the majority of the stratosphere, however comparisons near the tropopause are complicated by the effects of clouds on the retrievals, and biases in these regions are more difficult to estimate. Ridley *et al.* (2014) found that aerosol between 15 km and the tropopause can contribute a substantial fraction of the total stratospheric aerosol optical depth in the mid-to-high latitudes, making accurate aerosol measurements in the UTLS region an important component of an aerosol climatology. In the past, OSIRIS measurements have typically been used only above either 15 km or the 380 K surface to avoid cloud contamination. While a cloud clearing technique has been developed for the SAGE II data (Thomason *et al.,* 2013), the wavelength range of OSIRIS does not allow for such accurate discrimination. In the tropics, between approximately 20°N and 20°S the presence of clouds obscures measurements below the 380 K surface and the tropopause, located at approximately 17 km. Altitudes below the 380 K surface, but above the tropopause are considerably cleaner outside of the tropics. However, enhancements are often still seen at mid-to-high latitudes. These enhancements are much more pronounced after volcanic events, so are likely partially due to aerosols, however the cloud/aerosol fraction cannot be determined by OSIRIS alone, and future analysis would benefit from the inclusion of cloud discriminating instruments.

Figure 3.12 shows the fraction of aerosol optical depth that is due to the layer between 15 km and the tropopause as determined from the merged aerosol record. In the tropics

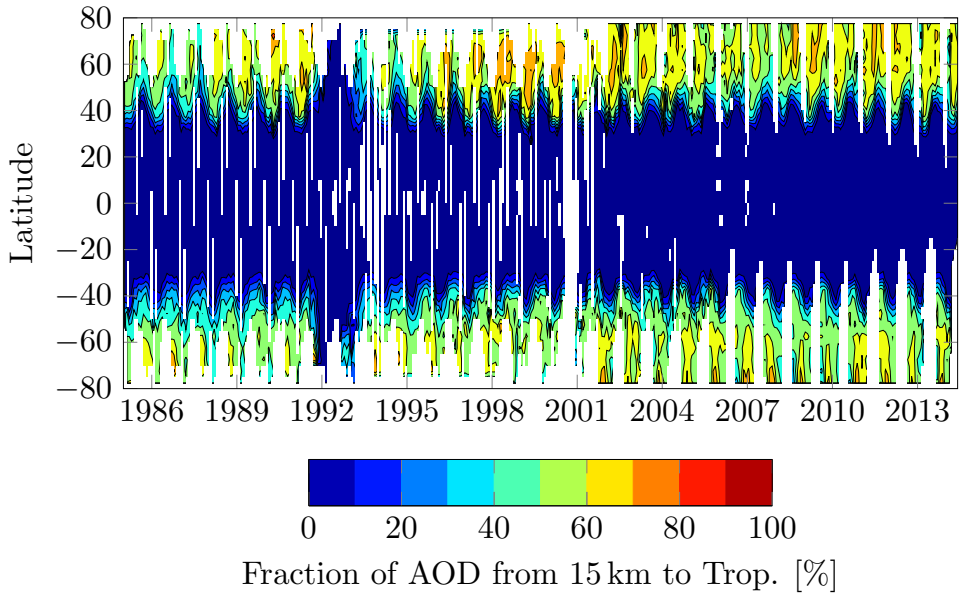

Figure 3.12: Fraction of the total stratospheric aerosol column that is between the tropopause and 15 km altitude. Computed as the aerosol optical depth from 15 km to the tropopause divided by the total aerosol optical depth from 15 km to 35 km.

where the tropopause is higher than 15 km the difference has been set to zero. Regions where 50% of the aerosol loading is from below 15 km are common, especially in the higher latitudes and Northern hemisphere. While these results are undoubtedly contaminated by clouds to some degree, the relative fraction of aerosol in the UTLS region agrees well with the results found by Ridley *et al.* (2014) which are derived from ground-based lidar and AERONET and less likely to be affected by clouds. Overall, this reiterates the need for high quality aerosol measurements at these altitudes to accurately quantify the total stratospheric aerosol budget.

3.8 Conclusions and Recommendations

In general the OSIRIS aerosol dataset agrees very well with that of SAGE II with typical biases less than 15%. Biases between the two instruments are generally well corrected by a simple scale factor, and monthly means are consistent across all latitudes from 18 to 30 km. Outside of the tropics this can be pushed somewhat lower to 14.5 km, and even to the tropopause although cloud contamination is an issue this low. While these results

are promising this analysis also highlights the need for caution when using this data set in certain locations. Some sampling and/or instrument biases are likely in the high latitudes, making the scale factor used less reliable, particularly outside of the overlap time period. In addition, the end of the SAGE II mission in 2005 precludes comparisons during periods of higher aerosol loading, when different OSIRIS biases may be present due to changing aerosol microphysics, although estimated errors are not expected to be substantially larger.

Overall, this presents a good start to a merged aerosol data product, but could likely benefit substantially from the inclusion of additional independent satellite datasets. The work by Vernier *et al.* (2011) shows good agreement, suggesting a merged product using SAGE II, GOMOS, CALIPSO and OSIRIS would be beneficial. CALIPSO measurements are best during night-time conditions, when OSIRIS cannot take measurements, providing a natural complement to improve latitude coverage. Although CALIPSO also requires some assumptions on aerosol microphysics due to the nature of backscatter measurements, comparisons between CALIPSO and OSIRIS could provide valuable information on the reliability of the scaling used in later years, as well as possible causes of the bias between the two instruments. Additionally, the cloud discrimination capabilities of CALIPSO could greatly improve the measurements just above the tropopause and in the UTLS region. The aerosol in this region is an important fraction of the total aerosol budget, particularly after small volcanic eruptions such as those that have occurred in the last decade, and improved retrievals here would greatly benefit the aerosol climatology. Combining these instruments into a single dataset would provide improved coverage and reliability in locations and years when OSIRIS merging is either difficult or impossible with SAGE II alone.

Chapter 4

A study of the approaches used to retrieve aerosol extinction, as applied to limb observations made by OSIRIS and SCIAMACHY

[1]Rieger, L. A., [2]Malinina, E. P., [2]Rozanov, A. V., [2]Burrows, J. P., [1]Bourassa, A. E., and [1]Degenstein, D. A.: A study of the approaches used to retrieve aerosol extinction, as applied to limb observations made by OSIRIS and SCIAMACHY, Atmos. Meas. Tech., 11, 3433-3445, https://doi.org/10.5194/amt-11-3433-2018, 2018.

[1]Institute of Space and Atmospheric Studies, University of Saskatchewan, Saskatoon, Canada
[2]Institute of Environmental Physics, University of Bremen, Bremen, Germany

Merging the SAGE II and OSIRIS records suggested that while the two satellites provided remarkably consistent measurements during the overlap period of 2001 to 2005, unanswered questions about the datasets remained. OSIRIS agreed well with SAGE II over the bulk of the Junge layer, but showed low biases at higher altitudes and latitudes. Compounding this, the scarcity of measurements with which to compare after SAGE II ceased operation makes quantification of the biases difficult during periods more affected by volcanic eruptions. Comparisons with the merged SAGE II-CALIPSO optical depth show systematic shifts after 2006, but attribution is difficult as both the measurement technique and volcanic loading changed during this transition period. The underlying causes of inter-instrument differences were not resolved in Rieger *et al.* (2014), but to improve agreement between instruments and better understand limb scattering aerosol measurements they need to be investigated, and

this forms the second component of this work.

To help investigate errors arising from the OSIRIS measurements versus the retrieval algorithm and a priori assumptions, a second limb scattering instrument, SCIAMACHY is employed. SCIAMACHY was selected as it shares many similarities with OSIRIS, including comparable wavelengths, vertical sampling, spatial coverage and 10 years of overlapping measurements from 2002 to 2012. However, SCIAMACHY occupies a different orbit than OSIRIS, resulting in different measurement geometries. Additionally, the SCIAMACHY retrievals use a different retrieval algorithm and radiative transfer model. This allows for the isolation of differences due to retrieval techniques and radiative transfer models along with modelling studies for investigation of how the scattering angle couples into the retrieval through the aerosol phase function.

This work began as a proposal I wrote to the German Academic Exchange Service (DAAD) to investigate differences between the OSIRIS and SCIAMACHY datasets. Co-authors on the paper helped to support the writing of the proposal and it would not have been successful without them. Additionally, as a collaborative work, not all of the research presented in the following paper was conducted by me. The SCIAMACHY aerosol dataset used in this work and the majority of retrievals involving SCIATRAN were performed by the IUP team. Otherwise, the retrievals using SASKTRAN, radiative transfer simulations, analysis, figure and manuscript preparation, and paper revisions were performed by me. That said, this work would not be what it is without the input of my co-authors who were instrumental in helping design experiments, improving the analysis and editing drafts of the manuscript.

4.1 Abstract

Limb scatter instruments in the UV–vis spectral range have provided long-term global records of stratospheric aerosol extinction important for climate records and modelling. While comparisons with occultation instruments show generally good agreement, the source and magnitude of the biases arising from retrieval assumptions, approximations in the radiative transfer modelling and inversion techniques have not been thoroughly characterized. This paper ex-

plores the biases between SCIAMACHY v1.4, OSIRIS v5.07 and SAGE II v7.00 aerosol extinctions through a series of coincident comparisons as well as simulation and retrieval studies to investigate the cause and magnitude of the various systematic differences. The effect of a priori profiles, particle size assumptions, radiative transfer modelling, inversion techniques and the different satellite datasets are explored. It is found that the assumed a priori profile can have a large effect near the normalization point, as well as systematic influence at lower altitudes. The error due to particle size assumptions is relatively small when averaged over a range of scattering angles, but individual errors depend on the particular scattering angle, particle size and measurement vector definition. Differences due to radiative transfer modelling introduce differences between the retrieved products of less than 10 % on average, but can introduce vertical structure. The combination of the different scenario simulations and the application of both algorithms to both datasets enable the origin of some of the systematic features such as high-altitude differences when compared to SAGE II to be explained.

4.2 Introduction

Stratospheric aerosols play an import role in several atmospheric processes, including radiative forcing and ozone depletion. For decades, monitoring of stratospheric aerosols from satellite observations was largely the domain of occultation instruments such as Stratospheric Aerosol and Gas Experiment (SAGE) II. However, since the 2000s aerosol extinction has been retrieved from limb scatter instruments such as the Optical Spectrograph and InfraRed Imaging System (OSIRIS) (Llewellyn *et al.,* 2004; Bourassa *et al.,* 2012a, and references therein), the SCanning Imaging Absorption spectroMeter for Atmospheric CHartographY (SCIAMACHY) (Burrows *et al.,* 1995; Bovensmann *et al.,* 1999; von Savigny *et al.,* 2015, and references therein) and the Ozone Mapping and Profile Suite Limb Profiler (OMPS-LP) (Flynn *et al.,* 2006; Loughman *et al.,* 2018). While limb scatter provides greatly improved global coverage over occultation satellites, it requires additional assumptions and computationally expensive forward models to perform the inversions. Despite the difficulties, comparisons between limb scatter and occultation measurements generally agree favourably with

mean biases in the 10–15 % range during volcanically quiescent periods. While this is the average case, biases at certain latitudes and altitudes can be considerably larger. Additionally, biases after 2005 have not been well characterized due to the lack of baseline occultation measurements with which to compare.

This paper investigates the cause of the biases between the OSIRIS and SCIAMACHY aerosol extinction retrievals using comparisons with SAGE II and a series of simulation studies. The two limb-scattering instruments and the inversion techniques are described in Sect. 4.3. Also introduced here is the new version 1.4 SCIAMACHY aerosol extinction product used in this work. Initially, a triple comparison among OSIRIS, SCIAMACHY and SAGE II is performed in Sect. 4.4. As there was very little volcanic influence on the stratospheric aerosol load during the overlap period, this serves as a baseline for the agreement seen between the limb scatter and occultation aerosol records during volcanically quiescent times and motivates the investigation of error sources. Section 4.5 discusses the magnitudes of the errors that are expected from the assumptions in the OSIRIS and SCIAMACHY retrievals and radiative transfer models through a series of simulation studies. Section 4.6 applies the IUP and USask retrievals to both datasets to investigate differences due to the inversion techniques and radiance products. Lastly, conclusions and recommendations are discussed in Sect. 4.7

4.3 The aerosol retrievals

Generally, aerosol extinction retrievals for OSIRIS, SCIAMACHY and OMPS-LP limb-scattering instruments proceed in a similar fashion. First, radiance profiles at one or more wavelengths are used to construct a single measurement vector as a function of altitude. As this provides only one piece of information at each altitude, aerosol extinction is typically chosen as the retrieved quantity, although this is not the only possibility. However, extinction is the natural quantity retrieved from occultation instruments and allows for continuation of this historical record. Ideally, the measurement vector would be dependent only on the desired aerosol extinction parameter, but in practice it is also affected by the surface albedo, atmospheric density and aerosol optical properties including particle size, shape and

composition. Typically, an effective Lambertian surface reflectivity is retrieved concurrently with the aerosol extinction, while the atmospheric density and optical properties are assumed using external information. Although atmospheric density is provided at high resolution by ECMWF (European Centre for Medium-Range Weather Forecasts) or MERRA, data on aerosol optical properties are much sparser and a notable limitation in the current retrievals.

Although particle size information has been retrieved from limb instruments in the past with OMPS-LP and OSIRIS (Rault *et al.,* 2013; Rieger *et al.,* 2014) and more recently with SCIAMACHY (Malinina *et al.,* 2018), the standard operational products remain as extinction-only for the OSIRIS and OMPS-LP aerosol products. These extinction products have been used in numerous studies and continue to contribute to the stratospheric aerosol record (Kremser *et al.,* 2016; Thomason *et al.,* 2017), highlighting the importance of accurately characterizing not only precision but also biases in the current operational retrievals.

4.3.1 OSIRIS v5.07

OSIRIS was launched in 2001 aboard the Odin spacecraft (Llewellyn *et al.,* 2004). The spectrograph produces limb-scattered radiance profiles from 280 to 810 nm, with typical sampling every 2 km, a vertical resolution of 1 km and an altitude range from 7 to 75 km. Odin is in a near-terminator orbit with an equatorial crossing time of approximately 06:00 on the descending node, providing limb measurements with a limited range of viewing geometries. Typically, solar scattering angles vary between 60 and 120 with the largest values occurring in the tropics, and little correlation between the mean scattering angle and latitude. The OSIRIS measurements have been used in the inversions of multiple species with products now spanning over 15 years (McLinden *et al.,* 2012). The inversions use the SASKTRAN radiative transfer model (Bourassa *et al.,* 2008; Zawada *et al.,* 2015) and a multiplicative algebraic reconstruction technique (MART) to retrieve ozone, NO_2 and aerosol extinction at 750 nm. This paper uses the OSIRIS v5.07 aerosol data product retrieved with the algorithm discussed in Bourassa *et al.* (2007) and Bourassa *et al.* (2012a), which simplifies to the Chahine inversion technique (Chahine, 1970) for the choice of tangent altitude weighting factors in the aerosol-specific portion of the MART retrieval. This algorithm will be referred to as the USask retrieval in this paper. For the radiative transfer modelling, a unimodal

lognormal distribution is assumed with median radius, rg of 80 nm and distribution width, σ_g, of 1.6 as defined in Eq. (4.5). This distribution is consistent with mid-latitude optical particle counter (OPC) measurements during volcanically quiescent periods (Deshler *et al.,* 2003), although the variability in the OPC measurements is large, as discussed in Sect. 4.5.3. Mie theory is used to calculate the aerosol scattering properties with a refractive index from Palmer *et al.* (1975) assuming a 75 % concentration of H_2SO_4 and 25 % H_2O. This produces a refractive index of $1.427 + i7.167 \times 10^{-8}$ at 750 nm and $1.432 + i0.0$ at 470 nm. The USask measurement vector is defined as

$$y'_{jk} = \ln\left(\frac{I(\lambda_k, j)}{I(\lambda_{\text{ref}}, j)}\right) - \frac{1}{N}\sum_{j_{\text{ref}}=m}^{m+N-1} \ln\left(\frac{I(\lambda_k, j_{\text{ref}})}{I(\lambda_{\text{ref}}, j_{\text{ref}})}\right), \tag{4.1}$$

where the measurement vector, y'_{jk} at wavelength k and altitude j is the radiance, I, normalized by a reference altitude, j_{ref}, and shorter wavelength, λ_{ref}, that is generally less sensitive to aerosols. To reduce noise at the reference altitude N measurements are used, beginning at tangent height $j_{\text{ref}} = m$. To improve the convergence speed of the relaxation technique (Barcilon, 1975; Chu, 1985), a modelled measurement vector assuming a molecular atmosphere is also used as a normalization, yielding the measurement vector

$$y_{jk} = y'_{jk} - y^{\text{mol}}_{jk}, \tag{4.2}$$

where y^{mol} is computed using Eq. (4.1), with the modelled radiances assuming an aerosol-free atmosphere. As this acts as a constant offset, it does not affect the sensitivity of the measurement vector to aerosols. However, in addition to improving convergence, this normalization also helps to identify the region of interest for the aerosol retrieval; after normalization by the molecular signal, the dominant components remaining are aerosol at lower altitudes and stray light at higher altitudes. The reference altitudes are chosen as the point, or points, where the measurement vector is at a minimum within the measurement noise, i.e. where both the stray light and aerosol signals are smallest. This produces a normalization that varies scan to scan, but typically produces reference altitudes between 25 and 40 km with lower altitudes near the poles. For the USask retrieval, 750 nm is used as the long wavelength, λ_k, and 470 nm is used as the reference, λ_{ref}. Atmospheric data for pressure and temperature are interpolated to the OSIRIS scan location from the ECMWF operational analysis.

4.3.2 SCIAMACHY v1.4

SCIAMACHY (Burrows *et al.,* 1995; Bovensmann *et al.,* 1999) was a national contribution to the payload on ESA's Envisat Satellite, which was launched in March 2002. Envisat was placed in a sun-synchronous orbit at 800 km altitude with an equatorial crossing time of 10:00 on the descending node. In the limb mode the SCIAMACHY instrument scans across the flight direction with the total swath of 960 km and the centre of the scan displaced by a few degrees westwards from the flight direction. This results in solar scattering angles ranging from 30° in the high northern latitudes to 150° in the high southern latitudes with a strong latitudinal dependence. SCIAMACHY operation started in August 2002 and ended with a sudden loss of communication with the Envisat satellite in April 2012. SCIAMACHY performed measurements in eight spectral channels covering a wide spectral range from 214 to 2380 nm with a resolution varying from 0.2 to 1.5 nm. During its mission, SCIAMACHY measured the solar radiation in nadir, limb scatter and solar–lunar occultation geometries and provided daily measurements of the solar spectral irradiance that have been used to retrieve a variety of species including aerosols, clouds, ozone, BrO, NO_2 and water vapour. For this study stratospheric aerosol retrievals are performed using the data from the limb scatter viewing geometry, where measurements are provided every 3.3 km with a vertical resolution of 2.6 km in the altitude range from approximately 0 to 100 km.

The stratospheric aerosol extinction retrieval algorithm used in this study is an updated version of the algorithm described by von Savigny *et al.* (2015) and Ernst *et al.* (2012). The SCIAMACHY v1.4 retrievals, herein referred to as the IUP retrievals, use the newer version 8 SCIAMACHY Level 1 radiance data. Atmospheric pressure and temperature background profiles from ECMWF operational analysis data from the specific date, time and location of each SCIAMACHY limb measurement are used. In comparison to the previous version of the algorithm (von Savigny *et al.,* 2015; Ernst *et al.,* 2012) and the USask retrieval algorithm, the updated v1.4 algorithm drops the shorter, 470 nm wavelength normalization to reduce the uncertainties related to measurement noise and lower sensitivity to aerosols. The new measurement vector is given by

$$y_{jk} = \ln(I(\lambda_k, j)) - \ln(I(\lambda_k, j_{\mathrm{ref}})). \tag{4.3}$$

To reduce noise on the measurements, all measured wavelengths within ±2 nm of λ_k are used in the retrieval. For the v1.4 extinction product the aerosol profiles are retrieved at 750 nm. The retrieval uses measurements in the altitude range from around 12 to 35 km (depending on the latitude and season) with a reference tangent altitude of about 38 km. The v1.4 aerosol extinction retrieval is performed on the measurement altitude grid, and the values below and above the retrieval range are fixed to the a priori values. Effective Lambertian albedo of the underlying surface is concurrently retrieved based on the limb radiances near the reference tangent height to reduce the influence of clouds below the field of view, although clouds within the field of view remain an issue. To reduce their impact, extinction values greater than $0.001\,km^{-1}$ are considered cloud contaminated and filtered after the retrieval is performed. To solve the inverse problem an iterative regularized inversion approach similar to that described by Rodgers (2000) is used. As in Ernst *et al.* (2012) it is assumed that the errors are uncorrelated, and the noise covariance matrix is chosen to be diagonal. The signal-to-noise ratio is set to 200 for all tangent heights. For the a priori covariance matrix the non-diagonal elements drop off exponentially with a correlation radius of $3.3\,km$ and the diagonal elements correspond to a relative standard deviation (SD) of 1.

Forward modelling, as well as retrievals, is done using the radiative transfer model with the retrieval code SCIATRAN-3.7 (Rozanov *et al.,* 2014). The scattering phase functions are calculated using Mie scattering theory, assuming spherical sulfate aerosol particles with a unimodal, lognormal size distribution. The refractive indices are calculated using the OPAC database (Hess *et al.,* 1998). At 750 nm the real component of the index of refraction is 1.427, and the imaginary component is 7.170×10^{-8}. The stratospheric aerosol parameters are defined from 12 to 46 km, where it is assumed to consist of sulfuric droplets with 0 % relative humidity in the surrounding atmosphere. The previous version 1.1 algorithm (von Savigny *et al.,* 2015) used a lognormal particle size distribution with a median radius of 110 nm and width of 1.37, also consistent with in situ observations by Deshler *et al.* (2003). Although there is no evidence to prefer either the particle size distribution used in the USask retrieval or that used by von Savigny *et al.* (2015), using different distributions complicates the comparison of limb-scattering retrievals, and so it is beneficial to make a consistent choice for this work. Therefore, the version 1.4 SCIAMACHY product uses the same lognormal

assumption as the v5.07 OSIRIS product ($r_g = 80\,\text{nm}$, $\sigma_g = 1.6$). While a full validation of the version 1.4 is currently ongoing, initial comparisons with version 1.1 show smaller uncertainty of the individual retrievals, reduced profile oscillations and better parameterized upwelling radiation (resulting also in less sensitivity to underlying clouds) due to the retrieval of albedo.

4.4 Coincident comparisons with SAGE II

The SAGE II was launched in 1984 and operated until November 2005, providing one of the longest continuous records of stratospheric aerosols. As an occultation instrument, the SAGE II aerosol retrieval is insensitive to many of the assumptions required in the limb scatter retrievals, making for a robust, independent comparison. This work uses the version 7.00 SAGE II aerosol extinction data at 525 and 1020 nm (Damadeo *et al.,* 2013). Several improvements have been made since version 6.2 that have resulted in aerosol extinction decreasing more quickly at higher altitudes. As both the OSIRIS and SCIAMACHY aerosol products are produced at 750 nm, the SAGE II data are interpolated to this wavelength using the Ångström coefficient derived from the 525 and 1020 nm channels. Although this is not a perfect conversion, as the wavelength dependence is not strictly linear in log-wavelength log-extinction space, the error is generally limited to less than 10 % for most particle sizes (Rieger *et al.,* 2015). To test agreement between the three instruments a coincident comparison is performed when all instruments have collocated measurements. Measurements are used when OSIRIS and SCIAMACHY observations are within ±5° latitude, ±20° longitude and ±24 h of the SAGE II tangent point. As limb measurements have approximately 200 km path lengths through the atmosphere, and scanning of a vertical profile typically occurs over a few degrees latitude, tightening these criteria does not generally improve agreement. To minimize the impact of clouds in the analysis extinction, values greater than $0.0025\,km^{-1}$ have been excluded. Due to the relatively eruption-free period of this comparison, this has minimal effect on the comparisons removing approximately 3 % of scans above 15 km and none above 20 km. This criterion provides 2580 coincident measurements between 2002 and 2005, when all three instruments were operating. The comparison is broken into 20° latitude

bins to better distinguish biases related to latitude and solar geometry conditions. Results are shown in Fig. 4.1. In general, all instruments agree to within approximately 15 % for most regions. Exceptions to this are at high altitudes and latitudes (such as panels a, b and h) where both OSIRIS and SCIAMACHY retrieve lower values than SAGE II by up to 40 % at 30 km. At latitudes above 40° N SCIAMACHY shows systematically higher results than SAGE II for all altitudes below 30 km. This effect increases with latitude up to approximately 40 % at the highest northern latitudes and is visible in panels g and h of Fig. 4.1. Although the largest clouds have been removed, both limb scatter instruments are likely to still contain some cloud contamination near and below the tropopause and the differences compared to SAGE II show large SDs in these regions.

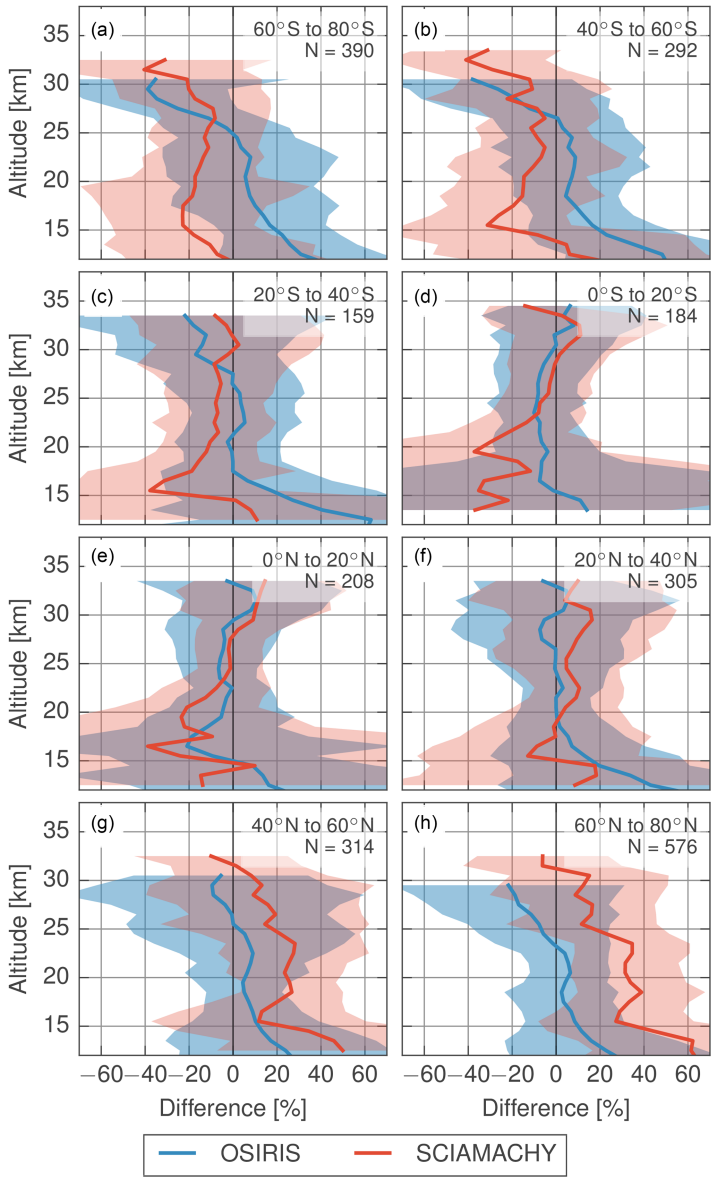

Figure 4.1: Coincident comparison between OSIRIS and SCIAMACHY measurements compared to SAGE II. Difference computed as (Instrument − SAGE II)/SAGE II × 100 %. Shaded regions indicated one SD of the differences from the median.

Several factors are expected to contribute to the differences between the aerosol extinction retrieved from the measurements of the occultation and limb scatter instruments, as well as the different biases between OSIRIS and SCIAMACHY. Limb scatter inversions use complex forward models which are not identical in their assumptions or approaches. The inversions

themselves also differ in several ways, with SCIAMACHY using a regularized inversion technique and OSIRIS using MART. A priori assumptions, such as the choice of aerosol particle size distributions and extinction profiles, also affect the retrievals. The importance of these effects depends on the viewing geometry of the instrument. OSIRIS and SCIAMACHY have significantly different viewing geometries as a result of the Envisat and Odin orbits. The following sections explore the significance of these different effects.

4.5 Simulation study

To test the sensitivity of the retrievals to assumed parameters and retrieval settings, a series of simulation studies is performed. The 2580 near-coincident scans from the SAGE II comparison are used as the test cases. These scans cover the full range of OSIRIS and SCIAMACHY geometries. While these scans are limited to pre-2006, the simulations use a range of atmospheric scenarios consistent with both background and volcanically perturbed conditions. Four factors are investigated in this study: the impact of different radiative transfer models, a priori extinction profile and particle size assumptions and choice of measurement vectors.

4.5.1 Radiative transfer modelling

It is difficult to decouple the retrieval algorithms from the radiative transfer models entirely due to differences in languages, input formats, and interfaces. However, differences between the IUP and USask retrievals due to the radiative transfer models can still be estimated by simulating measurements using one model and retrieving with the other. For this test, the SASKTRAN radiative transfer model is used to generate radiances that simulate the OSIRIS measurements. These synthetic radiances are then used in the IUP retrieval which uses the SCIATRAN radiative transfer model. The same is then performed with the SCIATRAN simulated radiances and the USask retrieval using SASKTRAN, again on OSIRIS measurements. Although this is not a test of "correctness" of either model, nor a test of how well the radiative transfer models could agree, it provides an indication of the magnitude of differences that should be expected due to the configuration of the radiative transfer models as used in the retrievals. Figure 4.2 shows the differences in the modelled radiances and

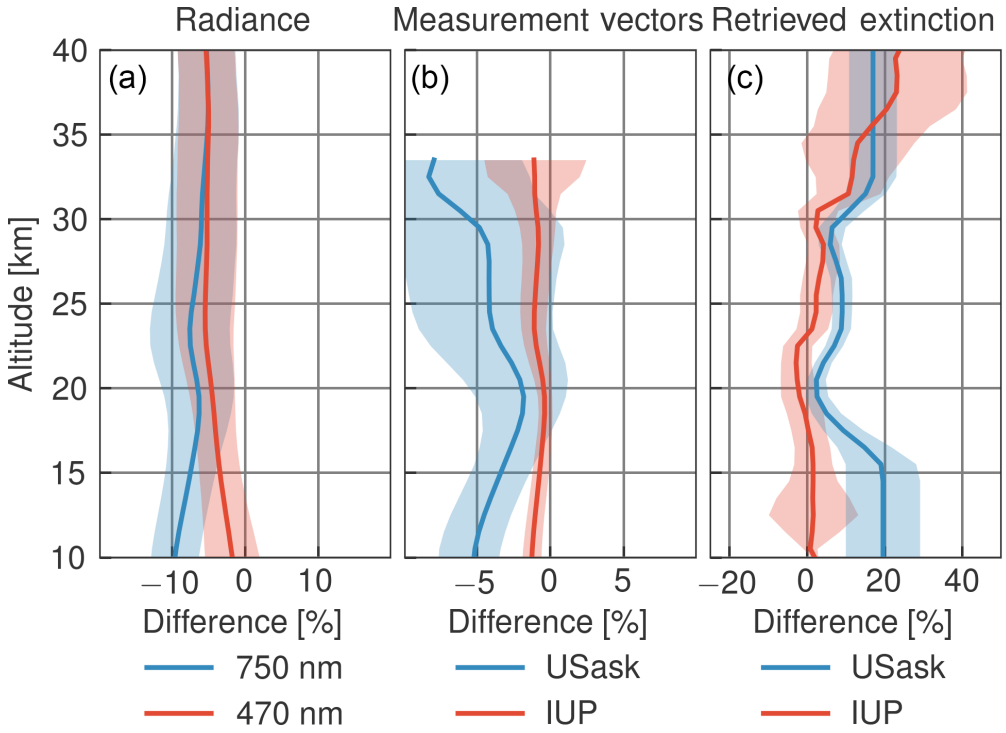

Figure 4.2: Comparisons of the radiative transfer models. Panel **(a)** shows the differences in radiance computed using SASKTRAN and SCIATRAN. Panel **(b)** shows the difference in measurement vectors. Panel **(c)** shows the difference in retrieved profiles. Differences in panels **(a)** and **(b)** are computed as (SASKTRAN − SCIATRAN)/(SASKTRAN + SCIATRAN) × 200 %. Extinction error is computed as (retrieved − true)/true × 100 %.

retrievals. Panel a shows the differences in the radiances at the 470 and 750 nm wavelengths. The radiances have systematic differences of approximately 5 %, with SCIATRAN producing larger radiance values than SASKTRAN. Some of this difference is due to model resolution settings. SASKTRAN simulations are performed at a higher vertical resolution of 1 km, and when both models use this higher-resolution vertical grid the agreement is improved to within 2–5 %. However, because the IUP retrieval is performed on a 3.3 km grid, the higher resolution is not required for SCIAMACHY retrievals. Although the variation in radiances between the models can occasionally reach 15 %, the normalizations used in the measurement vectors cancel much of the systematic differences. This can be seen in panel b, where differences in the measurement vectors, computed using the two different models, are shown. In this panel the red curve shows the percent difference between the IUP retrieval vectors defined in Eq. (4.3) when computed from SASKTRAN vs. SCIATRAN radiances. The blue

curve shows the same, except computed using the USask measurement vector definition from Eq. (4.1). The high-altitude normalization used in the IUP retrieval decreases the differences between the models to less than 2 % at most altitudes. If the short wavelength normalization is included the difference is larger, typically near 5 %, since the wavelength-dependent modelling differences vary more with altitude. How this difference translates to the retrieved extinction is shown in panel c. Here, the red curve shows the difference in the IUP retrieved extinction using SASKTRAN generated radiances compared to the true state. Similarly, the blue curve shows the same for USask retrieved extinction using SCIATRAN-generated radiances. The IUP retrieval produces errors in the retrieved extinction less than 5 % for most of the aerosol layer, with a SD close to 5 % as well. The larger differences in the USask measurement vector lead to larger differences in the USask the retrieved extinction, although errors are still typically less than 10 %. The exception to this is below 17 km and above 30 km, where the sensitivity to aerosol is low, and therefore small changes in the radiative transfer cause large changes in the extinction. This highlights that the high-altitude normalization is effective not only in minimizing errors due to uncertainties in unknown physical quantities such as albedo but also in reducing errors due to model assumptions. Conversely, the short wavelength normalization has the potential to introduce additional error if the radiative transfer model biases change with wavelength.

4.5.2 A priori profiles

The effect of the a priori profile on the retrieval is an important consideration and one that has the potential to vary substantially between retrieval methods. Although the MART relaxation used in the USask retrieval has no regularization, and the IUP retrieval is only weakly constrained by the a priori profile, the effect of the a priori profile at altitudes above the retrieval range can still play an important role. The aerosol here can couple to the lower altitudes due to the high-altitude normalization of the measurement vectors. While this normalization has many benefits, it has the drawback of coupling the error at high altitudes to all altitudes below. The USask retrieval scales the a priori profile above the retrieval range, at each iteration of the retrieval to match the top retrieved value and thus avoid sharp discontinuities in the retrieved profile. Therefore, the absolute error above the retrieval range

depends on the shape of the a priori profile at and above the normalization and the retrieved aerosol just below the normalization. Conversely, the IUP extinction is fixed to the a priori value above the retrieval altitudes and so will depend less on the shape of the chosen a priori profile and more on the absolute value in the normalization range.

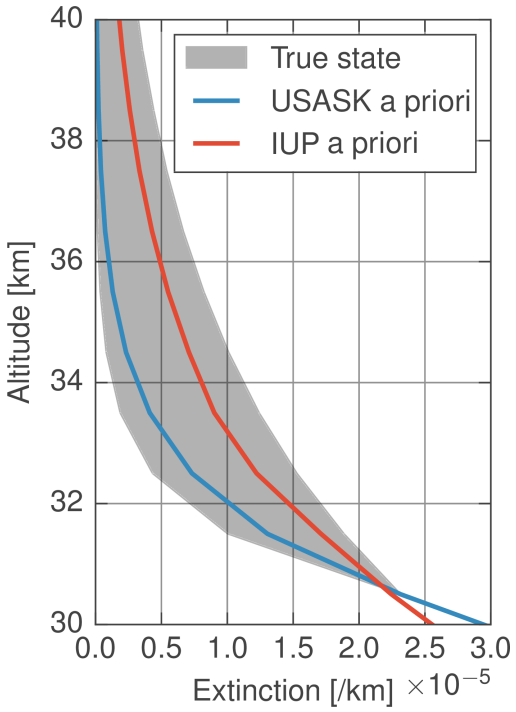

Figure 4.3: The range of the true state aerosol profiles is shown as the shaded region. The USask a priori profile is shown in blue and the IUP in red.

The effect of the a priori profile above the retrieval range is tested through a simulation study where the true high-altitude aerosol profile (i.e. the input profile used to generate the synthetic measurements) differs from that assumed in the retrievals. For this test an exponentially varying aerosol profile above 30 km is taken to be the truth. The slope of the exponential profile is then varied for each simulated OSIRIS and SCIAMACHY scan. The range of exponential profiles used as true states in the simulations is shown as the grey shaded region in Fig. 4.3. The USask and IUP a priori values are shown as the blue and red lines respectively. The shape of the a priori profile below 30 km, as well as all other aerosol parameters such as particle size, is assumed correctly in the simulated retrievals to avoid introducing errors due to other retrieval parameters. The simulated data were then used to retrieve the extinction profile using the USask and IUP retrievals under two conditions.

First, both retrievals are initialized with the USask a priori profile and, second, both are initialized with the IUP a priori profile.

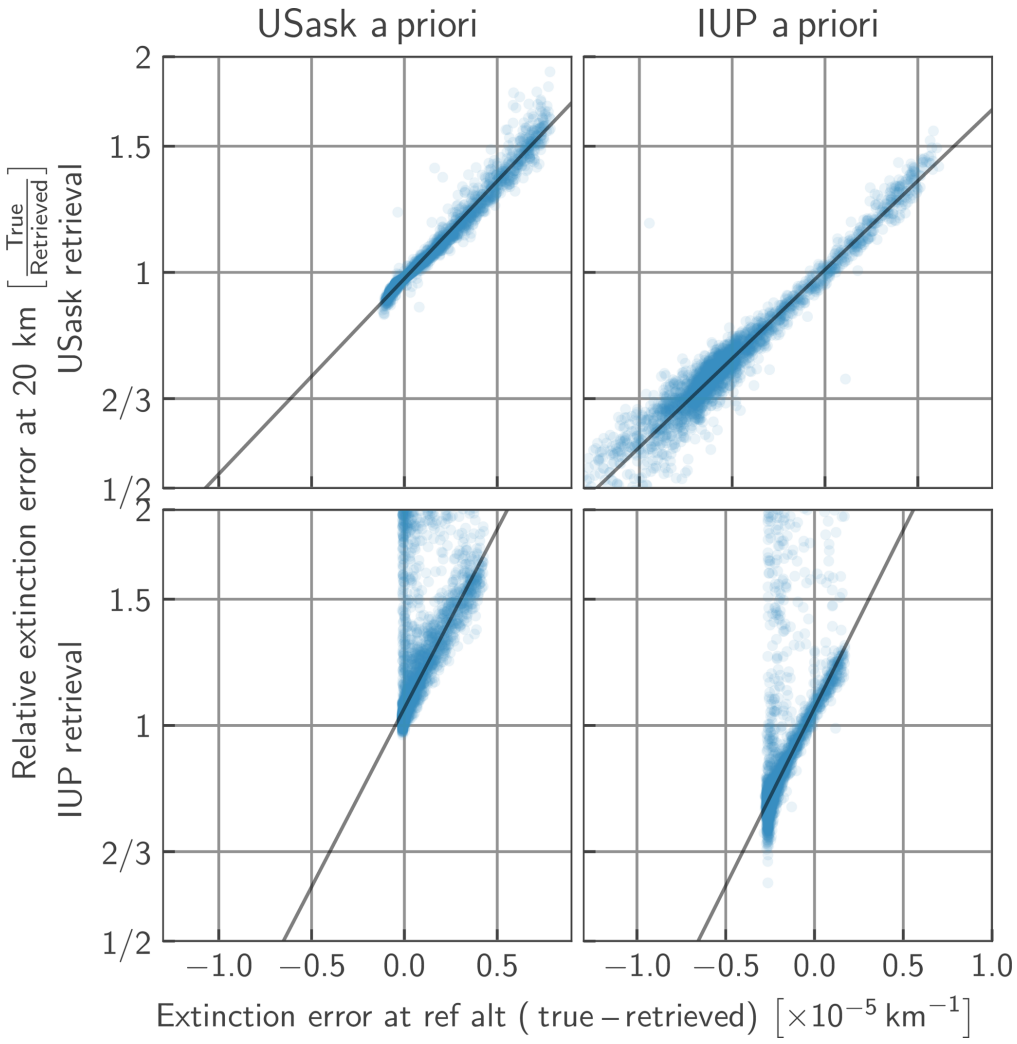

Figure 4.4: Relative error in the OSIRIS data retrievals at 20 km as a function of the absolute error in the true extinction at the reference point. The solid lines show the least squares fit to the data.

Figure 4.4 shows the relationship between errors at the reference altitude to errors lower in the profile for four cases. The top row shows results for the USask retrieval with the bottom row showing the IUP retrievals. The left column shows results when the USask a priori profile is used for the retrievals, with the right column showing results when the larger IUP a priori values are used. The solid line shows a linear best fit to the data. Generally, if aerosol is overestimated in the normalization range, due to an a priori profile that decays too slowly with altitude, the aerosol is overestimated for the entire retrieval. This is because the modelled

vector is normalized by an overly large value, decreasing the magnitude in the retrieval range; as a result, extra aerosol is added to compensate. The error in the retrieved aerosol is very well correlated with the error in the normalization range, with little dependence on whether the USask or IUP retrieval is used. This holds well for all geometries tested and for both retrieval algorithms. However, higher altitudes are more sensitive to aerosol loading, and so show a larger error in the retrieved profile for a similar absolute error in the a priori profile as the normalization altitude is increased. This can be seen in the larger sensitivity to a priori profile errors in the IUP retrieval, which uses a 38 km reference height, as opposed to the USask retrieval that used 35 km. The same error of $10^{-6}\,km^{-1}$ at a normalization altitude of 38 km will cause approximately twice the error that it does at 35 km. At low altitudes, less than approximately 14 km, the sensitivity to aerosol is very low and the retrievals no longer show a clear relationship between the retrieval error and the a priori profile error.

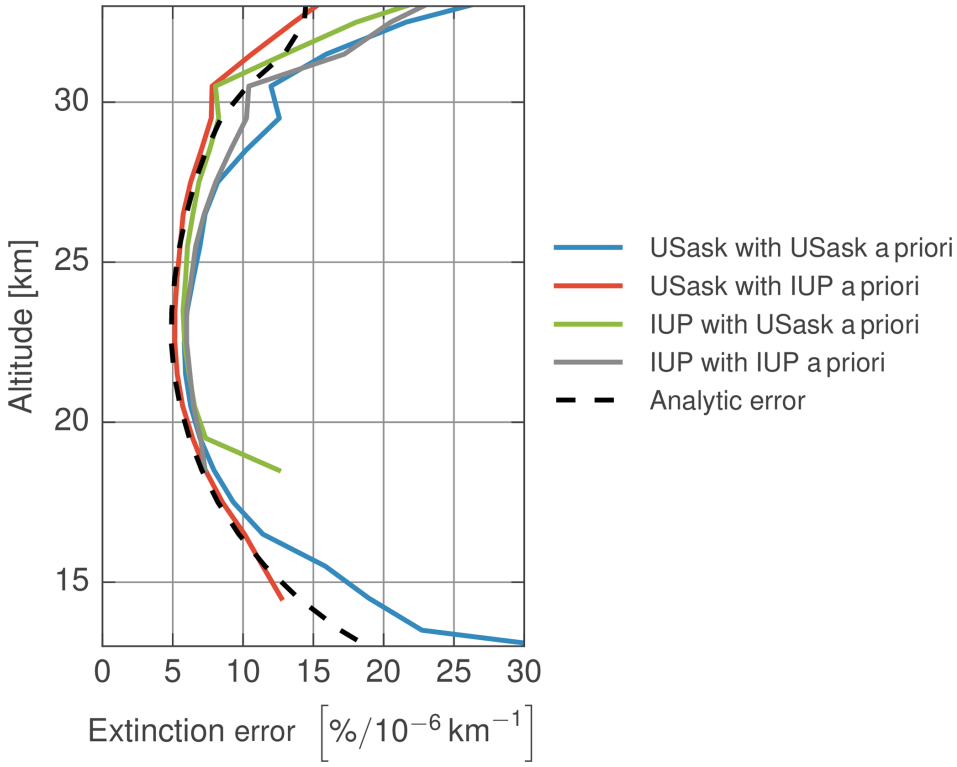

Figure 4.5: Percent error in the OSIRIS data retrievals as a function of altitude relative to an extinction error of $10^{-6}\,km^{-1}$ at 35 km. Solid lines show values computed from the best fit line from the simulation studies shown in Fig. 4.4. Dashed line shows the error expected from the linear error analysis of Eq. (4.4).

The altitude dependence of the retrieved error, normalized by the error at 35 km is shown

in Fig. 4.5. We note that normalizing the IUP retrieval by the error at 35 km is not strictly correct as the reference altitude is at 38 km. However, this allows for a consistent comparison between the two algorithms, and due to the relatively linear nature of the error it is not expected to introduce large biases. The retrieval error is smallest at around 22 km, where the aerosol loading is highest, and the measurement sensitivity is still quite good, with error increasing above and below this altitude. The error can also be estimated without simulating the full retrieval using the equation

$$\delta\mathbf{k} = \mathbf{G}\delta\mathbf{y}, \tag{4.4}$$

where $\delta\mathbf{k}$ is the error in the retrieved extinction, $\mathbf{G}$ is the gain matrix or the sensitivity of the retrieved extinction to variations in y, and $\delta\mathbf{y}$ is the error in the measurement vector. In this case, $\delta\mathbf{y}$ is the error in the measurement vector due to errors in the assumed aerosol at the normalization altitude and above. As the retrieval error is quite linear with respect to errors in the high-altitude profile, $\delta\mathbf{y}$ in the retrieval range can be calculated directly from the Jacobian matrix, $\mathbf{K}$. This analysis as applied to the USask retrieval is plotted in Fig. 4.5 as the dashed line. Agreement between the analytic method and simulation study is excellent over the full range of values tested. As $\mathbf{G}$ and $\mathbf{K}$ are typically readily available from the inversion method, this can also be applied on an operational basis if estimates of the extinction error at the normalization point are known.

4.5.3 Particle size

In the standard extinction retrievals the aerosol optical properties are not retrieved and must therefore be assumed when retrieving extinction. Of primary importance in the IUP, USask and OMPS retrievals is the assumption of a fixed particle size. All three retrievals assume lognormal distributions that correspond to typical background conditions as measured by Deshler *et al.* (2003), albeit with somewhat different lognormal parameters. The lognormal distribution used in the retrievals is given by the equation

$$n(r) = \frac{N}{\sqrt{2\pi}\ln(\sigma_g)r}\exp\left(-\frac{(\ln(r_g)-\ln(r))^2}{2\ln^2(\sigma_g)}\right), \tag{4.5}$$

where r_g is the median radius, σ_g the distribution width and N the number density. During background conditions the median radius is generally larger than 40 nm but less than 200 nm,

depending on altitude. However, after volcanic eruptions, a second mode of particles with median radii up to a few microns may be present, further complicating the analysis. The effect of this constant unimodal particle size assumption was estimated to a degree by Rieger *et al.* (2015), but a limited number of geometries and cases were tested. More recently, Loughman *et al.* (2018) estimated the impact of particle size assumptions based on estimates of the phase function, but they did not fully propagate the error through the retrievals. This work extends these previous analyses to additional conditions and geometries and estimates the impact on the retrieved extinction.

To estimate errors due to particle size assumptions two sets of simulations are performed. First, a study to estimate errors in the retrieved extinctions during relatively quiescent periods is done, when only a fine mode of aerosols is present. For these simulations, the fine-mode lognormal parameter profiles as measured by the OPC in Wyoming by Deshler *et al.* (2003) between 2001 and 2014 are used as inputs for the simulated data. This provides 44 unique particle size profiles. To avoid noise and high-frequency oscillations the OPC profiles are smoothed to a vertical resolution of approximately 3 km. The extinction profile was set to twice that of the a priori profile, with no change in the shape to avoid including errors from the a priori profile in this portion of the study. The second set of simulations covers conditions more representative of those after volcanic eruptions, when an additional mode of larger particles is present. For this case, the smoothed coarse mode as measured by the OPC is also added to the true extinction profile. The number densities of the fine and coarse modes are set such that the coarse mode accounts for 70 % of the total extinction. In each case, the coincident OSIRIS and SCIAMACHY scans were simulated using a random OPC particle size profile and a random albedo between zero and one as the true state. Figure 4.6 shows the range of median radii, widths and Ångström exponents (calculated between 525 and 750 nm) used in the simulations, as well as the a priori values.

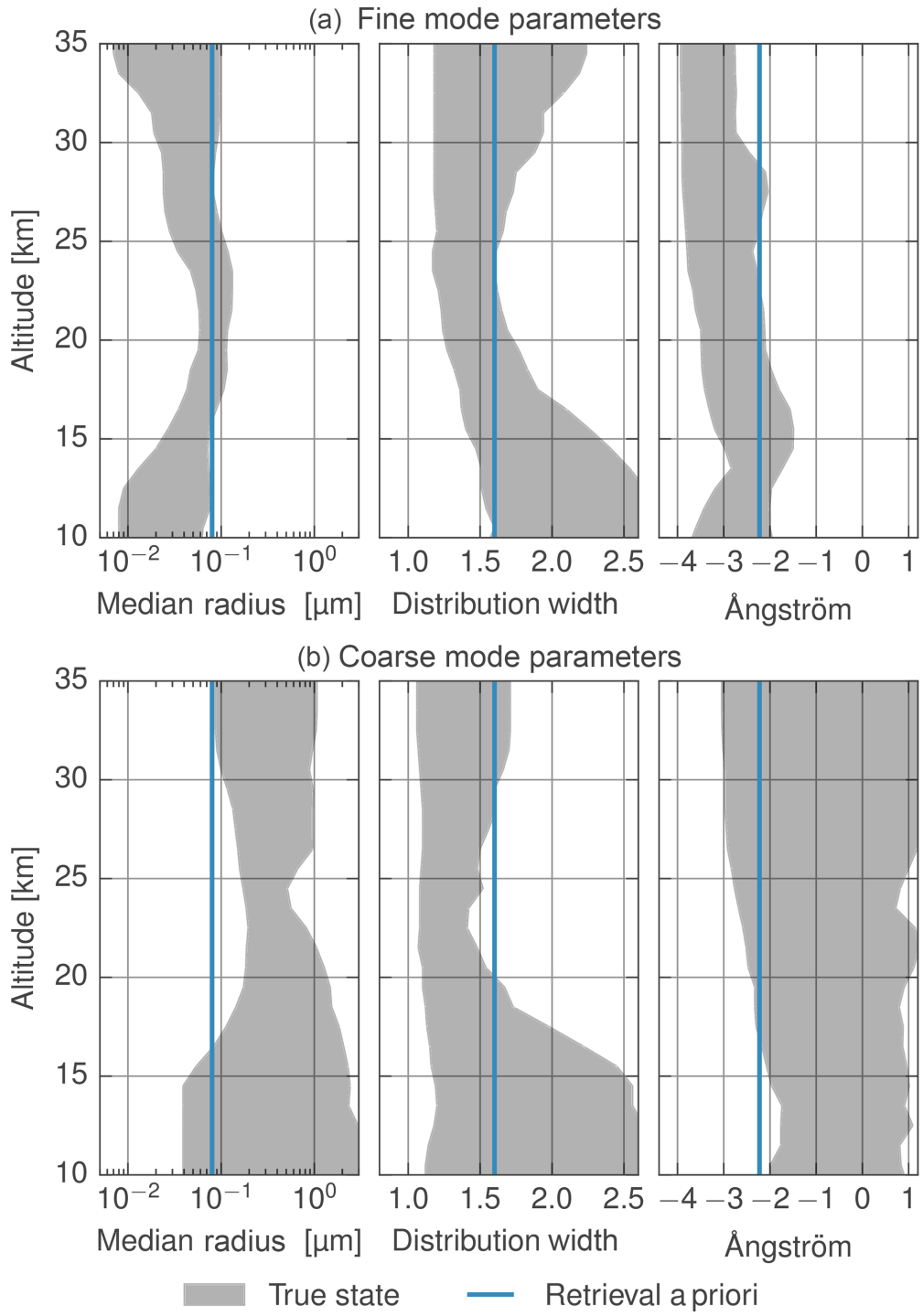

Figure 4.6: The range of particle sizes tested as a function of altitude. Panel **(a)** shows the fine-mode parameters and panel **(b)** the coarse mode. The blue lines show the USask and IUP a priori values assumed in the retrievals. The grey shaded region shows the range of values used in the simulations.

The standard USask algorithm was then used to retrieve extinction with the simulated data. These retrievals were also repeated using the USask algorithm but without the short wavelength normalization to determine its effect. The top row of Fig. 4.7 shows the relative error in the retrieved extinction for the standard USask retrieval when only a fine mode of particles is present, grouped by scattering angle. The colour of the line indicates the Ångström coefficient. Only the SCIAMACHY geometries are shown here, as the OSIRIS results are very similar, but with a reduced range of scattering angles. Generally, errors are largest in the strongly forward and backscattering cases, with a strong dependence on the Ångström coefficient. The assumed size distribution has an Ångström coefficient of 2.3, and consequently when the true state is near this value the retrieval has little error. At altitudes above 25 km, however, this assumption is consistently too high and leads to large errors, particularly in strongly forward scattering conditions.

The second row of Fig. 4.7 shows the same, but when the retrieval does not use a short wavelength normalization. In this case, the error is reduced in forward scattering conditions but increased in backscatter, particularly at lower altitudes, where sensitivity to aerosol is poor. The third row shows retrievals when the true state includes a second coarse mode of particles. In this case the assumption of an Ångström coefficient of 2.3 is generally more accurate at higher altitudes, and so the error above 20 km is reduced compared to the fine-mode-only case. However, the dependence on Ångström coefficient is weaker for the bimodal distributions, with many different particle sizes producing comparable errors. The effect of normalization is also not as clear under these more volcanic conditions, with only strongly forward scattering geometries showing a clear preference for no wavelength normalization.

This dependence on Ångström coefficient and scattering can be seen more clearly in Fig. 4.8, which shows a cross section of the results in Fig. 4.7 at 20 km, as well as the results from OSIRIS geometries. Each panel shows the relative error in the retrieved extinction as a function of the true Ångström coefficient at 20 km. The colour of each point indicates the scattering angle of the measurement. Panels a and b show results for the fine-mode-only simulations, while c and d show results from bimodal cases. Panels a and c shows results from OSIRIS geometries, and those from SCIAMACHY geometries are presented in panels b and d. The retrievals without the short wavelength normalization are shown in the right four

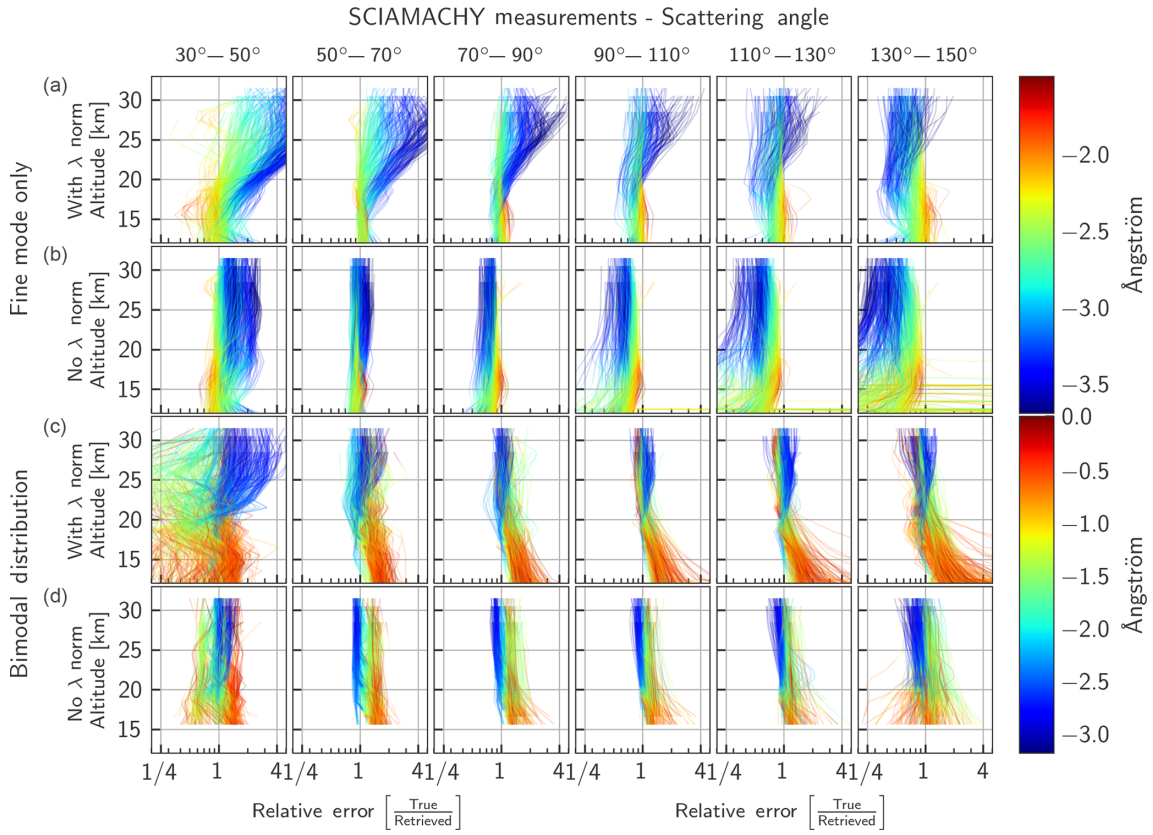

Figure 4.7: Error in the retrieved USask extinction for the simulated SCIAMACHY measurements grouped by the scattering angle for four different cases. The top two rows show results when only a fine mode of aerosols are present; the bottom two rows have both a fine and coarse mode. In both cases retrievals are done with a short wavelength normalization (**a** and **c**) and without (**b** and **d**). The colour of the lines indicates the Ångström coefficient.

panels. If only fine-mode particles are included in the simulated atmosphere, the error in the retrieval can be well parameterized by the Ångström coefficient and the solar scattering angle of the measurement. When the Ångström coefficient is assumed correctly the error in the retrieval is less than 10 %, nearly independent of the particular lognormal parameters. As the error in the Ångström coefficient increases, so does the error in the retrieval, up to 100 % for OSIRIS geometries. For SCIAMACHY geometries the range of scattering angles and errors can be larger due to larger variations in the aerosol phase function at extremely large and small angles. With a short wavelength normalization the retrievals show errors that are mostly symmetric around zero. While this will help to reduce biases over longer periods of time when a large range of scattering angles are sampled, seasonal biases are still

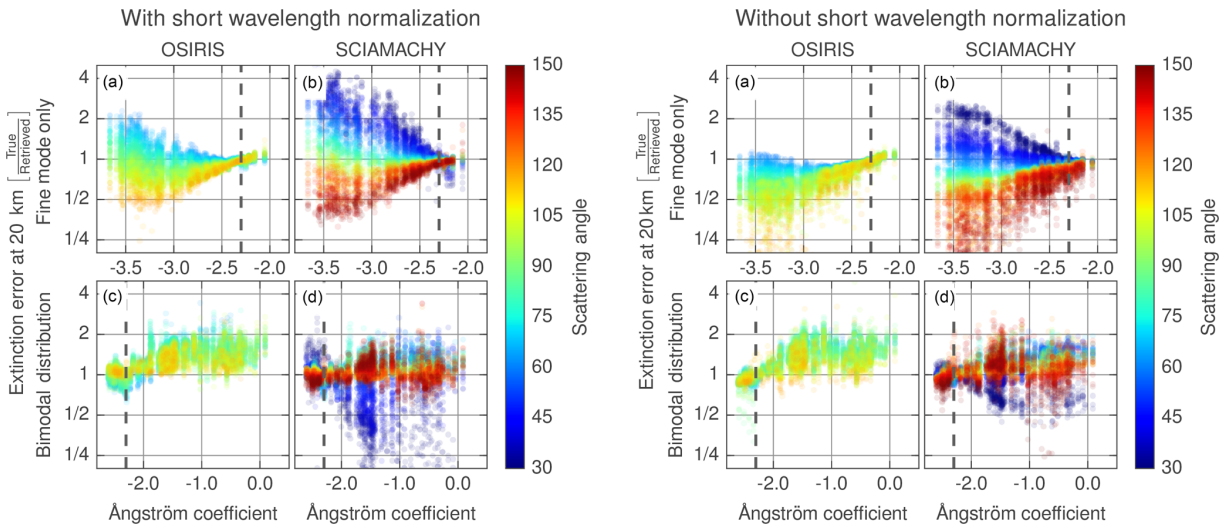

Figure 4.8: Error in the retrieved USask extinction as a function of Ångström coefficient at 20 km. The colour of the points shows the solar scattering angle. The top row shows the error for conditions when only a fine mode of aerosol is present. The bottom row shows the error when there is both a fine- and coarse-mode distribution. The black dashed line indicates the Ångström coefficient corresponding to the particle size distribution used in the retrievals.

to be expected as different scattering angles are sampled over the course of a year. Similarly, latitudinal biases are likely in the SCIAMACHY data as scattering angle depends strongly on latitude. Without a short wavelength normalization the general spread and shape of the errors is similar; however, the errors are not centred around zero with aerosol being overestimated more often than not. In this case, the error is minimized during forward scattering conditions when scattering angles are near 60°. When short wavelength normalization is used the error is at a minimum near 90°; subsequently the error for forward scatting geometries is increased, while it is decreased for backscattering geometries.

When coarse-mode particles are included, the phase functions can vary more widely for a given Ångström coefficient, leading to less of a clear relationship in the retrieved error. This can be seen in panels c and d of Fig. 4.8, where much weaker correlation between the Ångström coefficient, solar scattering angle and extinction error is visible. Even when the Ångström coefficient is assumed correctly, differences in the lognormal parameters can induce errors of 30 % in the retrieval for OSIRIS geometries and 50 % for SCIAMACHY geometries. While the error is less correlated, errors are not systematically larger than during volcanically quiescent periods, but do have a tendency to introduce low biases in the retrieved

results for most geometries and particle sizes. Additionally, while backscatter can still have large biases, they are not as large at the extreme scattering angles as during fine-mode-only conditions. During bimodal conditions the error in both the normalized and non-normalized retrievals is comparable, except during strongly forward scattering conditions when the short wavelength normalization increases the error. In general, this shows that the short wavelength normalization is beneficial during background periods under backscattering conditions, but generally increases the error during forward scatter. Additionally, in forward scatter both the 470 and 750 nm wavelengths are positively sensitive to aerosol, so the wavelength ratio will tend to decrease the sensitivity to aerosol and decrease the retrieved precision due to measurement noise as well.

4.6 Retrieval study

In Sect. 4.5 the sensitivity to retrieval assumptions and radiative transfer modelling was estimated. In this section, we explore the applicability of the USask retrieval to the SCIAMACHY measurements and vice versa, both to confirm the simulation studies and to better understand the sensitivity of the retrievals to differences in the radiance products. The same set of coincident SAGE II scans is used for this study, with comparisons performed in the same way as those presented in Sect. 4.4.

Figure 4.9 shows the USask retrieval applied to both instruments. Retrievals using the SCIAMACHY measurements agree very well with those using OSIRIS and show many of the same biases with respect to SAGE II. Both instruments show underestimation with respect to SAGE II at high altitudes and latitudes. If this was due to inaccuracies in the assumed particle size the error would be expected to change signs between hemispheres as the SCIAMACHY solar scattering angle goes from backscattering to forward scattering, which is not the case. Instead, these high-altitude errors are more likely to be caused by errors in the assumed a priori extinction profile at high altitudes where the measurements are normalized, as the effect of this is nearly independent of solar geometry. From Fig. 4.5 errors of $3 \times 10^{-6}\, km^{-1}$ in the reference altitude range could explain biases of $-30\,\%$ at high altitudes. Additionally, both instruments have some stray light at these higher altitudes that

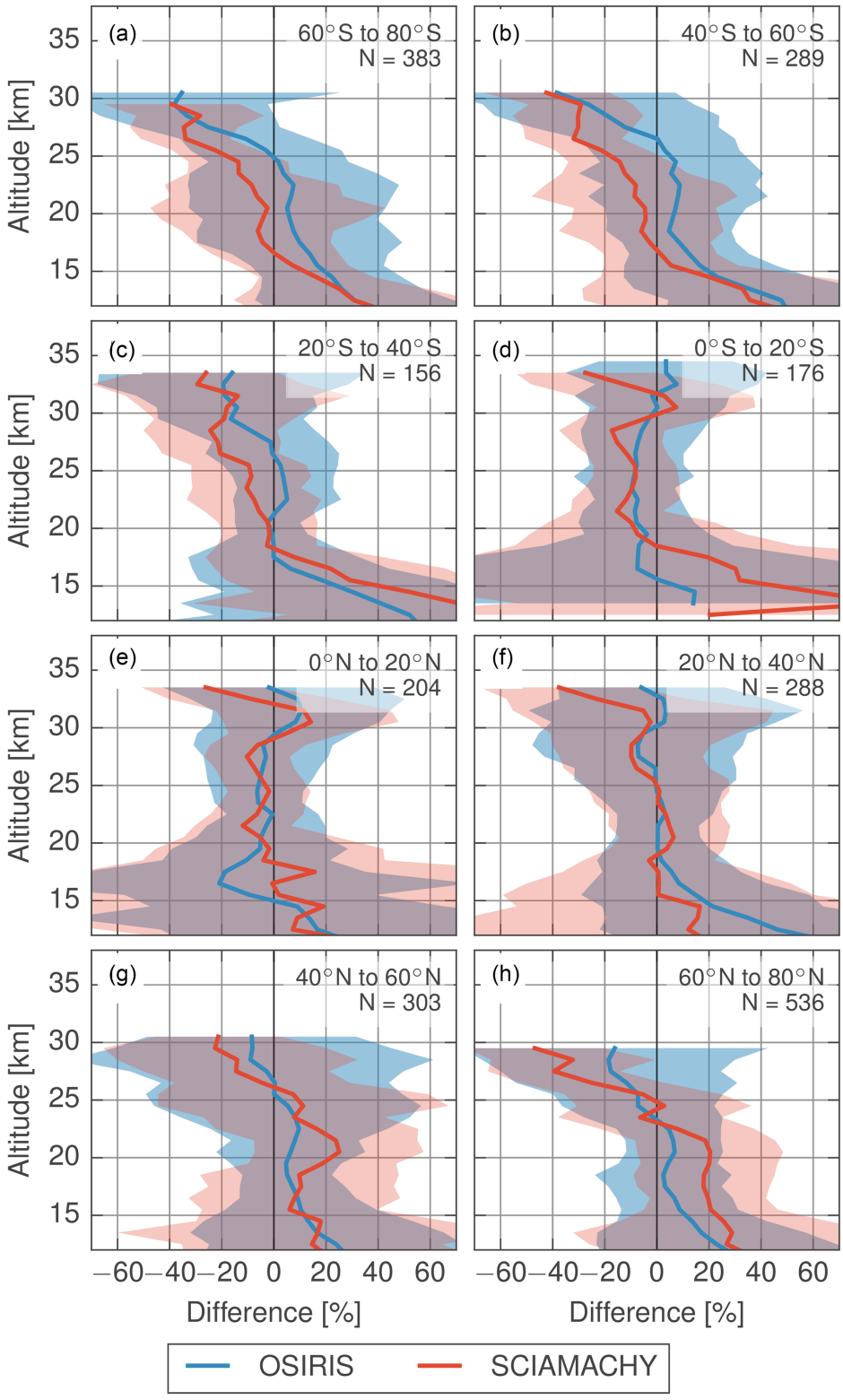

Figure 4.9: Coincident comparison with SAGE II when both OSIRIS and SCIAMACHY measurements have been processed with the USask algorithm.

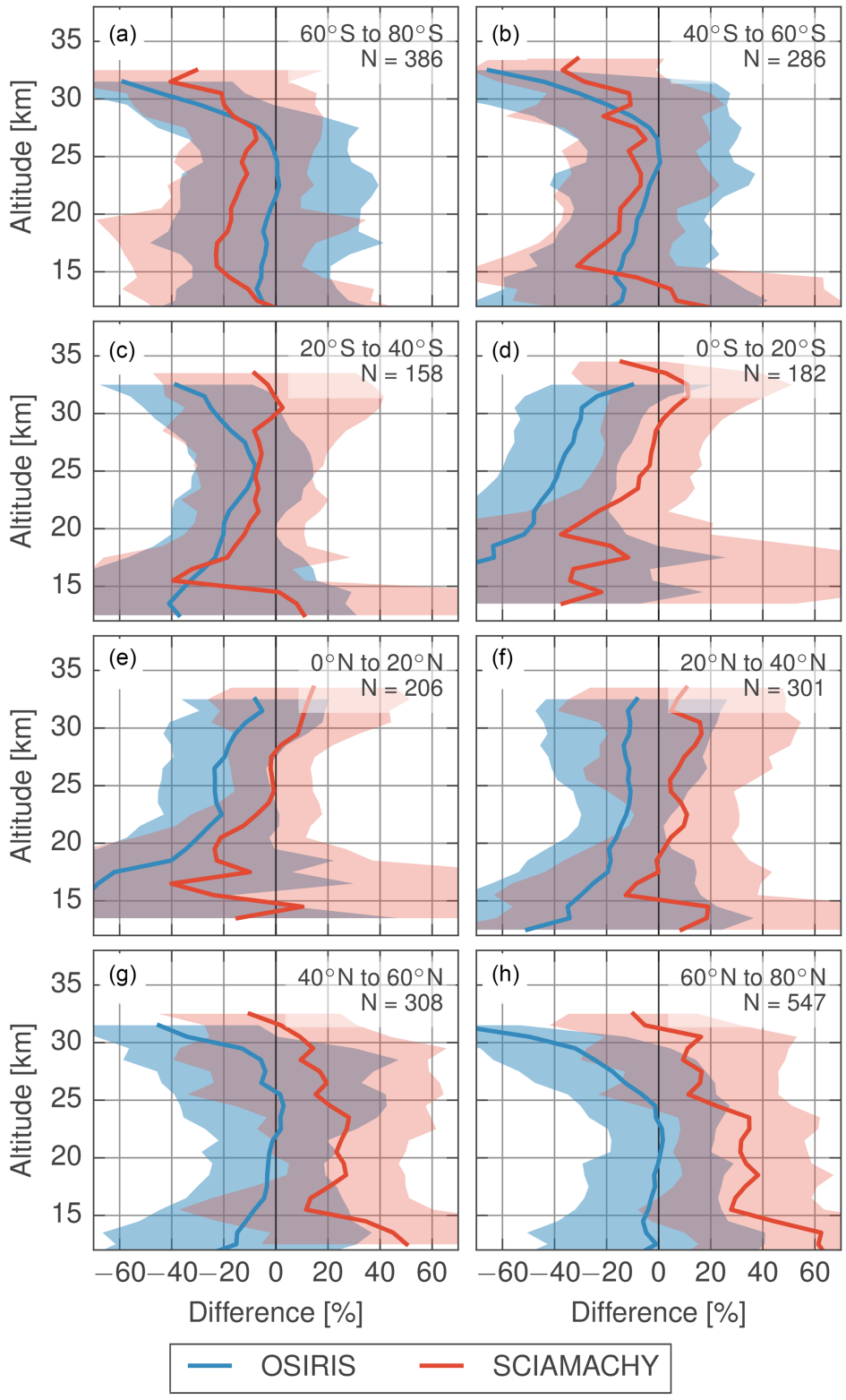

Figure 4.10: Coincident comparison with SAGE II when both OSIRIS and SCIAMACHY measurements have been processed with the IUP algorithm.

increases the radiance signal. This changes the shape of the aerosol measurement vector and is likely a contributing factor to the low biases at high altitudes and latitudes. Unfortunately, both a priori profile and stray light errors have similar systematic biases on the profile making them difficult to separate except in simulation, and errors in the a priori profile can either help to cancel or exacerbate errors due to stray light. The shift in the SCIAMACHY measurements from low biases in the Southern Hemisphere to high biases in the Northern Hemisphere is present, as was seen in the IUP retrieval in Fig. 4.1, again suggesting a particle size error. In the USask retrieval this shift is approximately 20–30 % between hemispheres, which from Fig. 4.8 would be consistent with an overestimation of the Ångström coefficient by approximately 0.3, i.e. an assumption that particles are too large at the high latitudes.

The IUP retrieval applied to both the SCIAMACHY and OSIRIS data is shown in Fig. 4.10. OSIRIS solar scattering angles do not vary as strongly between the northern and southern hemispheres, and so the OSIRIS retrievals do not exhibit the same shift from low biases in the south to high biases in the north that are seen in the SCIAMACHY measurements. The impact of the a priori profile choice can also be seen here. For the OSIRIS retrievals the USask a priori profile was used without scaling, resulting in low aerosol values in the normalization range and leading to lower aerosol values at all altitudes. However, if the IUP a priori profile is used the retrievals are substantially higher when compared to SAGE II (not shown). This is consistent with the results from Sect. 4.5.2, in that larger a priori values in the normalization range lead to larger values at all altitudes.

This highlights the sensitivity to the chosen a priori profile and reference altitudes and the limitations of both the USask and IUP approaches. The USask technique of scaling an a priori profile that decays rapidly with altitude works with both instruments provided the normalization altitude is chosen to minimize stray light. The variable normalization altitude ensures there is sufficient aerosol signal to determine the scaling, while the quickly decaying profile ensures the measurement vector is only weakly dependent on the scaling applied. However, while this provides a relatively robust retrieval it is likely to cause the aerosol to be underestimated at the normalization point, leading to low biases in the retrieved extinction, particularly at high altitudes. Conversely, the larger fixed a priori values used in the IUP retrieval works well for SCIAMACHY when an appropriate reference altitude

is chosen and can reduce biases at high altitudes. However, it yields poor results when applied to the OSIRIS measurements, illustrating the necessity of properly matching the normalization altitudes with the stray light characteristics and choice of a priori profile when using a fixed a priori profile. Together, the stray light, choice of normalization altitudes and a priori profile in the normalization range have a complex interplay. This can be seen panels a, b, g and h, where the OSIRIS biases at low altitudes are reduced compared to the USask retrieval (Fig. 4.9), despite not improving the retrievals at high altitudes. Conversely, the biases are increased elsewhere (panels c–f). Unfortunately, without more detailed knowledge of the stray light and error in the extinction in the normalization altitudes, the relative contribution of each cannot be determined.

4.7 Conclusions

The updated SCIAMACHY v1.4 aerosol extinction product shows good agreement with coincident SAGE II measurements, typically within 20 % for most regions. Exceptions to this include high northern latitudes where larger positive biases of 20–40 % are present and altitudes above 25 km in the southern high latitudes where negative biases are present. The differences between the limb and occultation measurements are well explained by two primary causes. First, the choice of a priori profiles is important in the limb retrieval due to the high-altitude normalization. If the shape of the a priori profile is assumed incorrectly in the USask retrieval the scaling applied to the profile in the retrievals will produce incorrect aerosol in the reference altitude, resulting in biases at all altitudes. The IUP retrieval fixes the aerosol profile above the retrieval range to the a priori value and errors couple similarly to lower altitudes. For both retrievals extinction errors in the reference altitude of $10^{-6}\,km^{-1}$ lead to errors in the retrieved extinction of 5 % near the aerosol peak and up to 20 % just below the reference altitude. Second, incorrect particle size generally shows a small mean difference when averaged over a range of scattering angles, but can have large differences of 100 % or more for individual cases, particularly for strongly forward and backscattering viewing conditions. This is especially important for orbits that systematically sample solar scattering conditions as a function of latitude. Simulations including a coarse mode of particles suggest

a low bias in the retrieved extinctions during volcanically perturbed periods is likely for most geometries. However, the magnitude of the error is not expected to be systematically larger than the during background conditions on a profile-by-profile basis. Additionally, while the USask and IUP retrievals use the same particle size assumptions, the biases are different for both the instruments and retrieval algorithms due to the difference in viewing geometries and definition of the measurement vectors. The error due to particle size can be reduced in backscatter geometries through the short wavelength normalization. However, this normalization has the opposite effect in strongly forward scattering conditions, where it makes the retrievals more sensitive to particle size assumptions and measurement noise. Differences in SASKTRAN and SCIATRAN radiative transfer models can cause systematic differences of up to 10 % between the retrieved products and may explain some of the vertical structure in the comparisons, but they are not expected to be a primary driver of the differences.

Future retrievals would benefit from improved estimates of the a priori aerosol extinction above 30 km and particle size distributions. In particular, OSIRIS retrievals could benefit from larger assumed a priori values at higher latitudes to reduce low biases compared to SAGE II. SCIAMACHY retrievals would benefit most from improved particle size estimates to reduce north–south biases. However, if this information remains limited, careful use of wavelength normalization (and the lack thereof) for specific viewing geometries has the potential to reduce retrieval biases. Additionally, although the USask and IUP approaches to aerosol in the normalization range of the measurements are different (scaling vs. fixed to a priori values respectively), both show comparable errors in the retrieved product for a given error in the normalization range. Robust measurements of high-altitude aerosol are therefore needed to establish whether a fixed a priori profile or a scaled one leads to less error at these altitudes. In summary, this study investigates the retrieval of extinction from the limb viewing observations of scattered solar radiance by the satellite borne instruments OSIRIS and SCIAMACHY. It provides a detailed analysis of our understanding of the systematic errors associated with these data products and biases with respect to the SAGE II measurements of extinction.

Chapter 5

A multi-wavelength retrieval approach for improved OSIRIS aerosol extinction retrievals

[1]Rieger, L. A., [1]D. J. Zawada, [1]A. E. Bourassa, and [1]D. A. Degenstein (2018), A multi-wavelength retrieval approach for improved OSIRIS aerosol extinction retrievals, J. Geophys. Res. Atmos., under revision, doi: 10.1002/2018JD029897.

[1]Institute of Space and Atmospheric Studies, University of Saskatchewan, Saskatoon, Canada

The study presented in the previous chapter indicated that limb scattering measurements are sensitive to the a priori profile at the reference altitude as well as the assumed particle size distribution used in the retrieval. Although high altitude biases can be large, errors here contribute to a relatively small fraction of the aerosol budget, so are less important for large-scale climate effects. Ridley *et al.* (2014) and Andersson *et al.* (2015) noted that smaller volcanic eruptions, particularly those at higher latitudes have a disproportionately large effect in the upper-troposphere and lower-stratosphere, a region where limb scattering measurements have been highly error prone due to poor aerosol sensitivity and cloud contamination. Crucially, it was found that the particle size biases were dependent on what measurement vector was used, with wavelength normalization playing a complex geometry dependent role. This opens the possibility of optimizing the measurement vector to reduce particle size biases as well as improving measurements in the UTLS region.

The final component of this work is to improve the OSIRIS aerosol data product by

developing a new algorithm using information gained from the simulations and comparisons with SCIAMACHY. In the previous work it was found that below approximately 15 km, particularly in backscattering conditions, the use of a short-wavelength normalization could improve the sensitivity to aerosol and decrease the dependence on the assumed particle size. However, this could be detrimental at other geometries and altitudes. This paper develops a retrieval technique that uses a variable wavelength normalization to improve the retrieval sensitivity over a wide range of conditions while reducing biases related to viewing geometry.

While the algorithm development, product validation and writing of this manuscript is my work, my co-authors have also made substantial contributions. Daniel Zawada helped with implementing the retrieval code into the SASKTRAN framework, and all of the co-authors have provided valuable insights and edits during the writing and revision process.

5.1 Abstract

The Optical Spectrograph and InfraRed Imaging System (OSIRIS) on board the Odin satellite has been used to provide vertically resolved aerosol extinction since 2001. The OSIRIS version 5.07 aerosol product has been used in numerous studies and now provides a 17 year record of global stratospheric aerosol. This work presents the new version 7 OSIRIS aerosol extinction retrieval. A multi-wavelength aerosol extinction algorithm has been developed to reduce particle size assumption biases and improve extinction retrieval in the upper troposphere and lower stratosphere. The algorithm has been applied to the complete set of OSIRIS measurements and is now available for download. The Chen *et al.* (2016) cloud detection algorithm has been adapted for the OSIRIS wavelength range for improved cloud screening and PSC detection, and comparisons after volcanic eruptions and with the CALIPSO-GOCCP product show promising results. The version 7 product shows comparable agreement with version 5.07 when compared to coincident SAGE II and III measurements, and improved agreement with CALIPSO time series.

5.2 Introduction

In the 1960s, in situ measurements began of a layer of particles that extends from the tropopause to approximately 25 km in altitude (Junge *et al.,* 1961). These particles are formed from trace gases including SO_2 and OCS that are transported from the troposphere into the stratosphere where they are converted to H_2SO_4 and combine with water to form liquid droplets (Brock *et al.,* 1995; Hamill *et al.,* 1997). Although OCS is the primary driver of the stratospheric aerosol during background periods (Sheng *et al.,* 2015), even moderate volcanic eruptions can have a profound impact on aerosol levels (Vernier *et al.,* 2011). The last two decades have been punctuated by several of these small-to-moderate eruptions and they have an important impact on climate, both through ozone depletion (Stone *et al.,* 2017) and contributions to the radiative forcing (Solomon *et al.,* 2011; Fyfe *et al.,* 2013a). The importance, as well as variability of the aerosol layer has meant that continuing measurements are of high importance for understanding the larger climate system.

Since Junge's measurements, a host of techniques have been used to study the stratospheric aerosol layer. Balloon measurements continue to be performed and provide an invaluable in situ record of aerosol size and concentration (Deshler *et al.,* 2003). Additionally, numerous space-based remote sensing techniques have been developed to provide global coverage. These began with the occultation technique that was employed on a series of Stratospheric Aerosol and Gas Experiments (SAGE) in 1975. This set of instruments provided the first global measurements of aerosol extinction, during both the highly perturbed conditions after the Mount Pinatubo eruption, and during the quiescent period that followed. However, these occultation measurements ceased for over a decade in mid-2006 with the end of SAGE III, until they were resumed in 2017. To continue the record of stratospheric aerosols, satellite instruments employing the limb scattering technique have been used, including the Optical Spectrograph and InfraRed Imaging System (OSIRIS) (Llewellyn *et al.,* 2004), the SpectroMeter for Atmospheric CHartographY (SCIAMACHY) (Bovensmann *et al.,* 1999), and the Ozone Mapping and Profiler Suite Limb Profiler (OMPS-LP) (Flynn *et al.,* 2006). These instruments have added to both the long-term global record (Thomason *et al.,* 2018), as well as studies of shorter-lived phenomenon such as volcanic eruptions (Bourassa *et al.,*

2012b), meteoric events (Gorkavyi *et al.,* 2013), and forest fires, and continue to monitor stratospheric aerosol levels.

While limb scatter instruments provide high vertical resolution and good sensitivity to background levels of aerosol due to the long path lengths, the measurements are inherently complex. At every point along the instrument line of sight, light both directly from the sun and from a diffuse component scattered by the ground and atmosphere can be scattered into the instrument. Each measurement depends not only on the extinction, as is the case for occultation measurements, but also the scattering properties of the atmospheric constituents. This leads to three main challenges when retrieving aerosol from limb scattered signals that can result in time-dependent biases in the retrieved products.

5.2.1 Phase Function Sensitivity

The nature of limb scatter couples the extinction and phase function information together. Very approximately, the aerosol signal is a product of the extinction and phase function, although this is complicated by extinction along the path and multiple scattering, particularly in backscatter conditions where the single scattered signal is low. Typically, the phase function is determined by assuming an aerosol composition of spherical sulphate droplets consisting of approximately 75% H_2SO_4 and 25% H_2O with a unimodal lognormal particle size distribution, as given by the equation,

$$\frac{dn(r)}{dr} = \frac{N}{\sqrt{2\pi}\ln(\sigma_g)r}\exp -\frac{(\ln r - \ln r_g)^2}{2\ln^2(\sigma_g)}, \tag{5.1}$$

where r_g is the median radius, σ_g the distribution width, and N the aerosol number density concentration. However, bimodal and gamma distributions have also been used (Loughman *et al.,* 2018; Chen *et al.,* 2018). Errors in these assumptions translate to errors in the phase function used in the radiative transfer, and carry through to errors in the retrieved extinction. As the value of the phase function depends on the single scattering angle (SSA), the error in the retrieved extinction will also be a function of the scattering angle. To minimize the error, and obtain information on particle size some retrievals attempt to determine one or more lognormal parameters (Rieger *et al.,* 2014; Malinina *et al.,* 2018); however, the information content in the visible and near-infrared wavelengths is limited and the coupled

extinction-particle size retrievals have important limitations. The version 6 OSIRIS retrieval assumes a constant distribution width, and are constrained by the Infrared channel on OSIRIS which saturates under moderate aerosol loading. Due to this, the version 5 OSIRIS retrieval remains the standard product, and what is compared against in this work. The SCIAMACHY retrievals assume a fixed number density profile, and have not been attempted outside of a limited range of scattering angles. While both products provide important information on particle size, the limitations mean they cannot be used to construct complete global records of aerosol extinction. While the standard extinction-only products are even simpler, assuming a fixed size distribution at all locations and times, they provide coverage of lower altitudes for OSIRIS, and all latitudes for SCIAMACHY; allowing for more complete records of aerosol extinction, and easier use in global climatologies. The following work develops an extinction retrieval that can be applied at all altitudes and latitudes, while reducing some of the limitations of earlier extinction retrievals.

5.2.2 Low Altitude Sensitivity

The Rayleigh scattered signal increases approximately exponentially along with atmospheric density. This can result in a relatively small fraction of the total radiance signal being attributable to aerosol at low altitudes. Additionally, the sensitivity to aerosol decreases as the total atmospheric extinction increases due to a larger fraction of the light being scattered out of the instrument line of sight. Together, these effects result in rapidly decreasing sensitivity at lower altitudes. Longer wavelengths are generally used to minimize these effects and provide better theoretical sensitivity at lower altitude. However, due to instrumental considerations, longer wavelengths often have poorer signal to noise and increased stray light, limiting the extent to which they can be used, particularly in the infrared region. Depending on the retrieval and instrument the wavelength is usually chosen between 675 and 850 nm, and is generally on the long side of the visible spectrum. This spectral region provides good sensitivity to aerosols while maintaining a relatively high signal-to-noise ratio over a wide range of stratospheric altitudes. While occultation and Lidar measurements often retrieve extinction in the 530 nm range, these wavelengths can have poor sensitivity at lower altitudes in limb scattering measurements, making longer wavelengths preferable in most cases.

However, even at the longer wavelengths, lower altitudes can remain problematic and Section 5.4.4 discusses improvements in sensitivity in the Upper Troposphere and Lower Stratosphere (UTLS) region.

Further complicating the UTLS is the possibility of clouds in the field of view. Sulphate aerosols in the upper troposphere and lower stratosphere can be an important component of the total aerosol optical depth, particularly in mid-to-high latitudes after moderate volcanic eruptions (Ridley *et al.,* 2014), making this an important region for accurate measurements. However, the radiance signal from clouds and cloud/aerosol mixtures can appear similar to volcanically enhanced aerosols, so distinguishing them has proved challenging and many methods have been developed to screen clouds from limb aerosol records (Thomason *et al.,* 2013; Normand *et al.,* 2013; Eichmann *et al.,* 2016; Liebing, 2016; Chen *et al.,* 2016). Section 5.4.2 implements an updated cloud detection algorithm applied to the OSIRIS dataset.

5.2.3 High Altitude Sensitivity

Limb scatter aerosol retrievals often use an altitude normalized radiance profile as the measurement vector (e.g. Bourassa *et al.,* 2012a; Loughman *et al.,* 2018). The altitude normalization decreases sensitivity to upwelling radiation as well as biases in absolute calibration and radiative transfer modeling. However, it comes at the cost of increased sensitivity to stray light and any aerosol in the normalization range, strongly coupling errors at these higher altitudes to lower altitudes. See Rieger *et al.* (2018) for a more detailed description of this effect. Stray light tends to be larger at longer wavelengths due to the decreasing signal levels, favoring use of shorter wavelengths, although the magnitude of this effect is difficult to quantify as the precise magnitude of the stray light is generally unknown. Although not strictly addressed in this paper, the reliance on high altitude (∼30-40 km) measurements is an important consideration in aerosol retrievals.

5.3 Algorithm Development

5.3.1 Overview

A multi-wavelength aerosol retrieval is developed here to help address the issues of phase function dependence and lack of low altitude sensitivity when using limb-scattered aerosol measurements. The retrieval assumes a spherically homogeneous atmosphere for the retrieval of vertical profiles of aerosol extinction. Also assumed is a fixed aerosol particle size distribution. The state vector, $\mathbf{x}$, used in the retrieval is the aerosol number density, which is converted to extinction using the assumed the particle size. The inverse problem is solved using the Levenberg-Marquardt procedure (Levenberg, 1944; Marquardt, 1963) to update the state vector, $\mathbf{x}$

$$\mathbf{x}_{n+1} = \mathbf{x}_n + \left[\mathbf{K}^T\mathbf{W}\mathbf{K} + \gamma \mathrm{diag}\left(\mathbf{K}^T\mathbf{W}\mathbf{K}\right)\right]^{-1}\mathbf{K}^T\mathbf{W}\left(\mathbf{y} - F(\mathbf{x})\right), \tag{5.2}$$

where $\mathbf{y}$ is the measurement vector, and F is the forward model used to simulate the measurement vector. The weight given to each measurement, $\mathbf{W}$, is often the inverse of the measurement error covariance matrix, but this is not required. The damping factor, γ, is set to 0.1 for the duration of the retrieval. The retrieval is initialized with an a priori guess, but is insensitive to this parameter, as no penalty is associated with divergence from the a priori values.

5.3.2 The Measurement Vector

The measurement vector is constructed from a combination of measurements to decrease sensitivity to confounding variables including instrument calibration, upwelling radiation and other atmospheric parameters. One of the simplest measurement vectors is a radiance, I, at a single wavelength, λ, normalized by a higher altitude. In this case the vector at altitude j is

$$y_j(\lambda) = \ln(I_j(\lambda)) - \frac{1}{N}\sum_{j=i}^{N-1}\ln(I_j(\lambda)), \tag{5.3}$$

where the range of altitudes from i to $i+N-1$ are used as the normalization. The logarithm of the radiance is often used to avoid the orders of magnitude difference in signal between

the ground and upper range of the retrieval, although this is not generally required if the measurement covariance is also used. A color ratio approach where the long-wavelength radiance is normalized by a shorter wavelength (usually near 470 nm) as well as a high altitude has also been used (Bourassa *et al.,* 2012a; Ernst *et al.,* 2012). In this case,

$$y_j = y_j(\lambda = 750\,\text{nm}) - y_j(\lambda = 470\,\text{nm}). \tag{5.4}$$

The short wavelength can be either positively or negatively sensitive to changes in aerosol at the tangent point, making this normalization beneficial at times and detrimental at others. A series of measurement vector Jacobians is shown in Figure 5.1 for single wavelength measurement vectors at 470 and 750 nm as well a short-wavelength normalized vector. In forward scattering conditions, as shown in the top row, the 470 nm vector is positively sensitive down to approximately 15 km, and nearly zero below this point, while the 750 nm vector is positive essentially down to the ground. In this case, the wavelength normalized vector sees no change in aerosol extinction sensitivity at low altitudes and decreased sensitivity above 15 km. In backscattering conditions, as shown in the second row, both measurements are much less sensitive to aerosol due to the much smaller phase function. However, the 470 nm vector becomes negative below approximately 20 km. Therefore, when a short wavelength is used as a normalization, the sensitivity of the vector is increased over the 750 nm measurement at lower altitudes. Above approximately 20 km, for both measurement geometries, normalization always causes a decrease in sensitivity to aerosol. Although this is a simple example, and a full analysis needs to incorporate measurement noise as is presented later, this indicates that a wavelength normalization can be useful in backscattering cases to improve the aerosol sensitivity in the UTLS region.

The sensitivity also depends on particle size, and this can affect both the magnitude and sign of the measurement Jacobian. Although the number of particles with radii less than approximately 50 nm in the stratosphere can be relatively large, their optical cross sections are generally too small to contribute meaningfully to aerosol extinction levels, and the effect on limb scattering measurements is further dependent on the phase function and other atmospheric parameters. To examine this in more detail it is illustrative to briefly explore some optical properties of a lognormal distribution of particles. The top panel of Figure

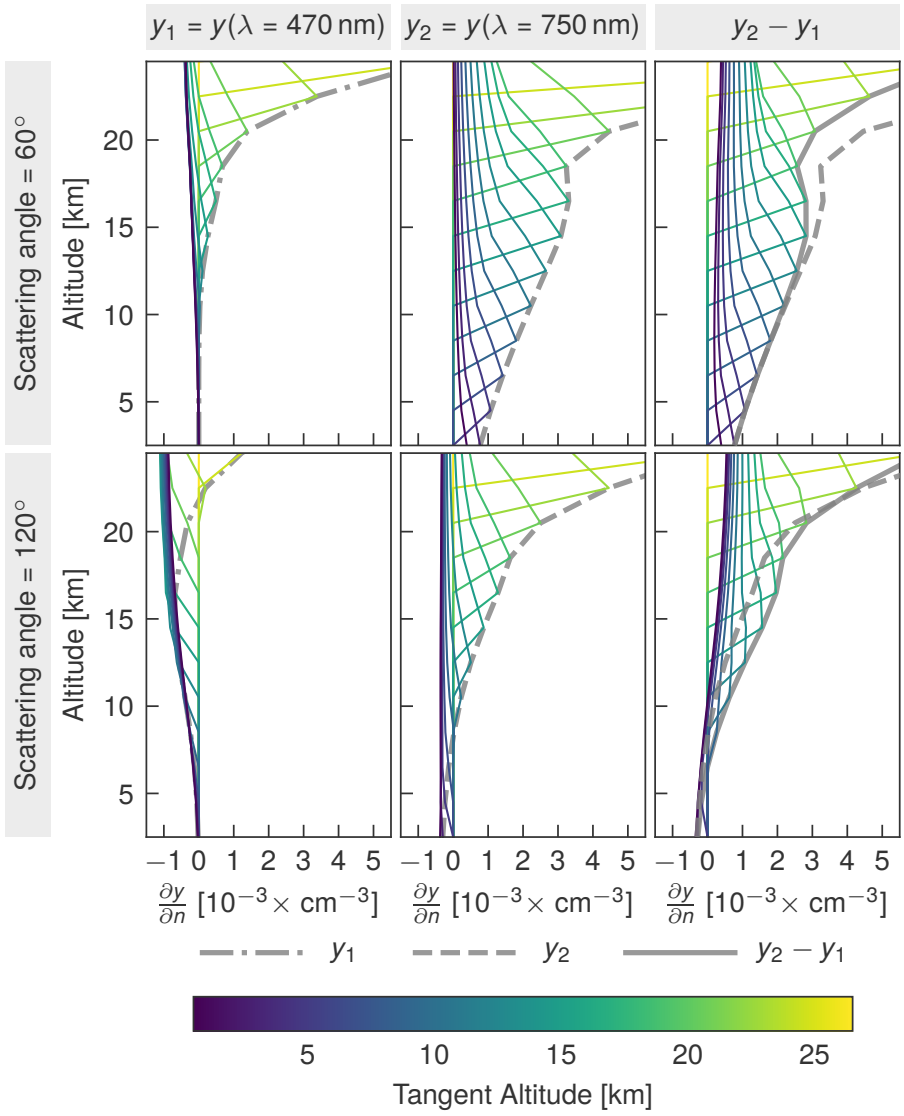

Figure 5.1: The sensitivity of three different measurement vectors to a perturbation in aerosol extinction. The top row shows a measurement geometry with solar zenith angle of 85° and single scattering angle of 60°. The bottom row shows the same solar zenith angle, but with a scattering angle of 120°. The left and center column shows a measurement vector from single wavelengths at 470 and 750 nm respectively. The right column shows a short wavelength normalized vector, as defined in Equation 5.4. The color of the line indicates the tangent point altitude of the measurement, as indicated by the colorbar. For reference, the gray lines indicate the sensitivity at the tangent altitude to changes at the tangent altitude.

5.2 shows the distribution of particle number density for a typical stratospheric lognormal distribution. The majority of particles are smaller than 100 nm, with the peak concentration around 65 nm for this particular distribution. However, this is not necessarily representative of where the extinction signal is large. Extinction can be determined directly as an integration over the size distribution,

$$k_\lambda = \int_0^\infty \sigma(r,\lambda)\frac{dn(r)}{dr}dr, \tag{5.5}$$

where $\sigma(r,\lambda)$ is the optical cross section computed from Mie theory, and also depends on the index of refraction. The second panel in Figure 5.2 shows $\partial k/\partial r$ at 750 nm for the same distribution. Over 95% of the extinction at 750 nm is generated by particles larger than 100 nm. This indicates for occultation measurements these smaller particles play little to no role. However, for a limb scattering measurement, the aerosol signal from the tangent point is approximately proportional to the extinction multiplied by the phase function. So, ignoring multiple scattering, the tangent point contribution to the aerosol measurement vector can be roughly estimated as

$$y(\lambda) \sim \int_0^\infty \sigma(r,\lambda)p(r,\lambda,\Theta)\frac{dn(r)}{dr}dr. \tag{5.6}$$

The proportionality comes from the fact that integration along the line of sight and multiplication by the incoming solar radiation is neglected. The final panel in Figure 5.2 shows $\partial y/\partial r$ for scattering angles of 30, 60 and 120°, again for 750 nm. In strongly forward scattering cases the signal is dominated by particles larger than approximately 150 nm. However, for backscattering conditions, the signal is much weaker overall, with smaller particles playing a much more prominent role due to the more Rayleigh-like phase functions.

From equation 5.6 we have the sensitivity of our measurement vector y to a change in the number of particles at radius r as

$$\frac{\partial y(r,\lambda)}{\partial n} \sim \sigma(r,\lambda)p(r,\lambda,\Theta). \tag{5.7}$$

Although, highly approximative, this gives a general indication of what particle sizes are important for limb scattering signals. Figure 5.3 shows this approximate $\partial y(r)/\partial n$ for three scattering angles for a vector at 750 nm. The dominant feature is the rapid increase in sensitivity to particles as radius increases due to the increase in the optical cross section. As the volume of aerosol increases with r^3, this unsurprisingly shows that y is generally more

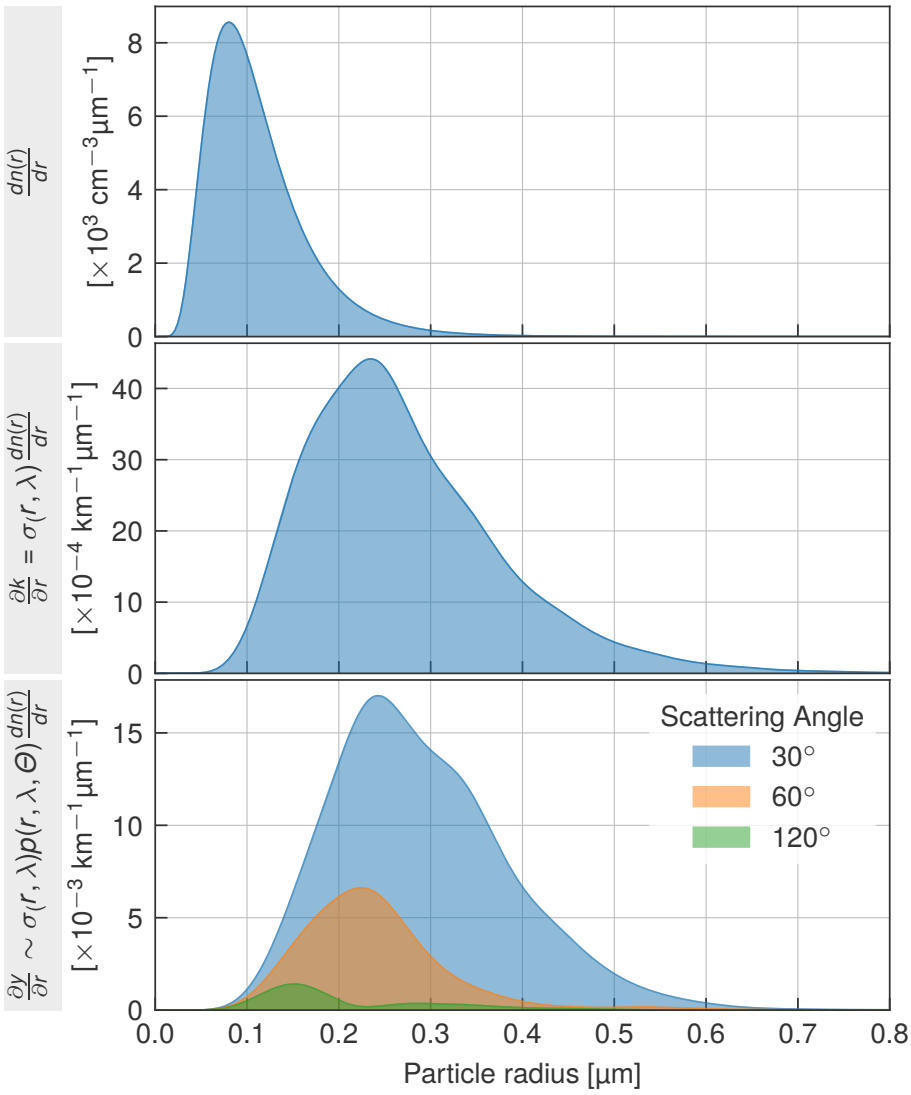

Figure 5.2: The top panel shows the number density of a typical lognormal distribution with median radius of 100 nm and width of 1.5. The center panel shows the extinction at 750 nm for this distribution. The last panel shows the extinction distribution multiplied by the phase function for a range of scattering angles as an approximation to the limb scattering aerosol signal, also at 750 nm.

sensitive to larger increases in aerosol loading than small. Equation 5.7 can be rewritten in terms of the change in aerosol volume, V as

$$\frac{\partial y(r,\lambda)}{\partial V} \sim \frac{3}{4r^3}\sigma(r,\lambda)p(r,\lambda,\Theta). \tag{5.8}$$

This has the physical interpretation of how a given mass of aerosol will change the measurement, y, if it is added to the atmosphere at different particle radii, and has been used previously when looking at occultation measurements (e.g. Thomason *et al.,* 1993). The quantity $\partial y/\partial V$ is shown in the center panel of Figure 5.3. Even with equal volume, particles with radii less than 50 nm have very little contribution to the signal at any scattering angle. While this interpretation is physically meaningful, for this work the retrieved quantity remains extinction, and so it is also useful to examine $\partial y/\partial k_{\lambda_{ret}}$. This is shown in the final panel of Figure 5.3 for $\lambda_{\text{ret}} = 750$ nm and is calculated as

$$\frac{\partial y(r,\lambda)}{\partial k_{\lambda_{\text{ret}}}} \sim p(r,\lambda,\Theta)\frac{\sigma(r,\lambda)}{\sigma(r,\lambda_{\text{ret}})}. \tag{5.9}$$

This indicates how sensitive the measurement vector is to changes in the extinction due to particles of size r, and would ideally be a flat line, i.e., the measurement sensitivity would be independent of the particle size causing the extinction. This is the case for occultation measurements and the reason extinction is such a robust quantity from the occultation measurement technique. For limb scattering, however, the variation can be quite large with measurements more than an order of magnitude more sensitive at some radii than others, and also depends strongly on the viewing geometry.

Although this provides a rough estimate of what particle sizes are important, a more accurate way to compute the limb scattering sensitivity to particle size variations is to model the signal using a reasonable background state, then add particles with a monodisperse size at a specific altitude, j, and model the signal once more. The difference between the two results at altitude i is then the numerical derivative $\partial y(r,\lambda)_i/\partial n_j$ for particles of radius, r. The number of particles in the perturbation can be easily adjusted as to keep the extinction perturbation constant across r, yielding $\partial y_i/\partial k_{j,\lambda}$. Repeating this at various values of r can then be used to determine the sensitivity to particles of different sizes.

Figure 5.4 shows the sensitivity of a measurement vector, $\partial y_j/\partial k_{j,\lambda}$, at four different wavelengths to a perturbation in extinction due to monodisperse particles. Each row indicates the sensitivity of a measurement with tangent altitude j to an extinction perturbation at that same altitude. The analytical sensitivities from Equation 5.9, normalized to the peak numeric value, are plotted as dashed lines in the 28.5 km panels for reference. They agree very well

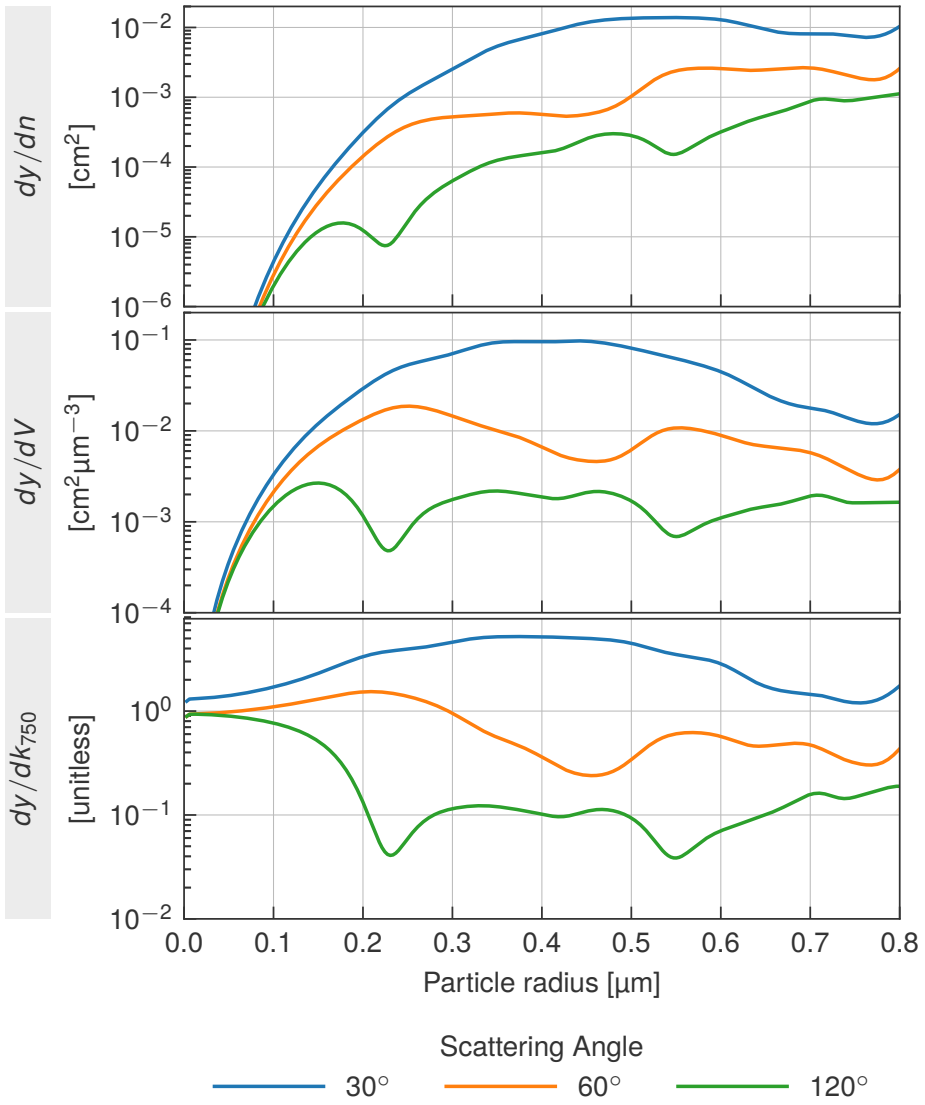

Figure 5.3: Analytic approximations to the 750 nm measurement vector sensitivity as function of particle radius. The top panel shows the sensitivity to changes in number density, the middle panel to changes in aerosol volume, and the bottom panel to changes in extinction at 750 nm.

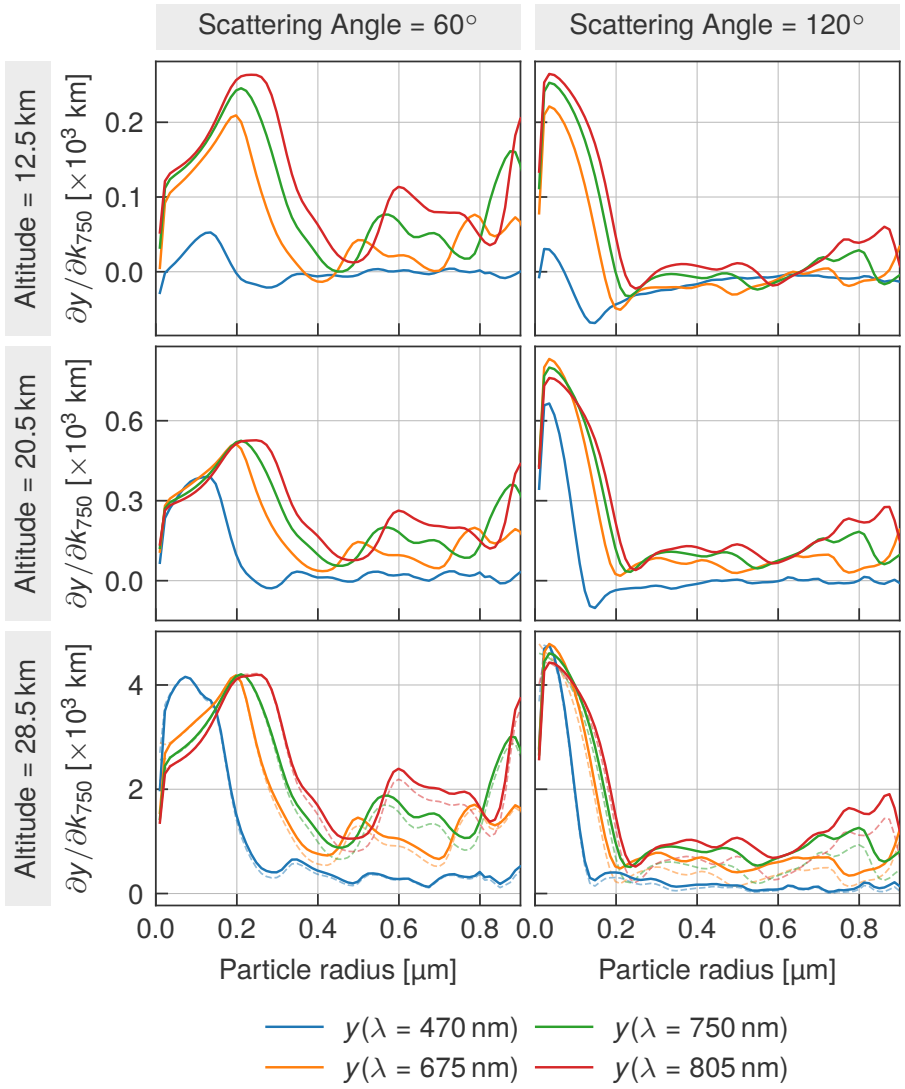

Figure 5.4: The sensitivity of three different measurement vectors to a perturbation in the aerosol size distribution. Left column shows the sensitivity for a forward scattering geometry and the right for a backscattering case. Each row indicates the sensitivity at a particular altitude to perturbations at that same altitude. The dashed lines show the analytic sensitivity calculated from Equation 5.9.

with the numeric derivatives at high altitudes, although are substantially less accurate below approximately 15 km and in backscattering conditions where large amounts of scattering out of the line of sight relative to the signal can cause negative values not captured in the simpler approximations. The 750 nm wavelength is more sensitive in general than the 470 nm

vector, but particularly to larger particles and at low altitudes, with a peak sensitivity to particles with a radius in the 100 to 200 nm range, depending on the geometry. The 470 nm measurements have a peak sensitivity in the 50 to 100 nm range, and at low altitudes the Jacobian is often negative for particles larger than 100 to 200 nm. This causes the wavelength normalized vector to have less sensitivity to particles smaller than 100 nm.

Figure 5.4 also illustrates the sensitivity of the measurements to changes in particle size distributions. If these curves were flat, then any particle size distribution would produce the same measurement vector, and the same retrieved extinction; it is the variability of the sensitivity with particle radius that causes the dependence on the assumed size distribution. Backscattering geometries in particular have a very sharp cutoff at particle sizes between 150 and 200 nm where sensitivity drops to nearly zero, making measurements highly sensitive to changes in the size distribution near this point. At lower altitudes the 470 nm measurement vector has a negative, but much broader response, reducing the dependence on the particle size distribution. Additionally, while the sensitivity of the wavelengths in the visible and near-infrared range are not unique enough to retrieve a particle size distribution, the response from each wavelength is slightly different, yielding the possibility that a measurement vector that uses a combination of wavelengths is less sensitive to particle size. Unfortunately, due to the limited wavelength range available from limb scattering instruments, and the non-orthogonality of the measurements a flat response cannot generally be achieved, and indeed even if it could, it may decrease the sensitivity to extinction sufficiently that measurement noise swamps the signal. While a flat response cannot generally be attained, this does not preclude improving the measurement vector to reduce biases. A measurement vector that is consistently sensitive over a range of particle sizes across measurement geometries has the potential to reduce scattering angle dependencies and resultant seasonal and latitudinal biases. Instead of attempting to force a flat response at the expense of extinction sensitivity, the measurements at different wavelengths can be combined to maximize sensitivity to a reasonable size distribution. This will produce a measurement vector that has good sensitivity to extinction for realistic cases, and will tend to produce measurement vectors that are similarly sensitive to particle size, so far as is possible with the available wavelengths. In the following section a retrieval is developed that uses a variable wavelength normalization

to increase the sensitivity to extinction and help decrease the dependence on measurement geometry.

5.3.3 Implementation

The measurement vector, $\mathbf{y}$, can be written as a linear combination of measurement vectors at individual wavelengths as

$$y_j = \sum_i a_j(\lambda_i) y_j(\lambda_i). \tag{5.10}$$

Although past limb scatter retrievals have used $a(\lambda) = \pm 1$, e.g, Equation 5.4, this is not a strict constraint and $a_j(\lambda)$ can assume any value, including one that changes with altitude. Stacking the measurement vectors at each individual wavelength, $\mathbf{y}(\lambda)$, into a single vector $\mathbf{y}'$, the combined vector can be written in matrix form as

$$\mathbf{y} = \mathbf{A}\mathbf{y}', \tag{5.11}$$

where $\mathbf{A}$ is a matrix that produces a linear combination of measurement vectors at different wavelengths. In Equation 5.2 this can be implemented by constructing the weighting matrix $\mathbf{W}$ such that

$$\mathbf{W} = \mathbf{A}\mathbf{S}_\epsilon^{-1}\mathbf{A}^T, \tag{5.12}$$

where $\mathbf{S}_\epsilon$ is the measurement error covariance matrix. Setting $\mathbf{A} = \mathbf{I}$ reduces to the conventional $\mathbf{W} = \mathbf{S}_\epsilon^{-1}$, and serves to minimize the weighted square error of the residuals. However, as described above, to improve aerosol sensitivity and reduce the dependence on the measurement geometry, we would like to combine wavelengths that have high sensitivity to the extinction in addition to low noise on the measurement. Combining the measurements in such a way, instead of using $\mathbf{y}'$ directly, allows for a measurement vector with similar sensitivities across measurement geometries. The matrix $\mathbf{A}$ is therefore constructed to produce a linear combination of wavelengths that minimizes the diagonal elements of the measurement error covariance, $\mathbf{S}_x$, which from Rodgers (2000) can be computed as,

$$\mathbf{S}_x = \mathbf{G}\mathbf{S}_\epsilon\mathbf{G}^T, \tag{5.13}$$

and $\mathbf{G}$ is the gain matrix, or in the case of Eq. 5.2,

$$\mathbf{G} = \left[\mathbf{K}^T\mathbf{S}_\epsilon^{-1}\mathbf{K}\right]^{-1}\mathbf{K}^T\mathbf{S}_\epsilon^{-1}. \tag{5.14}$$

If the Jacobian, $\mathbf{K}$, is invertible then this reduces to

$$\mathbf{G} = \mathbf{K}^{-1}. \tag{5.15}$$

The algorithm then proceeds as follows:

1. Search for the weights $\mathbf{A}$ that minimize the diagonal elements of $\mathbf{S}_x$. For this search each altitude is treated independently to help reduce the computation burden. As it is the relative weight of the vectors that matters the norm of each column of $\mathbf{A}$ is set to one.

2. Iteratively retrieve the aerosol extinction using Eq. 5.2. Aerosol is retrieved from below the normalization altitude to the lowest altitude at which the Jacobian exceeds 2×10^{-4} km. Smaller than this and it is difficult to ensure that even the sign of the Jacobian is correct as it depends strongly on the particular size distribution chosen. The a priori values at and above the normalization region are scaled to match the value at the highest retrieved altitude. Below the retrieval values are tapered back to the a priori value.

3. Repeat steps 1 and 2. After the first iteration the extinction is approximately correct, and so the second iteration couples the wavelength weights to the retrieved extinction.

The following section applies this algorithm to the OSIRIS measurements.

5.4 OSIRIS version 7

OSIRIS (Llewellyn *et al.,* 2004) was launched in 2001 on board the Odin satellite into a near-terminator orbit and continues operation. The spectrograph has a wavelength range of 280 to 810 nm with a spectral resolution of approximately 1 nm. OSIRIS scans the limb from 7 to 75 km with measurements every 2 km and vertical resolution of 1 km at the tangent point. OSIRIS views in the tangent plane of the orbit which produces single scattering angles between 60 to 120 degrees depending on the latitude and time of year.

Currently, OSIRIS aerosol retrievals are processed using the version 5.07 algorithm and includes retrieval of NO_2, aerosol extinction, and ozone (Degenstein *et al.,* 2009). Since

the release of version 5.07 a pointing adjustment to the instrument line of sight to correct a drift in the satellite attitude has been calculated and this correction is also included in version 7 (Bourassa *et al.,* 2018). This correction has important ramifications for long-term ozone trends, but a smaller affect on aerosol profiles. Full descriptions of the algorithm are described by Bourassa *et al.* (2007) and Bourassa *et al.* (2012a). For reference, the version 5.07 aerosol retrieval uses the MART relaxation technique that simplifies to the Chahine method (Chahine, 1972) for aerosol extinction as a single measurement vector is used. Extinction is retrieved at 750 nm using the short wavelength normalized vector shown in Equation 5.4.

Version 7 retrieves only aerosol extinction, and so relies on additional external atmospheric constraints. Pressure and temperature profiles from the ECMWF ERA-Interim reanalysis (Dee *et al.,* 2011) are interpolated to the OSIRIS scan location. Ozone values retrieved using the version 5.07 algorithm are used, as well a NO_2 climatology from the PRATMO photochemical box model (McLinden *et al.,* 2000). Effective Lambertian reflectivity is retrieved at 675 nm before each aerosol iteration and assumed to be the same for all wavelengths used. The aerosol phase function used is computed using Mie scattering theory assuming a lognormal distribution with a width of 1.6 and median radius of 80 nm, with refractive indices from Palmer *et al.* (1975) assuming a 75/25 mix of H_2SO_4/H_2O, the same as previous versions. The inversion uses the SASKTRAN radiative transfer model to simulate the OSIRIS measurements (Bourassa *et al.,* 2008; Zawada *et al.,* 2015). For the OSIRIS version 7 retrieval wavelengths of 470, 675, 750, and 805 nm are used. Due to instrumental considerations wavelengths between 475 and 530 nm are not available, and wavelengths near 600 nm are not used to avoid strong ozone absorption. Additional wavelengths between 675 and 805 nm do not provide substantially different sensitivity to aerosols, so the choice of four wavelengths is a compromise between measurement noise and computational time.

Figure 5.5 shows an example of the the altitude dependent weights for scans between 10°S and 10°N. Only measurements where Odin is traveling southward are used to isolate measurements with similar scattering angles. At high altitudes the aerosol loading is low, and the dominant source of error is the measurement noise, leading to the 470 nm measurement being weighted the most heavily. At lower altitudes the shorter wavelengths have poor sensitivity and the retrieval shifts to longer wavelengths. This is true until approximately

15 km. At this point, even the 805 nm measurements have minimal sensitivity to aerosol under backscattering conditions. However, here the 450 and 675 nm measurements become negatively sensitive, i.e. increasing aerosol levels reduces the signal, and the shorter wavelengths can again be used. The altitude at which the retrieval shifts to longer wavelengths, and then back to shorter depends primarily on the scattering angle, with backscattering geometries favoring shorter wavelengths sooner. However, it also depends on aerosol loading, with enhanced aerosol conditions also favoring shorter wavelengths in the UTLS region.

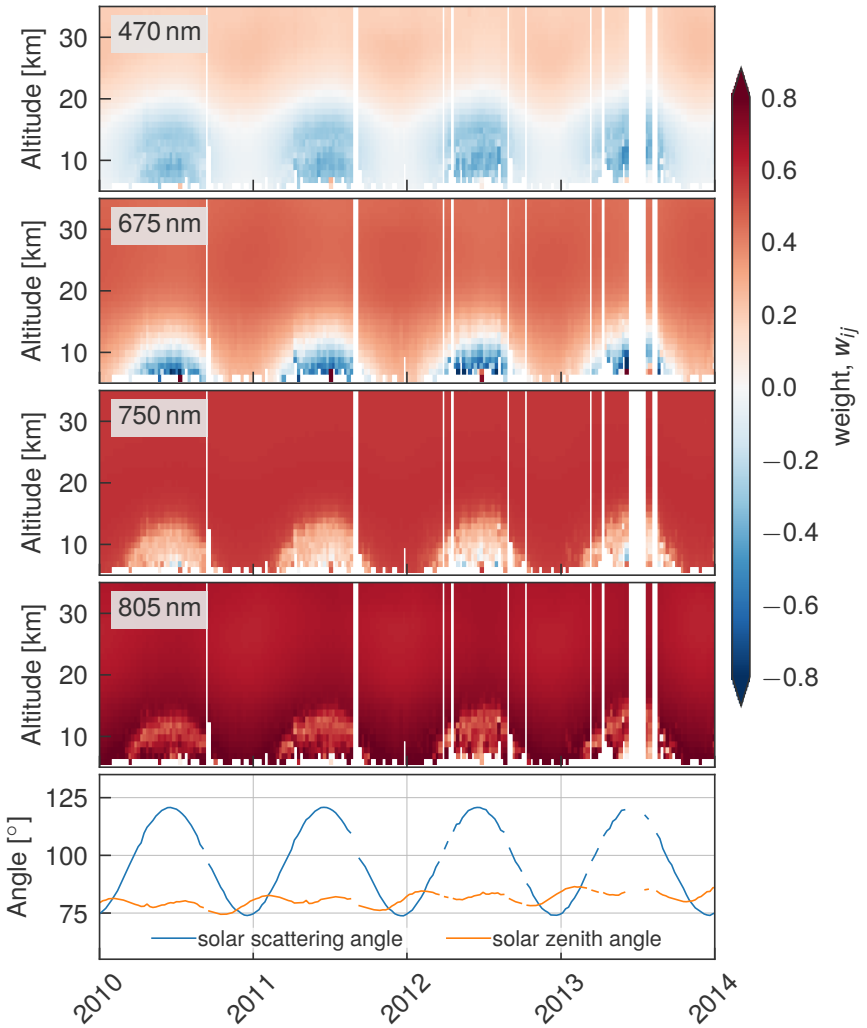

Figure 5.5: The top four panels show the weights used at each wavelength as a function of altitude and time for the OSIRIS descending node binned into 14-day averages. The last panel shows the solar scattering and solar zenith angles for the same node.

5.4.1 Scattering Angle Biases

One of the major goals of this work is to improve the sensitivity to the assumed particle size, and Odin's orbit provides a convenient test of this due to its terminator orbit. OSIRIS samples the same point on the globe approximately 12 hours apart, once on the ascending node and once on the descending. These two nodes can have drastically different scattering angles, and therefore, despite sampling the same location, have different retrieved aerosol values due to errors in the assumed aerosol phase function, dictated by the assumed particle size distribution.

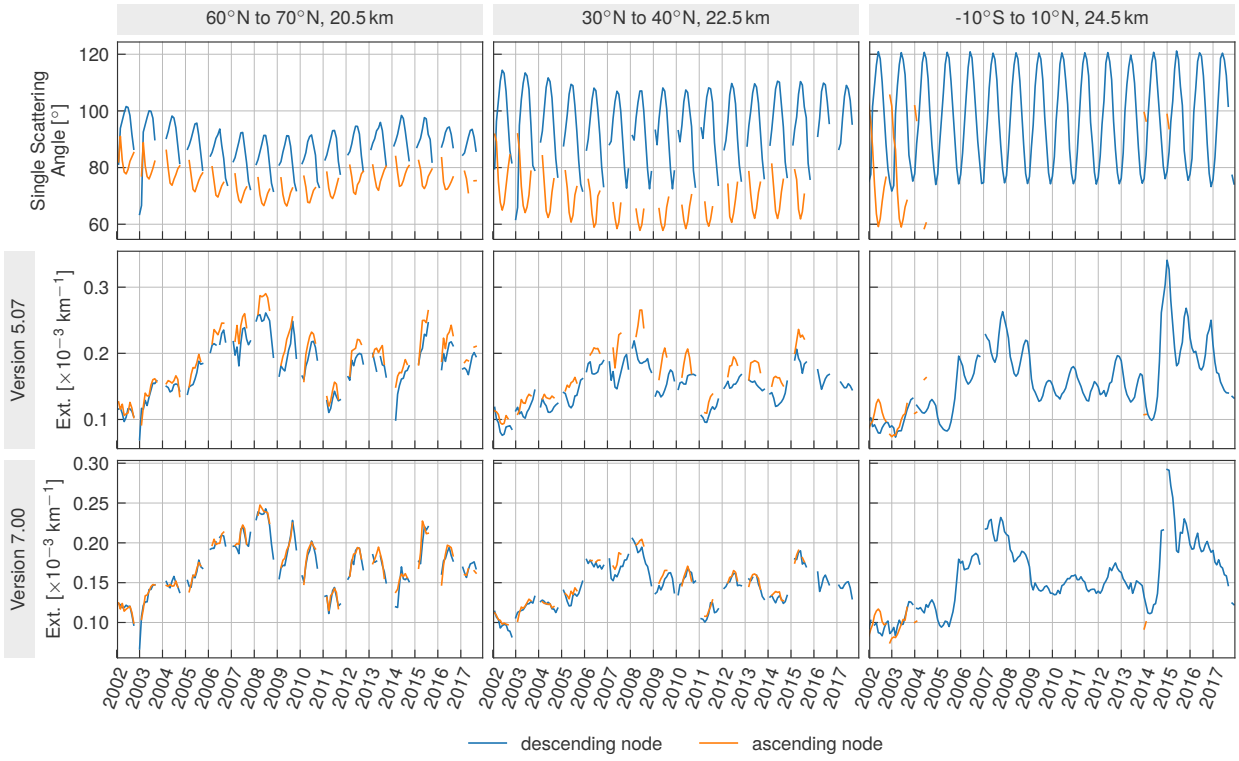

Figure 5.6: Comparison of the monthly averaged aerosol extinction retrieved on the ascending (orange) and descending (blue) nodes in three latitude bands.

Figure 5.6 shows the monthly averaged aerosol extinction retrieved at three altitudes and latitudes using the OSIRIS data, split into the ascending and descending nodes. The top row shows OSIRIS scattering angle for three latitude bands. The higher latitudes constantly measure both nodes throughout the mission, however the orbital drift pushes the ascending node past the terminator for more tropical latitudes after about 2004. The middle row shows

the extinction from version 5.07 retrieval, also grouped into ascending/descending conditions. There is a clear separation of the retrieved extinction between the two nodes that is dependent on the scattering angle. This dependence is stronger at mid and tropical latitudes and larger after 2006, when the stratospheric aerosol has been increased by a series of small volcanic eruptions (Vernier *et al.,* 2011). In the tropics the two nodes cannot be compared beyond the first few years due to an orbital precession which pushes the ascending node past the terminator. However, there is still a clear seasonal cycle that correlates very well with the scattering angle. The results from version 7 are shown in the bottom row. Mean extinction values remain very similar to version 5.07, however the separation between the nodes has been greatly reduced for all time periods. Although some differences remain in the tropics, the seasonal cycle has also been reduced substantially.

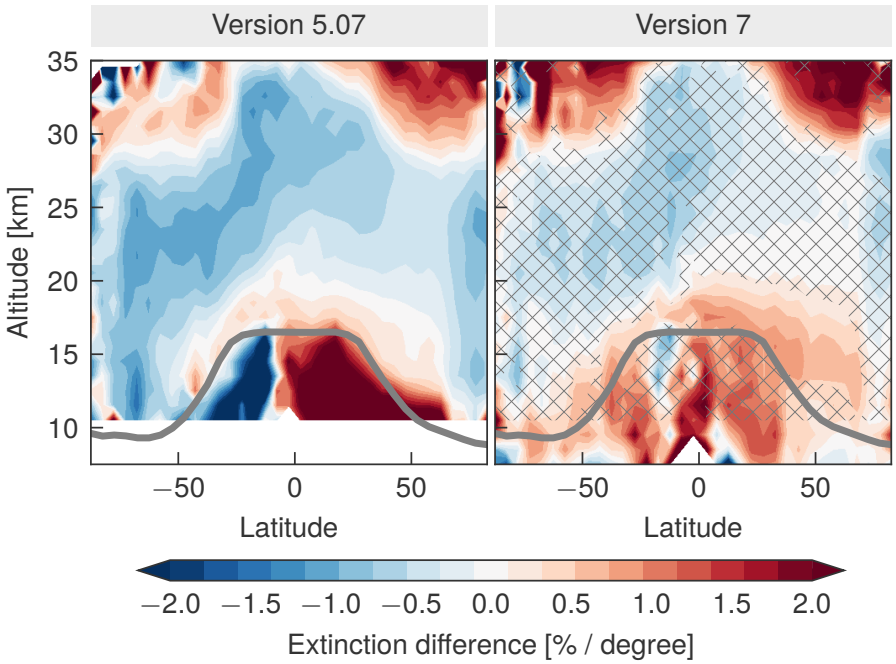

Figure 5.7: Comparison of the zonally averaged extinction from the ascending and descending nodes, normalized by the difference in scattering angle, or $\frac{k_{\text{desc}} - k_{\text{asc}}}{(\text{SSA}_{\text{desc}} - \text{SSA}_{\text{asc}}) \cdot k_{\text{mean}}} \times 100\%$. The hatched region shows the areas where version 7 has less dependence on scattering angle. The gray line shows the mean tropopause altitude.

Reduction of the seasonal cycle is evident in most, but all locations. Figure 5.7 compares the differences between the ascending and descending nodes as a function of latitude and

altitude. Here, the extinction difference has been computed as

$$\text{median}\left(\frac{k_{asc}-k_{desc}}{(SSA_{asc}-SSA_{desc})\cdot k_{mean}}\right)\times 100\%,$$

where the extinction, k, and scattering angle, SSA, are the monthly mean values. The subscripts *asc* and *desc* denote the ascending and descending nodes respectively. In version 5.07, for most regions in the stratosphere, a one degree change in scattering angle would cause approximately a 1% change in the retrieved extinction. In version 7, shown in the right panel, this dependence is generally reduced to approximately 0.5% per degree. Hatched regions indicate where version 7 shows less dependence on the scattering angle than version 5.07. Improvements are seen everywhere except at approximately 3-5 km above the tropopause in the northern hemisphere, where version 7 shows a stronger dependence on scattering angle. This region generally has high values of aerosol which, when coupled to with the low altitude, leads to poor sensitivity.

5.4.2 Cloud Detection

Before improvements in the UTLS can be fully explored, clouds must first be filtered from the retrieved extinction. Chen *et al.* (2016) and Eichmann *et al.* (2016) developed similar techniques to filter clouds from limb scattered data based on the assumption that clouds cause a steep vertical gradient in the radiance profile with longer wavelengths having a stronger response due to the larger size of cloud particles. As a filter criteria Chen *et al.* (2016) define the value,

$$\ln(R)\equiv\frac{\partial\ln I(\lambda_1)}{\partial z}-\frac{\partial\ln I(\lambda_2)}{\partial z} \tag{5.16}$$

where z is the altitude. For their application to the OMPS-LP instrument they used wavelengths of 674 and 868 nm, and recommended a threshold value of $0.15\,\text{km}^{-1}$ at these wavelengths. While this generally provides good results for OMPS-LP they note that during periods of increased volcanic loading this technique can flag what is likely to be aerosol as clouds; an affect that will be exacerbated when applying this technique to OSIRIS due to the more limited wavelength range available. Figure 5.8 shows the distribution of OSIRIS measurements in $\ln(R)$ and retrieved extinction space. $\ln(R)$ is computed at 675 and 805 nm and to make the values of $\ln(R)$ consistent with those discussed in Chen *et al.* (2016) a correction

of 1.48 (the ratio of OMPS-LP to OSIRIS wavelength ranges) is applied to account for the smaller wavelength range of OSIRIS. The OSIRIS measurements are also interpolated to a 1 km grid to approximate the vertical sampling of the OMPS-LP instrument. The dashed line indicates the $0.15\,\mathrm{km}^{-1}$ cut-off used for the OMPS-LP instrument. Unfortunately, there is no clear separation between cloud and aerosol measurements, either according to extinction or $\ln(R)$. However, there is a weak correlation between extinction and $\ln(R)$, so values with high $\ln(R)$ also have a tendency to have large extinction, extending the tail of distribution when viewed in this two dimensional space.

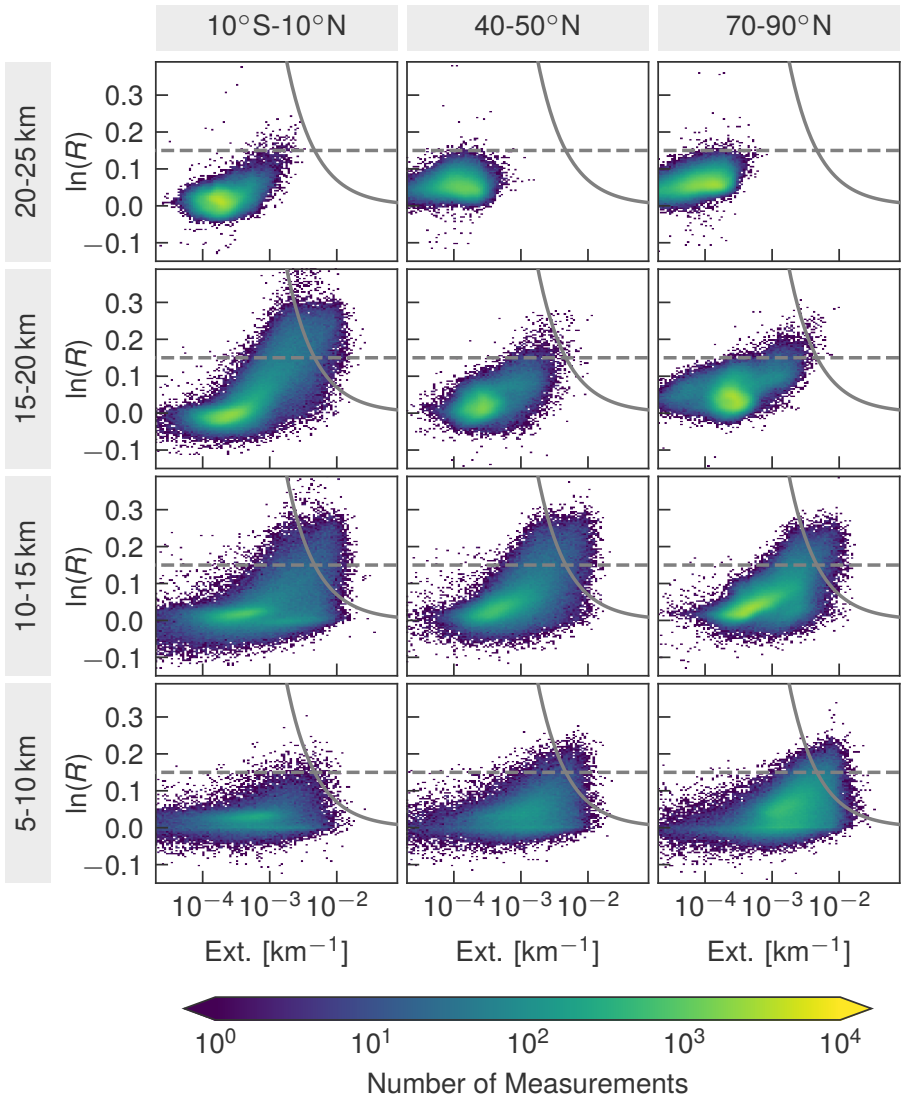

Figure 5.8: Distribution of OSIRIS measurements for the duration of the mission in $\ln(R)$ and extinction space for a selection of altitude and latitude ranges. The color indicates the number of measurements with these values. The dashed line shows the threshold used in Chen *et al.* (2016), and the solid line shows $k \cdot \ln(R) = 7 \times 10^{-4}\,\mathrm{km}^{-2}$.

To help improve the discrimination between volcanic aerosol and clouds a small modification is made to the Chen *et al.* (2016) cloud algorithm. The value $\ln(R)$ is multiplied by the extinction, k, before setting a threshold value. This incorporates the additional assumption that clouds will tend to have larger extinction values than aerosols, as has been used previously in SAGE II algorithms (Kent *et al.,* 1993; Thomason *et al.,* 2013). The solid line

in Figure 5.8 shows the line of constant $k \cdot \ln(R) = 7 \times 10^{-4}\,\mathrm{km}^{-2}$ that is used in this work to discriminate between aerosol and cloud. In general, this leads to fewer measurements being flagged as clouds than the Chen *et al.* (2016) method, tending to increase the extinction after volcanic eruptions, even though some additional measurements with large extinction are now removed.

As a case study, Figure 5.9 compares the Chen *et al.* (2016) method with that employed in this work for the period around the 2009 Sarychev eruption. The first column shows the Chen *et al.* (2016) method applied to the OSIRIS data. The first panel is the $\ln(R)$ quantity computed at 675 and 805 nm for the period from March to December 2009 in one week averages between 50°N and 70°N. Note that while weekly averages are shown here, the flagging itself is done on a scan-by-scan basis. Clouds are clearly highlighted below approximately 15 km until the Sarychev eruption on 15 June 2009, at which point the $\ln(R)$ value in the aerosol layer is often as large as where clouds are expected. The effect this has on the cloud flagging can be seen in the panel below. After the eruption, the early volcanic plume is often flagged as containing clouds, reducing the average extinction measured after an eruption. Although the $0.15\,\mathrm{km}^{-1}$ threshold could be tuned for the OSIRIS wavelengths to reduce aerosol-as-cloud misclassification, the similarity in values between clouds and volcanic aerosols makes improvements difficult without including many more clouds. The center column shows the updated cloud algorithm, using $k \cdot \ln(R)$. Clouds are clearly visible below approximately 15 km, and while the value of $k \cdot \ln(R)$ does increase after the volcanic eruption, it is less likely to rise to the level typically seen in cloudy conditions, making the threshold easier to set. For this work a value of $7 \times 10^{-4}\,\mathrm{km}^{-2}$ was empirically determined to provide good discrimination.

The final column of Figure 5.9 shows the differences in the cloud fraction (row 2) between the two algorithms, and the difference in retrieved extinction (row 3). The updated algorithm generally flags clouds at slightly lower altitudes, placing more below the tropopause, denoted by the grey line. It also removes less aerosol after the Sarychev eruption, causing the zonally averaged extinction to increase by approximately 10 % for the months following the eruption and up to 20 % in isolated periods. It should be noted however, that while this technique flags less aerosol as cloud, it is not a perfect classification. The inclusion of extinction in the

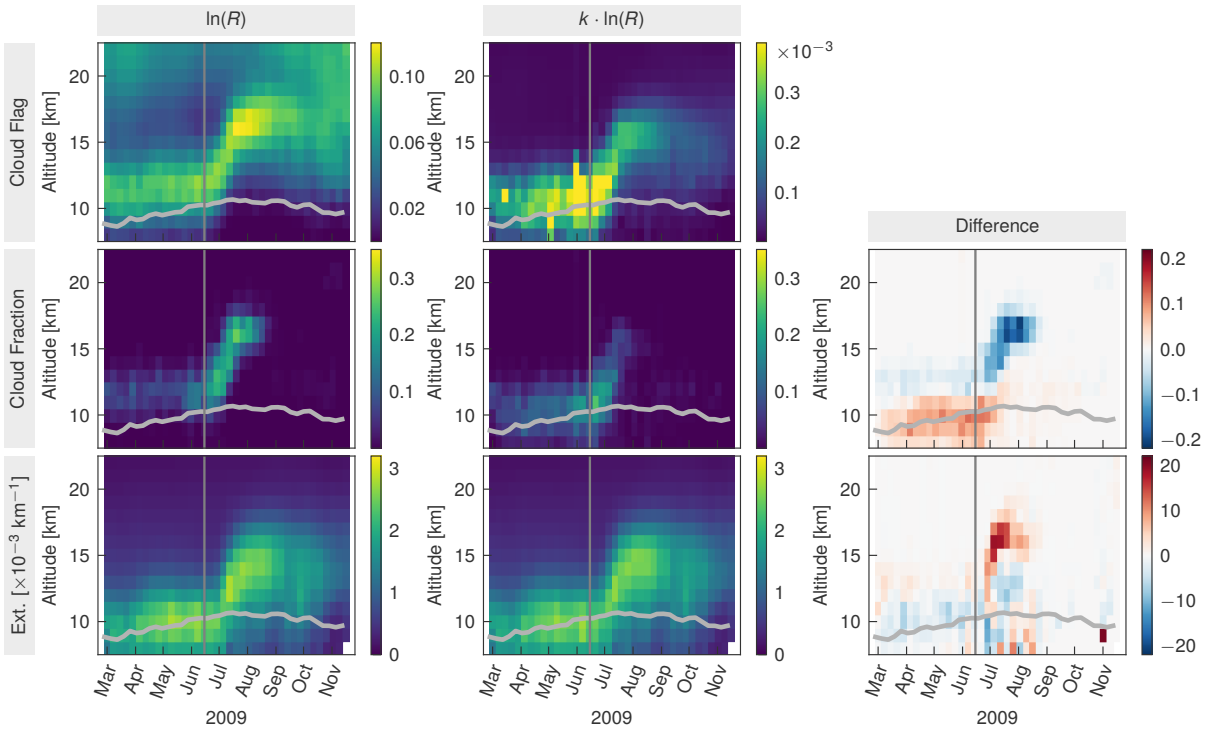

Figure 5.9: Comparison of the Chen *et al.* (2016) cloud detection algorithm applied to OSIRIS data, and the updated method used in this work. The left column shows results from the $\ln R$ quantity used in the Chen algorithm, and the center column from the updated method. The right column shows the difference in the effects on the final products. The top row shows the weekly averaged value of the cloud flag. The middle row shows the weekly averaged cloud fraction, and the last row the cloud free extinction product. All plots are zonally averaged between 50°N to 70°N. The difference in cloud fraction is computed as $CF_{k\cdot\ln R} - CF_{\ln R}$. The difference in extinction is computed as $(k_{k\cdot\ln R} - k_{\ln R})/k_{\ln R} \times 100\%$. The vertical gray line marks the eruption of Sarychev Peak on 15 June 2009, and the light gray line denote the tropopause altitude.

threshold also means it will be more likely to miss flagging thin or spatially inhomogeneous clouds, as the smaller extinction values mean these cases are less likely to meet the threshold value. Any threshold technique is likely to misclassify some cases, especially in the case of low altitudes where there may be a mix of both clouds and aerosol. Additionally, while fewer cases of aerosol are flagged as cloud, it is not a perfect discrimination, and high levels of aerosol such as immediately following an eruption are still occasionally flagged as clouds.

Therefore, for studies involving the immediate evolution of volcanic plumes, where aerosol levels are high and still spatially inhomogeneous, it is recommended that the sampling of the OSIRIS instrument is taken into account; in the case of model comparisons by sampling at comparable locations and altitudes, or when comparing with other instruments through coincident comparisons, rather than the use of zonally averaged quantities when possible. The retrieved extinction values without cloud clearing applied are also provided in the final version 7 product for cases when distinction between clouds and aerosol may be ambiguous.

It is also useful to briefly explore the retrieved cloud distributions as a check on the technique and chosen threshold. However, comparison of cloud measurements is complicated by the different sampling and sensitivities of various instruments. The long path lengths of limb instruments make them sensitive to thin cirrus clouds, but essentially blind to anything below a layer of cloud or thick aerosol. Conversely, nadir viewing instruments have less sensitivity to thin clouds, but can penetrate to lower layers. Different satellite orbits also affect the local time of the measurements making climatologies harder to compare. Chepfer *et al.* (2010) used the Cloud-Aerosol Lidar and Infrared Pathfinder Satellite Observations (CALIPSO) data to develop the GCM Oriented Cloud CALIPSO Product (GOCCP). While designed for comparison with GCMs it provides a convenient first test of the OSIRIS cloud flag as it has essentially global coverage of cloud fraction and cloud cover over the majority of the OSIRIS mission. This allows for sampling of the GOCCP at OSIRIS scan locations to avoid sampling biases. Comparisons with the CALIPSO-GOCCP dataset shows good agreement, both in terms of altitude and spatial distribution of cloud fraction, as shown in Figure 5.10. The top row shows the zonally averaged cloud fraction between 2006 and 2018, with OSIRIS data on the left and CALIPSO-GOCCP on the right. Both datasets show a clear maximum in cloud fraction in the tropics near 15 km, with lows near $\pm 25°$, followed by a cloud layer that follows the tropopause. Generally, OSIRIS measures somewhat higher fractions of clouds and places them at slightly higher altitudes. This is at least partially due to the threshold set in the CALIPSO-GOCCP, which will only detect clouds with an optical depth greater than approximately 0.03, missing many of the sub-visual cirrus clouds. Chepfer *et al.* (2013) investigated the differences between different CALIPSO cloud products and found that cloud fraction differences of 10-20% were not uncommon, with larger cloud

fractions at higher altitudes in the tropics when different thresholds and averaging were used. Very low clouds are also missed by OSIRIS, likely due to high aerosol and clouds above these altitudes, which masks the cloud signature. The bottom panel shows the spatial distribution of cloud cover above 6.5 km from the two datasets over the same period. Cloud distribution is very similar in both datasets, although OSIRIS again measures somewhat higher cloud fraction, particularly in the tropics where more sub-visual cirrus are expected.

5.4.3 Polar Stratospheric Clouds

Although the OSIRIS orbit precludes measurements from being taken at high latitudes for most of the winter, measurements in the spring may contain polar stratospheric clouds. As sulphate aerosols are often a primary component of these clouds, and they play an important role in ozone destruction, it is useful to flag PSCs separately from lower altitude ice and water clouds. To do this, PSCs are screened using the Chen *et al.* (2016) method with a threshold value of 0.12 with the additional constraint that the temperature at the tangent point must also be below 200K. Although this is slightly above the typical formation temperature it allows for some error in the ECMWF climatology and variation along the line of sight. Figure 5.11 shows the weekly averaged extinction between 60°S and 90°S before and after removal of PSCs. The final panel shows the fraction of measurements that have been flagged as containing PSCs. Just after OSIRIS regains coverage in the austral spring up to half of the measurements contain PSCs with essentially none remaining by the end of October. The exception to this is in 2015, when aerosol from the Calbuco Eruption in April 2015 produces PSCs well into November.

5.4.4 UTLS Improvements

Combined with the cloud removal, the improved sensitivity of incorporating additional wavelengths allows for the version 7 algorithm to retrieve at lower altitudes than previously. Version 5.07 did not attempt retrievals below 10 km, and has relied on various thresholds to determine lower limits depending on the use case. Version 5 of the OSIRIS data took a conservative approach and masked off any data below where the extinction exceeded approx-

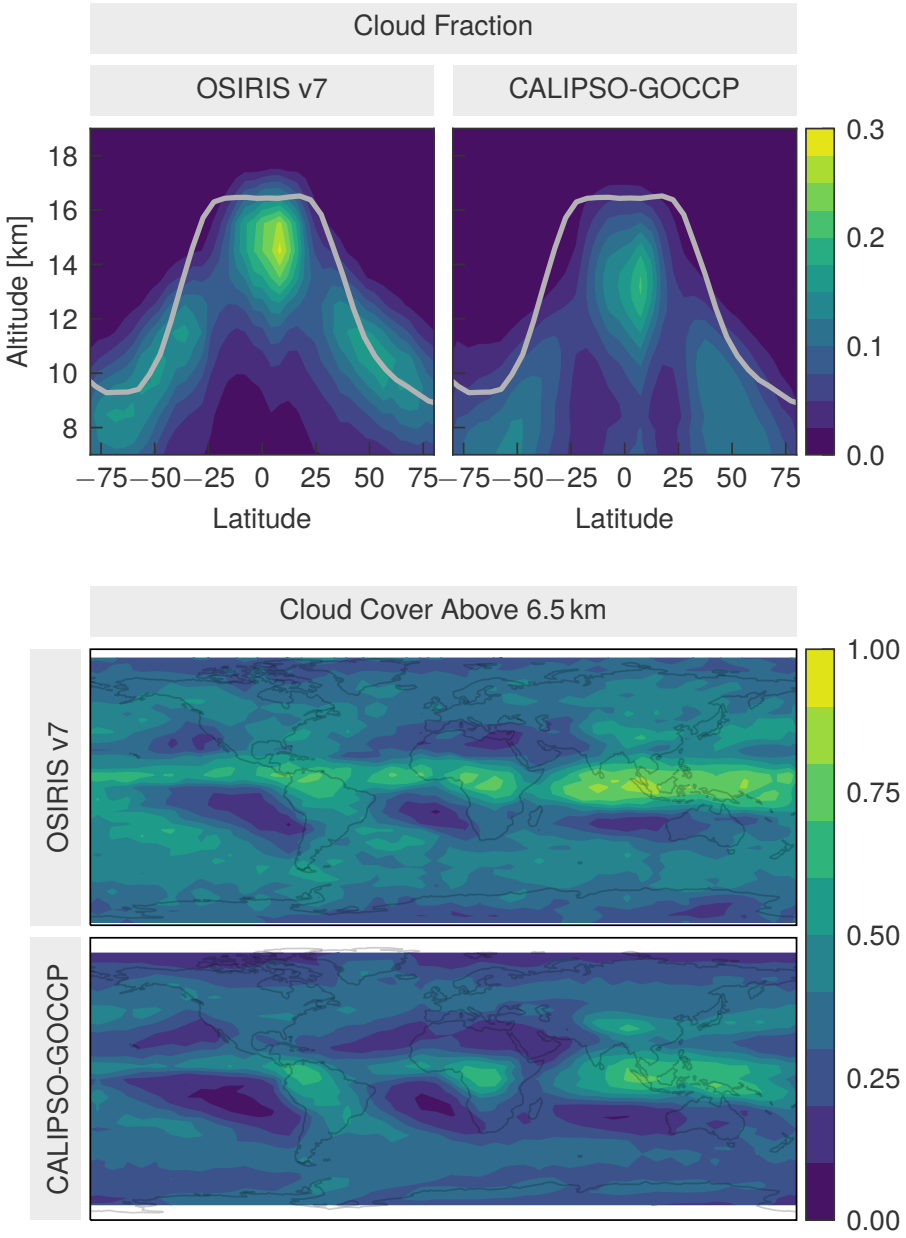

Figure 5.10: The top panels show the cloud fraction as a function of latitude from the OSIRIS version 7 (left) and CALIPSO-GOCCP datasets (right). The gray line indicates the mean tropopause altitude. The fractional cloud cover is shown in the bottom panel. All figures are computed from 2006 through 2017, the duration of the CALIPSO-GOCCP dataset.

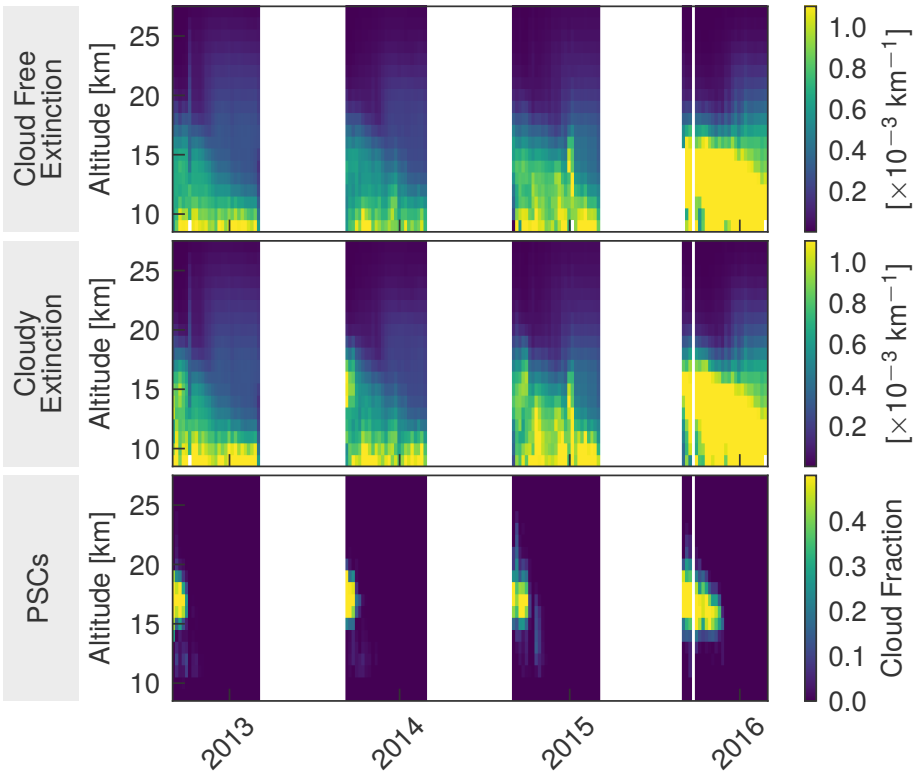

Figure 5.11: Top panel shows the weekly averaged cloud-free extinction between 60°S and 90°S. The middle panel shows the extinction before cloud screening. The bottom panel shows the fraction of measurements that have been flagged as containing PSCs.

imately $2.5 \times 10^{-3}\,\mathrm{km}^{-1}$. As noted in Fromm *et al.* (2014), this can cause apparent biases when comparing to records that include higher aerosol values. Other work such as Rieger *et al.* (2015) applied a much less conservative limit of $3 \times 10^{-2}\,\mathrm{km}^{-1}$ to help reduce these effects at the cost of including some clouds in the analysis. Version 7 does not limit the retrieval to above 10 km altitudes and consistently extends below the tropopause.

Figure 5.12 shows a comparison between version 5.07 and 7 products in the UTLS after the Sarychev eruption. Each panel shows the change in average extinction relative to May 2009, the month preceding the eruption. The v5.07 product is shown in the left column, and immediately after the Sarychev eruption a clear increase aerosol extinction is present above 50°N. However, data in the tropics below the tropopause is heavily contaminated with clouds, and the 10 km cutoff results in data missing even above the tropopause at higher latitudes, with virtually no indication of what is happening below the aerosol plume. The version 7 data

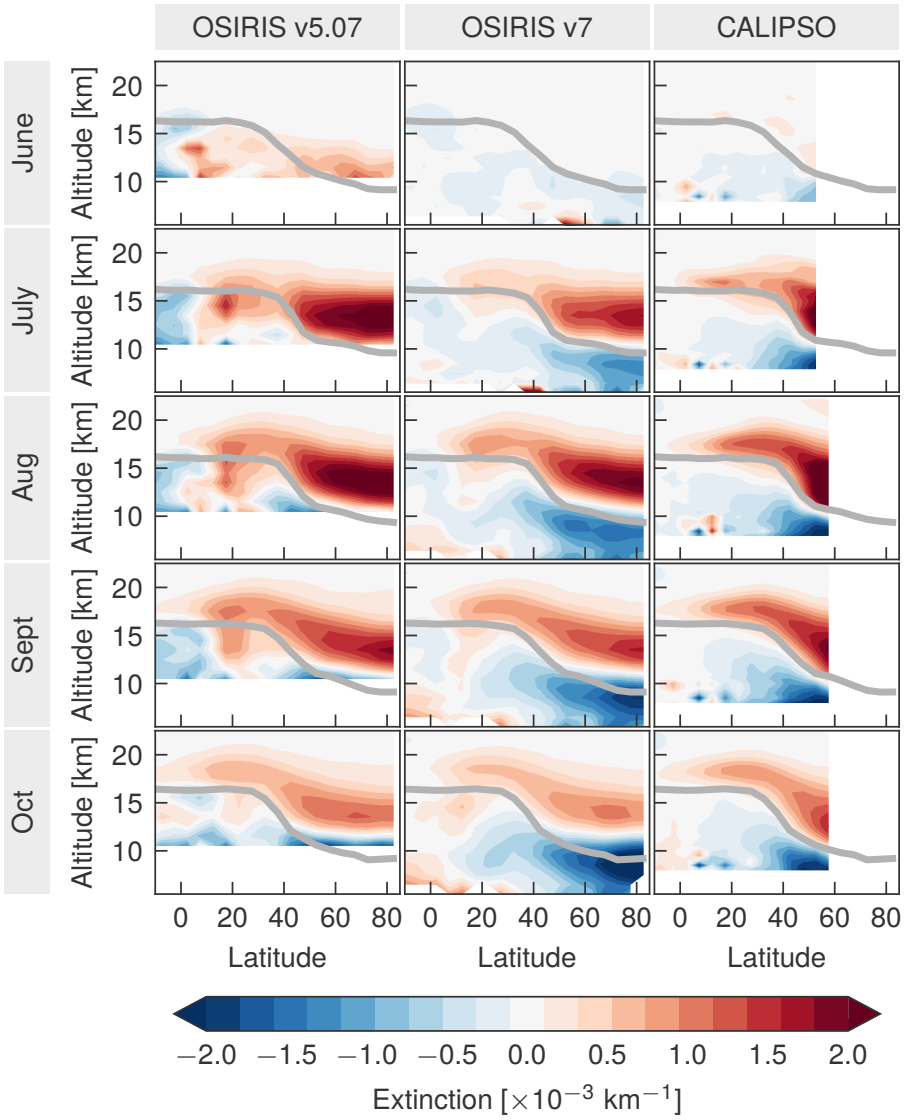

Figure 5.12: Comparisons of UTLS measurements after the Sarychev eruption in June 2009. Monthly averaged extinction is shown as the difference from May 2009 values. OSIRIS v5.07 measurements are shown in left column, version 7 in the center column, and CALIPSO-GloSSAC values in the right column. The gray line indicates the monthly mean tropopause altitude.

is shown in the center column and consistently extends down to 6.5 km altitudes. It shows a very similar evolution of the Sarychev plume above the tropopause, however also shows a clear decrease in aerosol levels in the troposphere outside of the tropics. CALIPSO data from the global space-based stratospheric aerosol climatology (GloSSAC) (Thomason *et al.*, 2018) is

shown in the far right column. CALIPSO backscatter at 532 nm has been converted to 750 nm extinction using a conversion factor of 30, consistent with the particle size used in the OSIRIS retrieval. The version 7 algorithm retrieves somewhat more variable extinction values in the tropical troposphere than CALIPSO. OSIRIS version 7 also retrieves somewhat lower aerosol values in the thickest part of the aerosol plume. This is likely an indication of some clouds remaining in the extinction product in the tropics, while some aerosol has been flagged as cloud at high extinction levels. Additionally, few extinction measurements exceed $0.01\,\mathrm{km}^{-1}$, due largely to limitations in the retrieval at large optical depths. Very large extinctions can be difficult to model, as assumptions about horizontal homogeneity and aerosol composition are likely less robust, and local minimums in the retrievals can lead to non-convergence. As only converged profiles are reported in the final product, events with extinctions near or exceeding $0.01\,\mathrm{km}^{-1}$ will be underestimated when looking at averaged data. Despite the difficulty of the measurements, both instruments present a consistent picture of the UTLS region after a moderate volcanic eruption, with aerosol levels increasing rapidly above the tropopause, while altitudes below remain considerably cleaner than pre-eruption.

5.5 Validation

5.5.1 SAGE Comparisons

SAGE II was launched in 1984 on board the Earth Radiation Budget Satellite and continued operation until 2005. It provided near global sampling of stratospheric aerosol extinction approximately every month at wavelengths of 386, 452, 525 and 1020 nm. For this study the SAGE II version 7 aerosol extinction (Damadeo *et al.,* 2013) is used, and converted to 750 nm by interpolating the 525 nm and 1020 nm channels in logarithmic space. SAGE II data has been cloud cleared using the provided cloud flag.

SAGE III was launched on the Meteor-3M (M3M) platform in 2001 into a polar orbit that provided coverage of the mid-to-high latitudes. SAGE III measured extinction at a range of wavelengths between 384 and 1543 nm until 2006. A second SAGE III instrument was launched in February 2017 and placed on the International Space Station (ISS). SAGE

III/ISS began operations in June 2017 with aerosol extinction processed using essentially the same algorithm as SAGE III/M3M. For this work the SAGE III/M3M comparisons use the version 4 extinction product at 755 nm (Thomason *et al.,* 2010). As no cloud flag is provided with the SAGE III data it has not been cloud cleared. Using the 520 and 1020 nm channels from SAGE III to interpolate to 750 nm, as was done with the SAGE II data, generally decreases the SAGE III extinction values by a few percent but does not meaningfully impact the comparisons, either in magnitude or standard deviation.

Scans are considered to be coincident if they are within ±2° latitude, ±10° longitude, and ±24 hours. Each line of sight through the limb spans approximately 2° latitude, and an additional 1-4° latitude is spanned as the satellite orbits during the acquisition of a vertical profile, making tighter latitudinal criteria of little benefit. The median percent differences between OSIRIS version 7 and each of the SAGE instruments are shown in Figure 5.13 at three latitude bands. The solid line indicates the median, while the shaded regions indicate different percentiles of the data, as shown in the figure legend. The small numbers at the left of each panel indicate the number of coincident measurements at that altitude. For reference, the median version 5.07 differences are also shown in red.

Agreement between OSIRIS and the various SAGE instruments is generally very good, with biases of less than 10% for most regions above the tropopause. The exception to this is at high altitudes where OSIRIS has low bias with respect to SAGE, and is thought to be due to sensitivity to stray light and non-zero aerosol in the OSIRIS normalization altitudes (Rieger *et al.,* 2018). For the SAGE II and SAGE III/M3M comparisons there is little difference between the OSIRIS version 5.07 and 7 products, as the mean extinction does not change substantially between products when averaged over multiple years. However, the SAGE III/ISS comparison covers only a 6 month time span, limiting the range of OSIRIS scattering angles included in the comparison, and here improvements over version 5.07 are seen in the mid and high latitudes. Differences between SAGE III/ISS and OSIRIS in the tropics is currently under investigation.

In the future, moving to comparisons on equivalent latitude may be beneficial, as sampling in and outside of the polar vortex is evident in the SAGE III/ISS comparisons in the 30° to 90°S bin. The 90^{th} percentile shows vary large differences, a likely indicator that SAGE

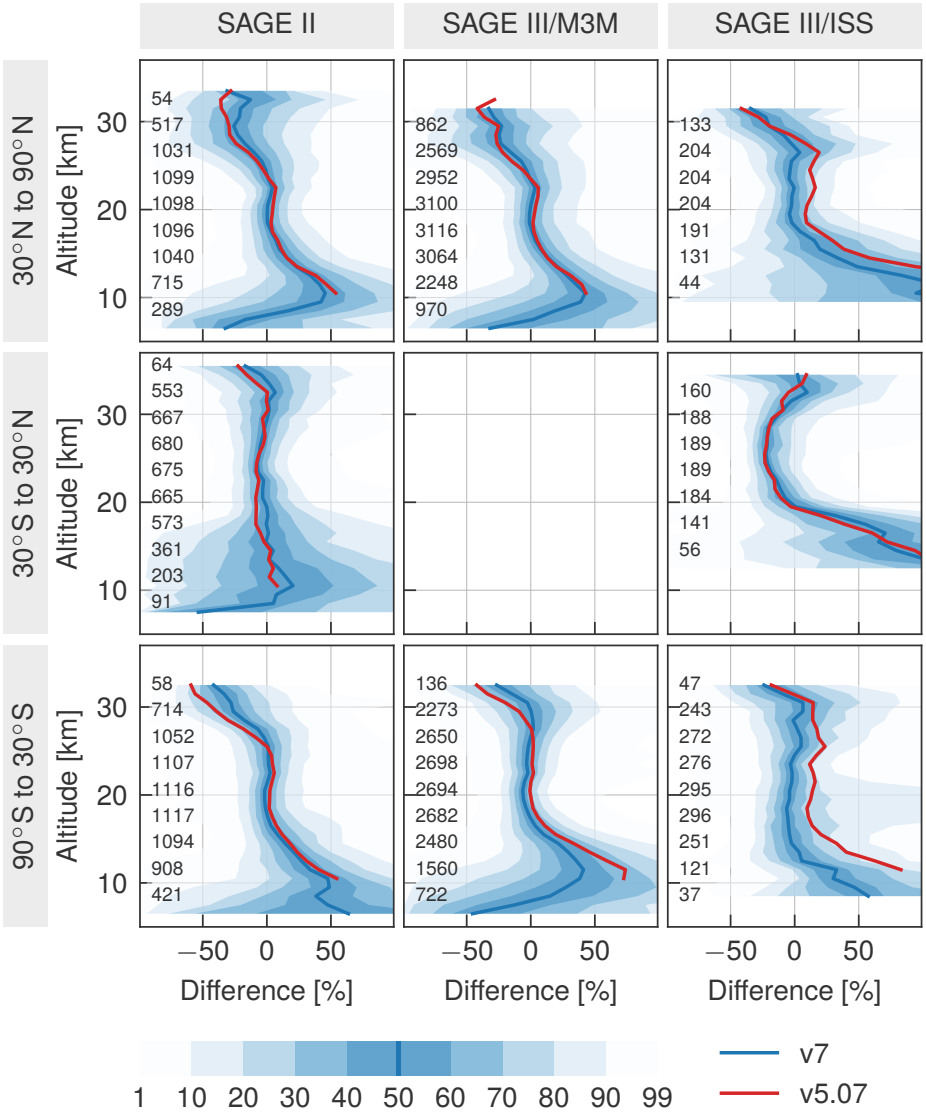

Figure 5.13: Coincident comparison of OSIRIS version 7 with SAGE II, SAGE III, and SAGE III-ISS. Differences are computed as (OSIRIS - SAGE) / SAGE × 100%. Solid lines show the median difference and shaded regions show various percentiles as indicated by the color bar. Version 7 results are shown in blue with version 5.07 comparisons shown in red as a reference. The numbers in the left of the panels indicate the number of coincident measurements at each altitude.

III/ISS is sampling inside of the relatively clean vortex, and OSIRIS outside. However, for 80% of the data, differences are within ±25%, indicating that when both instruments are sampling similar air masses agreement is generally very good.

5.5.2 Level 3 Comparisons

Although clouds and reduced sensitivity in the UTLS can make direct comparisons of averaged data difficult, the creation and validation of such climatologies is still an important task as they are often used both in model comparisons, and as model inputs. Figure 5.14 shows OSIRIS data in monthly averages from 10°S to 10°N at three altitude levels. The shaded region indicates one standard deviation of the monthly mean values. Also plotted are the SAGE II data, averaged in the same way, as well as the CALIPSO extinction from GloSSAC, again converted using a backscatter to extinction factor of 30. This factor provides good agreement for most altitudes in the tropics, however at higher latitudes, and particularly at altitudes above 25 km, causes CALIPSO to overestimate OSIRIS by up to a factor of two. This may be an indicator of smaller particles at these higher extra-tropical altitudes. A lognormal distribution with a width of 1.6 and median radius of 50 nm would provide a Lidar conversion factor of 15, instead of the 30 used here, and greatly improve agreement in these regions (not shown). CALIPSO and SAGE II are displayed here as they, along with OSIRIS, provide the three main datasets used to construct GloSSAC. Additionally, neither SAGE II nor CALIPSO are limb scatter datasets, minimizing seasonal biases due to particle size assumptions, providing more independent data for time-series comparisons. For reference, the version 5.07 data is also shown. Altitudes near 20 km remain largely unchanged between versions and both are in excellent agreement with both SAGE II and CALIPSO. The seasonal cycle in near 25 km has been greatly reduced in version 7, and OSIRIS now agrees much better with the CALIPSO extinction. Altitudes near 30 km agree very well for both versions of OSIRIS, however large spikes in the version 5.07 data at the beginning of 2005, 2009, and 2014 have been reduced and now agree much better with CALIPSO. The cause of this is not currently known, but happens primarily when the quasi-biennial oscillation is transitioning from Easterly to Westerly, so may be an indication of changing particle size coupled with the seasonal cycle in the OSIRIS scattering angle.

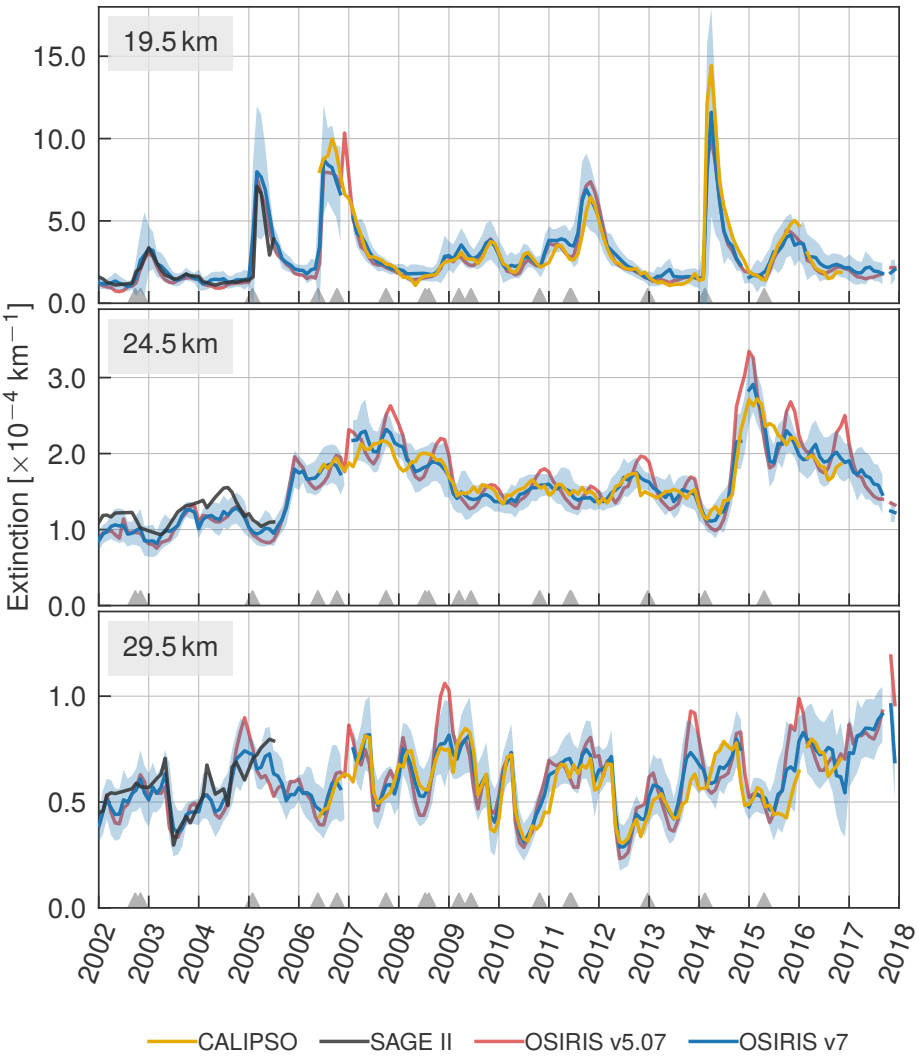

Figure 5.14: Comparison of the monthly averaged version 7 OSIRIS aerosol record in the tropics compared to SAGE II, CALIPSO, and the OSIRIS version 5.07 record. The shaded region indicates one standard deviation of the monthly mean values. Grey triangles indicate the time of the largest volcanic eruptions during this time period.

5.6 Conclusions

A new version of the OSIRIS aerosol extinction product has been processed using a multi-wavelength retrieval. The data, as well as additional information on file formats, usage and

processing updates can be found at `https://arg.usask.ca/docs/osiris_v7/`. The new algorithm shows improved results when compared to previous versions as well as CALIPSO, SAGE II and SAGE III instruments. The dependence on the measurement geometry has been reduced when comparing measurements at different scattering angles, although some discrepancies remain just above the tropopause in the northern hemisphere, and the cause of this remains under investigation. Use of multiple wavelengths allows for retrievals at lower altitudes then previously, and agreement with CALIPSO measurements is promising even during enhanced aerosol conditions such as after the Sarychev eruption. However, with a limited wavelength range cloud clearing remains an imperfect exercise, and saturation of the retrieval immediately after eruptions may still result in low biases if zonal and temporal averages are used for comparisons.

Chapter 6

Conclusions and Outlook

The interpretation of aerosol quantities from remote sensing measurements is far from straight-forward, and requires many assumptions with careful consideration of the inversion techniques used to minimize errors. Despite the inherent difficulties, satellite measurements have greatly expanded the knowledge of stratospheric aerosols and allowed for more accurate simulations of Earth's climate and improved understanding of chemical and radiative impacts. This work has helped merge two satellite records to produce a continuous aerosol dataset spanning over 35 years that is currently being used by the climate modelling community for both model input and validation. While a substantial improvement over previous efforts, the merged record had seasonal biases and deficiencies in the UTLS due to limitations of the OSIRIS record. Careful analysis of limb scattering retrieval methods yielded an improved algorithm that was applied to the OSIRIS measurements and a more robust aerosol product was published that provided reduced sensitivity to particle size assumptions, increased measurements at lower altitudes and improved cloud screening, allowing for greater use of the data in the UTLS region. The updated OSIRIS product is currently being incorporated by NASA into the next version of the Global Space-based Stratospheric Aerosol Climatology for use in climate models.

While this work has improved the OSIRIS aerosol product and the resulting merged climatologies, there are several avenues for further improvement moving forward. A major source of error in the retrievals is the assumed aerosol loading at altitudes above the current retrieval altitudes, and improvements here could help to reduce systematic errors. Inclusion of shorter wavelengths into the retrieval, which are more sensitive to aerosols but not yet saturated by the Rayleigh signal may help at these higher altitudes. Additionally, while this work intentionally left the assumed particle size unchanged as to separate changes to

the a priori particle size from the algorithm modifications, future versions may benefit from updates to the particle size assumption from new balloon-borne data such as incorporating altitude dependent profiles. Expanding the application of the this multi-wavelength algorithms to other limb scatter datasets such as OMPS-LP could help improve the aerosol record into the future, especially with planned launches of the JPSS missions, successors to OMPS-LP.

In addition to retrieval improvements, there remains many additional open questions in the field of stratospheric aerosol measurements. Particle size is an important factor when computing radiative effects and surface area density for ozone loss, and very little global data exists about this quantity. This is due primarily to the broad spectral signature of aerosol particles that has little size information in the optical and near infrared wavelength ranges typically measured. Uncertainty in this quantity impacts the larger understanding of climate in two ways. First, the retrievals from limb scattering and lidar measurements are biased by these a priori assumptions, leading to time and latitude dependent biases in extinction records. Second, when using the retrieved extinction values climate models must assume some particle size distribution, and errors here lead to errors in the climate. In situ measurements currently provide the best information on this topic, but are limited in scope, and often do not measure particles in the 50 to 100 nm range that are important in improving size distribution knowledge. Future measurement platforms that can resolve particle size on a global scale would greatly reduce the uncertainties in the radiative assumptions used in both extinction retrievals and climate models.

While particle size remains an important question, it is likely a secondary effect in terms of radiative impact. Large uncertainty of extinction itself remains in the UTLS region, where cloud contamination and poor measurement sensitivity make retrievals difficult. In the last 20 years the stratospheric aerosol layer has been dominated by small volcanic eruptions that reach only into the upper troposphere or lower stratosphere where measurement uncertainty is largest. Coupled with the measurement difficulty in this region is the uncertainty in composition, with high altitude airplane campaigns noting high levels of organics in addition to sulfur compounds, complicating the chemical reactions that affect particle lifetime and optical properties, further increasing radiative forcing uncertainty. Substantial advancement to stratospheric aerosol understanding will require improvements to these UTLS measurements

using a range of instruments, as no single, current measurement system is likely capable of making these improvements. Occultation measurements provide excellent extinction measurements but poor sampling, and limb scattering measurements, while improved in this work, still suffer from cloud biases and saturation at low altitudes. Space based lidars with polarization information may provide the best opportunities in the UTLS due largely to good cloud discrimination, but signal to noise remains a challenge and few such systems are planned for the future.

Ultimately, improving quantification of the climate impacts of stratospheric aerosol will rely heavily on both new measurement systems and the ability of models to capture secondary effects. While radiative forcing estimates are subject to uncertainties in observed extinction, the process is relatively well understood. Conversely, cloud-aerosol interactions remain a primarily parameterized affair with large variability between models. More uncertain still is the ability to predict the future state of stratospheric aerosols. While the random nature of volcanic eruptions is a prime driver of this uncertainty, modelling of aerosol microphysics remains a difficult task reliant on many assumptions and parameterizations. Large scale modelling studies such as ISA-MIP (Timmreck *et al.,* 2018) aim to investigate these inter-model differences, however measurements of cloud-aerosol interactions remain limited (Fan *et al.,* 2016) making direct validation difficult. Overall, however, while important questions remain in regards to precise stratospheric aerosol levels, optical properties, and indirect effects, research has made remarkable strides in these areas over the last decade with substantial reduction in the resulting climate uncertainties.

Bibliography

1. Abdalati, W., Zwally, H. J., Bindschadler, R., *et al.* The ICESat-2 laser altimetry mission. *Proceedings of the IEEE* **98,** 735–751 (2010).

2. Ammann, C. M., Meehl, G. A., Washington, W. M. & Zender, C. S. A monthly and latitudinally varying volcanic forcing dataset in simulations of 20th century climate. *Geophysical Research Letters* **30** (2003).

3. Andersson, S. M., Martinsson, B. G., Vernier, J.-P., *et al.* Significant radiative impact of volcanic aerosol in the lowermost stratosphere. *Nature communications* **6,** 7692 (2015).

4. Ansmann, A., Wandinger, U., Le Rille, O., Lajas, D. & Straume, A. G. Particle backscatter and extinction profiling with the spaceborne high-spectral-resolution Doppler lidar ALADIN: methodology and simulations. *Applied optics* **46,** 6606–6622 (2007).

5. Barcilon, T. V. On Chahine's relaxation method for the radiative transfer equation. *Journal of the Atmospheric Sciences* **32,** 1626–1630 (1975).

6. Barnes, J. E. & Hofmann, D. J. Lidar measurements of stratospheric aerosol over Mauna Loa Observatory. *Geophysical Research Letters* **24,** 1923–1926 (1997).

7. Barth, C., Rusch, D., Thomas, R., *et al.* Solar mesosphere explorer: Scientific objectives and results. *Geophysical research letters* **10,** 237–240 (1983).

8. Boucher, O., Randall, D, Artaxo, P, *et al.* in *Climate Change 2013: The Physical Science Basis. Contribution of Working Group I to the Fifth Assessment Report of the Intergovernmental Panel on Climate Change* (eds Stocker, T., Qin, D, Plattner, G.-K., *et al.*) (Cambridge University Press, Cambridge, United Kingdom and New York, NY, USA, 2013).

9. Bourassa, A. E., Rieger, L. A., Lloyd, N. D. & Degenstein, D. A. "Odin-OSIRIS stratospheric aerosol data product and SAGE III intercomparison". *Atmospheric Chemistry and Physics* **12,** 605–614 (2012).

10. Bourassa, A. E., Degenstein, D. A., Gattinger, R. L. & Llewellyn, E. J. Stratospheric aerosol retrieval with optical spectrograph and infrared imaging system limb scatter measurements. *Journal of Geophysical Research: Atmospheres* **112.** ISSN: 2156-2202. doi:10.1029/2006JD008079 (2007).

11. Bourassa, A. E., Roth, C. Z., Zawada, D. J., *et al.* Drift-corrected Odin-OSIRIS ozone product: algorithm and updated stratospheric ozone trends. *Atmospheric Measurement Techniques* **11,** 489 (2018).

12. Bourassa, A. E., Robock, A., Randel, W. J., *et al.* Large volcanic aerosol load in the stratosphere linked to Asian monsoon transport. *Science* **337,** 78–81 (2012).

13. Bourassa, A., Degenstein, D., Elash, B. & Llewellyn, E. Evolution of the stratospheric aerosol enhancement following the eruptions of Okmok and Kasatochi: Odin-OSIRIS measurements. *Journal of Geophysical Research: Atmospheres* **115** (2010).

14. Bourassa, A., Degenstein, D. & Llewellyn, E. SASKTRAN: A spherical geometry radiative transfer code for efficient estimation of limb scattered sunlight. *Journal of Quantitative Spectroscopy and Radiative Transfer* **109,** 52 –73. ISSN: 0022-4073 (2008).

15. Bovensmann, H, Burrows, J., Buchwitz, M, *et al.* SCIAMACHY: Mission objectives and measurement modes. *Journal of the Atmospheric Sciences* **56,** 127–150 (1999).

16. Brock, C., Hamill, P, Wilson, J., Jonsson, H. & Chan, K. Particle formation in the upper tropical troposphere: A source of nuclei for the stratospheric aerosol. *Science* **270,** 1650–1653 (1995).

17. Burrows, J., Hölzle, E, Goede, A., Visser, H & Fricke, W. SCIAMACHY-Scanning imaging absorption spectrometer for atmospheric chartography. *Acta Astronautica* **35,** 445–451 (1995).

18. Byrne, C. L. Iterative image reconstruction algorithms based on cross-entropy minimization. *IEEE Transactions on image processing* **2,** 96–103 (1993).

19. Canty, T, Mascioli, N., Smarte, M. & Salawitch, R. An empirical model of global climate–Part 1: A critical evaluation of volcanic cooling. *Atmospheric Chemistry and Physics* **13,** 3997–4031 (2013).

20. Carslaw, K. S., Luo, B. & Peter, T. An analytic expression for the composition of aqueous HNO_3-H_2SO_4 stratospheric aerosols including gas phase removal of HNO_3. *Geophys. Res. Lett.* **22,** 1877–1880 (1995).

21. Chagnon, C. W. & Junge, C. E. The vertical distribution of sub-micron particles in the stratosphere. *Journal of Meteorology* **18,** 746–752 (1961).

22. Chahine, M. I. A general relaxation method for inverse solution of the full radiative transfer equation. *Journal of the Atmospheric Sciences* **29,** 741–747 (1972).

23. Chahine, M. T. Inverse problems in radiative transfer: Determination of atmospheric parameters. *Journal of the Atmospheric Sciences* **27,** 960–967 (1970).

24. Chandrasekhar, S. *Radiative Transfer* (Dover, New York, 1960).

25. Chen, Z., Bhartia, P. K., Loughman, R. & Colarco, P. Impact of aerosol size distribution on extinction and spectral dependence of radiances measured by the OMPS Limb profiler instrument. *Atmospheric Measurement Techniques Discussions* **2018,** 1–18 (2018).

26. Chen, Z., DeLand, M. & Bhartia, P. K. A new algorithm for detecting cloud height using OMPS/LP measurements. *Atmospheric Measurement Techniques* **9,** 1239–1246 (2016).

27. Chepfer, H, Cesana, G, Winker, D, *et al.* Comparison of two different cloud climatologies derived from CALIOP-attenuated backscattered measurements (Level 1): The CALIPSO-ST and the CALIPSO-GOCCP. *Journal of Atmospheric and Oceanic Technology* **30,** 725–744 (2013).

28. Chepfer, H, Bony, S, Winker, D, *et al.* The GCM-Oriented CALIPSO Cloud Product (CALIPSO-GOCCP). *Journal of Geophysical Research: Atmospheres* **115** (2010).

29. Chu, W. P., McCormick, M. P., Lenoble, J., Brogniez, C. & Pruvost, P. SAGE II inversion algorithm. *Journal of Geophysical Research: Atmospheres* **94,** 8339–8351. ISSN: 2156-2202 (1989).

30. Chu, W. P. Convergence of Chahine's nonlinear relaxation inversion method used for limb viewing remote sensing. *Applied optics* **24,** 445–447 (1985).

31. Curtius, J., Weigel, R., Vössing, H.-J., *et al.* Observations of meteoric material and implications for aerosol nucleation in the winter Arctic lower stratosphere derived from in situ particle measurements. *Atmospheric chemistry and physics* **5,** 3053–3069 (2005).

32. Damadeo, R. P., Zawodny, J. M., Thomason, L. W. & Iyer, N. SAGE version 7.0 algorithm: application to SAGE II. *Atmospheric Measurement Techniques* **6,** 3539–3561 (2013).

33. Dee, D. P., Uppala, S., Simmons, A., *et al.* The ERA-Interim reanalysis: Configuration and performance of the data assimilation system. *Quarterly Journal of the royal meteorological society* **137,** 553–597 (2011).

34. Degenstein, D., Bourassa, A., Roth, C. & Llewellyn, E. Limb scatter ozone retrieval from 10 to 60 km using a multiplicative algebraic reconstruction technique. *Atmospheric Chemistry and Physics* **9,** 6521–6529 (2009).

35. Degenstein, D. A., Llewellyn, E. J. & Lloyd, N. D. Volume emission rate tomography from a satellite platform. *Applied optics* **42,** 1441–1450 (2003).

36. Dempster, A. P., Laird, N. M. & Rubin, D. B. Maximum likelihood from incomplete data via the EM algorithm. *Journal of the royal statistical society. Series B (methodological),* 1–38 (1977).

37. Deshler, T., Hervig, M. E., Hofmann, D. J., Rosen, J. M. & Liley, J. B. Thirty years of in situ stratospheric aerosol size distribution measurements from Laramie, Wyoming (41°N), using balloon-borne instruments. *J. Geophys. Res.* **108,** 4167 (Mar. 2003).

38. Driscoll, S., Bozzo, A., Gray, L. J., Robock, A. & Stenchikov, G. Coupled Model Intercomparison Project 5 (CMIP5) simulations of climate following volcanic eruptions. *Journal of Geophysical Research: Atmospheres (1984–2012)* **117** (2012).

39. Eichmann, K.-U., Lelli, L., von Savigny, C., Sembhi, H. & Burrows, J. P. Global cloud top height retrieval using SCIAMACHY limb spectra: model studies and first results. *Atmospheric Measurement Techniques* **9,** 793 (2016).

40. England, M. H., McGregor, S., Spence, P., *et al.* Recent intensification of wind-driven circulation in the Pacific and the ongoing warming hiatus. *Nature Climate Change* **4,** 222 (2014).

41. Eparvier, F., Rusch, D., Clancy, R. & Thomas, G. Solar Mesosphere Explorer satellite measurements of El Chichón stratospheric aerosols: 2. Aerosol mass and size parameters. *Journal of Geophysical Research: Atmospheres* **99,** 20533–20544 (1994).

42. Ernst, F., von Savigny, C., Rozanov, A., *et al.* Global stratospheric aerosol extinction profile retrievals from SCIAMACHY limb-scatter observations. *Atmospheric Measurement Techniques Discussions* **5,** 5993–6035 (2012).

43. Fan, J., Wang, Y., Rosenfeld, D. & Liu, X. Review of aerosol–cloud interactions: Mechanisms, significance, and challenges. *Journal of the Atmospheric Sciences* **73,** 4221–4252 (2016).

44. Fiocco, G & Grams, G. Observations of the aerosol layer at 20 km by optical radar. *Journal of the Atmospheric Sciences* **21,** 323–324 (1964).

45. Flamant, P., Cuesta, J., Denneulin, M.-L., Dabas, A. & Huber, D. ADM-Aeolus retrieval algorithms for aerosol and cloud products. *Tellus A: Dynamic Meteorology and Oceanography* **60,** 273–286 (2008).

46. Flynn, L. E., Seftor, C. J., Larsen, J. C. & Xu, P. in *Earth science satellite remote sensing* 279–296 (Springer, 2006).

47. Fromm, M., Kablick, G, Nedoluha, G, *et al.* Correcting the record of volcanic stratospheric aerosol impact: Nabro and Sarychev Peak. *Journal of Geophysical Research: Atmospheres* **119** (2014).

48. Fueglistaler, S, Dessler, A., Dunkerton, T., *et al.* Tropical tropopause layer. *Reviews of Geophysics* **47** (2009).

49. Fussen, D., Dekemper, E., Errera, Q., *et al.* The ALTIUS mission. *Atmos Meas Tech Discuss* (2016).

50. Fyfe, J., Salzen, K, Cole, J., Gillett, N. & Vernier, J.-P. Surface response to stratospheric aerosol changes in a coupled atmosphere–ocean model. *Geophysical Research Letters* **40,** 584–588 (2013a).

51. Fyfe, J. C., Gillett, N. P. & Zwiers, F. W. Overestimated global warming over the past 20 years. *Nature Climate Change* **3,** 767 (2013).

52. Goldberg, M. D., Kilcoyne, H., Cikanek, H. & Mehta, A. Joint Polar Satellite System: The United States next generation civilian polar-orbiting environmental satellite system. *Journal of Geophysical Research: Atmospheres* **118,** 13–463 (2013b).

53. Gordley, L. L., Hervig, M. E., Fish, C., *et al.* The solar occultation for ice experiment. *Journal of Atmospheric and Solar-Terrestrial Physics* **71,** 300–315 (2009).

54. Gordon, R., Bender, R. & Herman, G. T. Algebraic reconstruction techniques (ART) for three-dimensional electron microscopy and X-ray photography. *Journal of theoretical Biology* **29,** 471–481 (1970).

55. Gorkavyi, N., Rault, D., Newman, P., Silva, A. & Dudorov, A. New stratospheric dust belt due to the Chelyabinsk bolide. *Geophysical Research Letters* **40,** 4728–4733 (2013).

56. Govindasamy, B, Caldeira, K. & Duffy, P. Geoengineering Earth's radiation balance to mitigate climate change from a quadrupling of CO2. *Global and Planetary Change* **37,** 157–168 (2003).

57. Goyer, G. G. & Watson, R. The laser and its application to meteorology. *Bulletin of the American Meteorological Society* **44,** 564–570 (1963).

58. Granqvist, C. G. & Buhrman, R. A. Ultrafine metal particles. *J. Appl. Phys.* **47,** 2200–2219 (May 1976).

59. Gu, L., Baldocchi, D. D., Wofsy, S. C., *et al.* Response of a deciduous forest to the Mount Pinatubo eruption: Enhanced photosynthesis. *Science* **299,** 2035–2038 (2003).

60. Guo, S., Bluth, G. J., Rose, W. I., Watson, I. M. & Prata, A. Re-evaluation of SO2 release of the 15 June 1991 Pinatubo eruption using ultraviolet and infrared satellite sensors. *Geochemistry, Geophysics, Geosystems* **5** (2004).

61. Haarig, M., Ansmann, A., Baars, H., *et al.* Depolarization and lidar ratios at 355, 532, and 1064 nm and microphysical properties of aged tropospheric and stratospheric Canadian wildfire smoke. *Atmospheric Chemistry and Physics* **18,** 11847–11861 (2018).

62. Haerter, J. O., Roeckner, E., Tomassini, L. & von Storch, J.-S. Parametric uncertainty effects on aerosol radiative forcing. *Geophysical Research Letters* **36.** L15707, n/a–n/a. ISSN: 1944-8007 (2009).

63. Hamill, P., Turco, R., Kiang, C., Toon, O. & Whitten, R. An analysis of various nucleation mechanisms for sulfate particles in the stratosphere. *Journal of Aerosol Science* **13,** 561–585 (1982).

64. Hamill, P., Toon, O. & Kiang, C. Microphysical processes affecting stratospheric aerosol particles. *Journal of the Atmospheric Sciences* **34,** 1104–1119 (1977).

65. Hamill, P., Jensen, E. J., Russell, P. & Bauman, J. J. The life cycle of stratospheric aerosol particles. *Bulletin of the American Meteorological Society* **78,** 1395–1410 (1997).

66. Haywood, J. M., Jones, A. & Jones, G. S. The impact of volcanic eruptions in the period 2000–2013 on global mean temperature trends evaluated in the HadGEM2-ES climate model. *Atmospheric Science Letters* **15,** 92–96 (2014).

67. Heckendorn, P., Weisenstein, D., Fueglistaler, S., *et al.* The impact of geoengineering aerosols on stratospheric temperature and ozone. *Environmental Research Letters* **4,** 045108 (2009).

68. Hervig, M. E., Brooke, J. S., Feng, W., Bardeen, C. G. & Plane, J. Constraints on meteoric smoke composition and meteoric influx using SOFIE observations with models. *Journal of Geophysical Research: Atmospheres* **122** (2017).

69. Hervig, M. E., Stevens, M. H., Gordley, L. L., *et al.* Relationships between polar mesospheric clouds, temperature, and water vapor from Solar Occultation for Ice Ex-

periment (SOFIE) observations. *Journal of Geophysical Research: Atmospheres* **114** (2009).

70. Hess, M, Koepke, P & Schult, I. Optical properties of aerosols and clouds: The software package OPAC. *Bulletin of the American meteorological society* **79,** 831–844 (1998).

71. Hofmann, D., Barnes, J., O'Neill, M., Trudeau, M. & Neely, R. Increase in background stratospheric aerosol observed with lidar at Mauna Loa Observatory and Boulder, Colorado. *Geophys. Res. Lett.* **36,** L15808 (Aug. 2009).

72. Holben, B. N., Eck, T. F., Slutsker, I., *et al.* AERONET—A federated instrument network and data archive for aerosol characterization. *Remote sensing of environment* **66,** 1–16 (1998).

73. Holton, J. R., Haynes, P. H., McIntyre, M. E., *et al.* Stratosphere-troposphere exchange. *Rev. Geophys.* **33,** 403–439 (Nov. 1995).

74. Illingworth, A. J., Barker, H., Beljaars, A, *et al.* The EarthCARE satellite: The next step forward in global measurements of clouds, aerosols, precipitation, and radiation. *Bulletin of the American Meteorological Society* **96,** 1311–1332 (2015).

75. Junge, C. E., Chagnon, C. W. & Manson, J. E. Stratospheric aerosols. *Journal of Meteorology* **18,** 81–108 (1961).

76. Kaczmarz, S. 1379 Angenäherte Auflösung von Systemen linearer Gleichungen. *Bull. Int. Acad. Pol. Sci. Lett. Class. Sci. Math. Nat* **A35,** 355–7 (1937).

77. Kalnay, E., Kanamitsu, M., Kistler, R., *et al.* The NCEP/NCAR 40-year reanalysis project. *Bulletin of the American meteorological Society* **77,** 437–471 (1996).

78. Kent, G., Winker, D., Osborn, M. & Skeens, K. A model for the separation of cloud and aerosol in SAGE II occultation data. *Journal of Geophysical Research: Atmospheres* **98,** 20725–20735 (1993).

79. Khaykin, S. M., Godin-Beekmann, S., Keckhut, P., *et al.* Variability and evolution of the midlatitude stratospheric aerosol budget from 22 years of ground-based lidar and satellite observations. *Atmospheric Chemistry and Physics* **17,** 1829–1845 (2017).

80. Kiehl, J. T. & Briegleb, B. P. The relative roles of sulfate aerosols and greenhouse gases in climate forcing. *Science* **260,** 311–314 (Apr. 1993).

81. Kiss, L. B., Söderlund, J., Niklasson, G. A. & Granqvist, C. G. New approach to the origin of lognormal size distributions of nanoparticles. *Nanotechnology* **10,** 25–28 (Mar. 1999).

82. Kremser, S., Thomason, L. W., Hobe, M., *et al.* Stratospheric aerosol observations, processes, and impact on climate. *Reviews of Geophysics* (2016).

83. Kuebbeler, M., Lohmann, U. & Feichter, J. Effects of stratospheric sulfate aerosol geo-engineering on cirrus clouds. *Geophysical Research Letters* **39** (2012).

84. Kyrölä, E., Tamminen, J, Leppelmeier, G., *et al.* GOMOS on Envisat: An overview. *Advances in Space Research* **33,** 1020–1028 (2004).

85. Lacis, A., Hansen, J. & Sato, M. Climate forcing by stratospheric aerosols. *Geophys. Res. Lett.* **19,** 1607–1610 (1992).

86. Landweber, L. An iteration formula for Fredholm integral equations of the first kind. *American journal of mathematics* **73,** 615–624 (1951).

87. Levenberg, K. A method for the solution of certain non-linear problems in least squares. *Quarterly of applied mathematics* **2,** 164–168 (1944).

88. Liebing, P. *New Limb Cloud Detection Algorithm Theoretical Basis Document* 2016.

89. Llewellyn, E. J., Lloyd, N. D., Degenstein, D. A., *et al.* The OSIRIS instrument on the Odin spacecraft. *Canadian Journal of Physics* **82,** 411–422 (2004).

90. Lohmann, U. & Feichter, J. Global indirect aerosol effects: a review. *Atmospheric Chemistry and Physics* **5,** 715–737 (2005).

91. Loughman, R., Bhartia, P. K., Chen, Z., *et al.* The Ozone Mapping and Profiler Suite (OMPS) Limb Profiler (LP) Version 1 aerosol extinction retrieval algorithm: theoretical basis. *Atmospheric Measurement Techniques* **11,** 2633–2651 (2018).

92. Malinina, E., Rozanov, A., Rozanov, V., *et al.* Aerosol particle size distribution in the stratosphere retrieved from SCIAMACHY limb measurements. *Atmospheric Measurement Techniques* **11,** 2085 (2018).

93. Marquardt, D. W. An algorithm for least-squares estimation of nonlinear parameters. *Journal of the society for Industrial and Applied Mathematics* **11,** 431–441 (1963).

94. McCormick, M. P., Thomason, L. W. & Trepte, C. R. Atmospheric effects of the Mt Pinatubo eruption. *Nature* **373,** 399–404 (Feb. 1995).

95. McCormick, M. P., Chu, W. P., McMaster, L. R., *et al.* Satellite studies of the stratospheric aerosol. *Bull. Am. Meterol. Soc.* **60,** 1038–1046 (Sept. 1979).

96. McGill, M. J., Yorks, J. E., Scott, V. S., Kupchock, A. W. & Selmer, P. A. *The Cloud-Aerosol Transport System (CATS): A technology demonstration on the International Space Station* in *Lidar Remote Sensing for Environmental Monitoring XV* **9612** (2015), 96120A.

97. McLinden, C., Bourassa, A., Brohede, S., *et al.* OSIRIS: A decade of scattered light. *Bulletin of the American Meteorological Society* **93,** 1845–1863 (2012).

98. McLinden, C., Olsen, S., Hannegan, B, *et al.* Stratospheric ozone in 3-D models: A simple chemistry and the cross-tropopause flux. *Journal of Geophysical Research: Atmospheres* **105,** 14653–14665 (2000).

99. Mercado, L. M., Bellouin, N., Sitch, S., *et al.* Impact of changes in diffuse radiation on the global land carbon sink. *Nature* **458,** 1014–1017 (Apr. 2009).

100. Metropolis, N. & Ulam, S. The monte carlo method. *Journal of the American statistical association* **44,** 335–341 (1949).

101. Mie, G. Contributions to the optics of turbid media, particularly of colloidal metal solutions (Translated from German). *Ann. Phys. (Leipszig)* **25,** 377–445 (Feb. 1908).

102. Mishchenko, M. I. Vector radiative transfer equation for arbitrarily shaped and arbitrarily oriented particles: a microphysical derivation from statistical electromagnetics. *Applied optics* **41,** 7114–7134 (2002).

103. Murphy, D., Cziczo, D., Hudson, P. & Thomson, D. Carbonaceous material in aerosol particles in the lower stratosphere and tropopause region. *Journal of Geophysical Research: Atmospheres* **112** (2007).

104. Murphy, D., Froyd, K., Schwarz, J. & Wilson, J. Observations of the chemical composition of stratospheric aerosol particles. *Quarterly Journal of the Royal Meteorological Society* **140,** 1269–1278 (2014).

105. Normand, E., Wiensz, J., Bourassa, A. & Degenstein, D. Cloud discrimination in probability density functions of limb-scattered sunlight measurements. *Atmospheric Measurement Techniques* **6,** 3359 (2013).

106. Oman, L., Robock, A., Stenchikov, G., Schmidt, G. A. & Ruedy, R. Climatic response to high-latitude volcanic eruptions. *Journal of Geophysical Research: Atmospheres (1984–2012)* **110** (2005).

107. Palmer, K. F. & Williams, D. Optical constants of sulfuric acid; application to the clouds of Venus? *Applied Optics* **14,** 208–219 (1975).

108. Pitari, G., Aquila, V., Kravitz, B., *et al.* Stratospheric ozone response to sulfate geoengineering: Results from the Geoengineering Model Intercomparison Project (GeoMIP). *Journal of Geophysical Research: Atmospheres* **119,** 2629–2653. ISSN: 2169-8996 (2014).

109. Rasch, P. J., Tilmes, S., Turco, R. P., *et al.* An overview of geoengineering of climate using stratospheric sulphate aerosols. *Philos. Trans. R. Soc. Lond., Ser. A* **366,** 4007–4037 (Nov. 2008).

110. Rasch, P. J., Crutzen, P. J. & Coleman, D. B. Exploring the geoengineering of climate using stratospheric sulfate aerosols: The role of particle size. *Geophys. Res. Lett.* **350,** L02809 (Jan. 2008).

111. Rault, D. F. & Loughman, R. P. The OMPS Limb Profiler environmental data record algorithm theoretical basis document and expected performance. *Geoscience and Remote Sensing, IEEE Transactions on* **51,** 2505–2527 (2013).

112. Ridley, D. A, Solomon, S., Barnes, J. E., *et al.* Total volcanic stratospheric aerosol optical depths and implications for global climate change. *Geophysical Research Letters.* ISSN: 1944-8007. doi:10.1002/2014GL061541 (2014).

113. Rieger, L. A., Malinina, E. P., Rozanov, A. V., *et al.* A study of the approaches used to retrieve aerosol extinction, as applied to limb observations made by OSIRIS and SCIAMACHY. *Atmospheric Measurement Techniques Discussions* **2018,** 1–21 (2018).

114. Rieger, L. A., Bourassa, A. E. & Degenstein, D. A. Stratospheric aerosol particle size information in Odin-OSIRIS limb scatter spectra. *Atmospheric Measurement Techniques* **7,** 507–522 (2014).

115. Rieger, L., Bourassa, A. & Degenstein, D. Merging the OSIRIS and SAGE II stratospheric aerosol records. *Journal of Geophysical Research: Atmospheres* **120,** 8890–8904 (2015).

116. Rienecker, M. M., Suarez, M. J., Gelaro, R., *et al.* MERRA: NASA's modern-era retrospective analysis for research and applications. *Journal of Climate* **24,** 3624–3648 (2011).

117. Robock, A. Volcanic eruptions and climate. *Rev. Geophys.* **38,** 191–220 (2000).

118. Roche, A., Kumer, J., Mergenthaler, J., *et al.* The cryogenic limb array etalon spectrometer (CLAES) on UARS: Experiment description and performance. *Journal of Geophysical Research: Atmospheres* **98,** 10763–10775 (1993).

119. Rodgers, C. D. *Inverse methods for atmospheric sounding: theory and practice* (World scientific, 2000).

120. Rosen, J. M. The Boiling Point of Stratospheric Aerosols. *J. Appl. Meteorol.* **10,** 1044–1045 (Oct. 1971).

121. Rozanov, V., Rozanov, A., Kokhanovsky, A. & Burrows, J. Radiative transfer through terrestrial atmosphere and ocean: software package SCIATRAN. *Journal of Quantitative Spectroscopy and Radiative Transfer* **133,** 13–71 (2014).

122. Russell, P. B. & McCormick, M. P. SAGE II aerosol data validation and initial data use: An introduction and overview. *Journal of Geophysical Research: Atmospheres* **94,** 8335–8338. ISSN: 2156-2202 (1989).

123. Russell III, J. M., Gordley, L. L., Park, J. H., *et al.* The halogen occultation experiment. *Journal of Geophysical Research: Atmospheres* **98,** 10777–10797 (1993).

124. Santer, B. D., Fyfe, J. C., Pallotta, G., *et al.* Causes of differences in model and satellite tropospheric warming rates. *Nature Geoscience* **10,** 478 (2017).

125. Santer, B. D., Bonfils, C., Painter, J. F., *et al.* Volcanic contribution to decadal changes in tropospheric temperature. *Nature Geoscience* **7,** 185 (2014).

126. Sato, M., Hansen, J. E., McCormick, M. P. & Pollack, J. B. Stratospheric aerosol optical depths, 1850-1990. *Journal of Geophysical Research: Atmospheres* **98,** 22987–22994. ISSN: 2156-2202 (1993).

127. Schmidt, A., Mills, M. J., Ghan, S., *et al.* Volcanic radiative forcing from 1979 to 2015. *Journal of Geophysical Research: Atmospheres* (2018).

128. Sheng, J.-X., Weisenstein, D. K., Luo, B.-P., *et al.* Global atmospheric sulfur budget under volcanically quiescent conditions: Aerosol-chemistry-climate model predictions and validation. *Journal of Geophysical Research: Atmospheres* **120,** 256–276 (2015).

129. Soden, B. J., Wetherald, R. T., Stenchikov, G. L. & Robock, A. Global Cooling After the Eruption of Mount Pinatubo: A Test of Climate Feedback by Water Vapor. *Science* **296,** 727–730 (2002).

130. Solomon, S., Daniel, J. S., Neely, R. R., *et al.* The Persistently Variable "Background" Stratospheric Aerosol Layer and Global Climate Change. *Science* **333,** 866–870 (2011).

131. Solomon, S., Garcia, R. R., Rowland, F. S. & Wuebbles, D. J. On the depletion of Antarctic ozone. *Nature* **321,** 755 (1986).

132. Stone, K. A., Solomon, S., Kinnison, D. E., *et al.* Observing the impact of Calbuco volcanic aerosols on South Polar ozone depletion in 2015. *Journal of Geophysical Research: Atmospheres* **122** (2017).

133. Thomas, G. E., Jakosky, B. M., West, R. A. & Sanders, R. W. Satellite limb-scanning thermal infrared observations of the El Chichon stratospheric aerosol - First results. *Geophys. Res. Lett.* **10,** 997–1000 (Nov. 1983).

134. *SPARC Assessment of Stratospheric Aerosol Properties (ASAP)* (eds Thomason, L. & Peter, T.) 322 pp. (SPARC Office, 2006).

135. Thomason, L. W., Ernest, N., Millán, L., *et al.* A global, space-based stratospheric aerosol climatology: 1979 to 2016. *Earth System Science Data Discussions* **2017,** 1–41 (2017).

136. Thomason, L. W. & Vernier, J.-P. Improved SAGE II cloud/aerosol categorization and observations of the Asian tropopause aerosol layer: 1989-2005. *Atmospheric Chemistry and Physics* **13,** 4605–4616 (2013).

137. Thomason, L. W., Burton, S. P., Luo, B.-P. & Peter, T. SAGE II measurements of stratospheric aerosol properties at non-volcanic levels. *Atmospheric Chemistry and Physics* **8,** 983–995 (2008).

138. Thomason, L. W. & Taha, G. SAGE III aerosol extinction measurements: Initial results. *Geophys. Res. Lett.* **30,** 1631 (June 2003).

139. Thomason, L. W., Nicholas, E., Millán, L., *et al.* A global space-based stratospheric aerosol climatology: 1979–2016. *Earth System Science Data* **10,** 469 (2018).

140. Thomason, L. W. & Poole, L. R. Use of stratospheric aerosol properties as diagnostics of Antarctic vortex processes. *Journal of Geophysical Research: Atmospheres* **98,** 23003–23012 (1993).

141. Thomason, L., Moore, J., Pitts, M., Zawodny, J. & Chiou, E. An evaluation of the SAGE III version 4 aerosol extinction coefficient and water vapor data products. *Atmospheric Chemistry and Physics* **10,** 2159–2173 (2010).

142. Thompson, D. W., Wallace, J. M., Jones, P. D. & Kennedy, J. J. Identifying signatures of natural climate variability in time series of global-mean surface temperature: Methodology and insights. *Journal of Climate* **22,** 6120–6141 (2009).

143. Tikhonov, A. N. *On the stability of inverse problems* in *Dokl. Akad. Nauk SSSR* **39** (1943), 195–198.

144. Tilmes, S., Garcia, R. R., Kinnison, D. E., Gettelman, A. & Rasch, P. J. Impact of geoengineered aerosols on the troposphere and stratosphere. *Journal of Geophysical Research: Atmospheres* **114** (2009).

145. Timmreck, C., Mann, G. W., Aquila, V., *et al.* The Interactive Stratospheric Aerosol Model Intercomparison Project (ISA-MIP): motivation and experimental design. *Geoscientific Model Development* **11,** 2581–2608 (2018).

146. Trickl, T, Giehl, H, Jäger, H & Vogelmann, H. 35 yr of stratospheric aerosol measurements at Garmisch-Partenkirchen: from Fuego to Eyjafjallajökull, and beyond. *Atmospheric Chemistry and Physics* **13,** 5205–5225 (2013).

147. Twersky, V. *On propagation in random media of discrete scatterers* in *Proc. Symp. Appl. Math* **16** (1964), 84–116.

148. Twomey, S. Comparison of constrained linear inversion and an iterative nonlinear algorithm applied to the indirect estimation of particle size distributions. *Journal of Computational Physics* **18,** 188 –200. ISSN: 0021-9991 (1975).

149. Vanhellemont, F., Fussen, D., Mateshvili, N., *et al.* Optical extinction by upper tropospheric/stratospheric aerosols and clouds: GOMOS observations for the period 2002-2008. *Atmospheric Chemistry and Physics* **10,** 7997–8009 (2010).

150. Vernier, J.-P., Thomason, L. W., Pommereau, J.-P., *et al.* Major influence of tropical volcanic eruptions on the stratospheric aerosol layer during the last decade. *Geophysical Research Letters* **38,** 10281–10298. ISSN: 1944-8007 (2011).

151. Vernier, J.-P., Fairlie, T. D., Deshler, T., *et al.* In situ and space-based observations of the Kelud volcanic plume: The persistence of ash in the lower stratosphere. *Journal of Geophysical Research: Atmospheres* **121** (2016).

152. Von Savigny, C, Ernst, F, Rozanov, A, *et al.* Improved stratospheric aerosol extinction profiles from SCIAMACHY: validation and sample results. *Atmospheric Measurement Techniques* **8,** 5223–5235 (2015).

153. Wigley, T. M. L. A Combined Mitigation/Geoengineering Approach to Climate Stabilization. *Science* **314,** 452–454 (Oct. 2006).

154. Winker, D. M., Pelon, J., Coakley Jr., J. A., *et al.* The CALIPSO Mission: A Global 3D View of Aerosols and Clouds. *Bulletin of the American Meteorological Society* **91,** 1211–1229 (Sept. 2010).

155. Zawada, D. J., Rieger, L. A., Bourassa, A. E. & Degenstein, D. A. Tomographic retrievals of ozone with the OMPS Limb Profiler: algorithm description and preliminary results. *Atmospheric Measurement Techniques* **11,** 2375–2393 (2018).

156. Zawada, D., Dueck, S., Rieger, L., *et al.* High-resolution and Monte Carlo additions to the SASKTRAN radiative transfer model. *Atmospheric Measurement Techniques* **8,** 2609–2623 (2015).

157. Zawada, D., Bourassa, A. & Degenstein, D. Two-dimensional analytic weighting functions for limb scattering. *Journal of Quantitative Spectroscopy and Radiative Transfer* **200,** 125–136 (2017).

158. Zwally, H., Schutz, B., Abdalati, W., *et al.* ICESat's laser measurements of polar ice, atmosphere, ocean, and land. *Journal of Geodynamics* **34,** 405–445 (2002).

Appendix

Supplementary Information

Table A.1: Data and formats for the OSIRIS 750nm climatology

Parameter Name	Dimensions	Notes
OSIRIS_Extinction_750nm	Latitude × Altitude × Time [36×40×371]	The OSIRIS 750 nm aerosol extinction profiles averaged into 5deg, 1km, monthly bins. No wavelength conversion or bias correction has been applied to this data.
Altitude	kilometers [40×1]	Altitude is the center of the 1km bin.
Latitude	degrees [36×1]	Latitude is the center of the 5 degree bin.
Date/ModifiedJulianDate	Days since Nov. 17, 1858 [371×1]	Date is given as the center of each one month bin. Date information is also provided as year, month, day.

Table A.2: Data and formats for the merged SAGE II OSIRIS 525nm climatology

Parameter Name	Dimensions	Notes
Merged_Extinction_525nm	Latitude × Altitude × Time [36×40×371]	The merged SAGE II, OSIRIS 525 nm aerosol extinction profiles averaged into 5deg, 1km, monthly bins.
Merged_AOD_525nm	Latitude × Time [36×371]	The merged SAGE II, OSIRIS 525 nm aerosol optical depth integrated from 1 km above the 380K potential temperature surface to 35km.
AOD_Flag	Latitude × Time [36×371]	The merged AOD is flagged (true) if the SAGE II or OSIRIS extinction measurements are not available from the tropopause up to 30km. Flagged aod data will be low biased and should be used with caution.
Altitude	kilometers [40×1]	Altitude is the center of the 1km bin.
Latitude	degrees [36×1]	Latitude is the center of the 5 degree bin.
Date/ModifiedJulianDate	Days since Nov. 17, 1858 [371×1]	Date is given as the center of each one month bin. Date information is also provided as year, month, day.

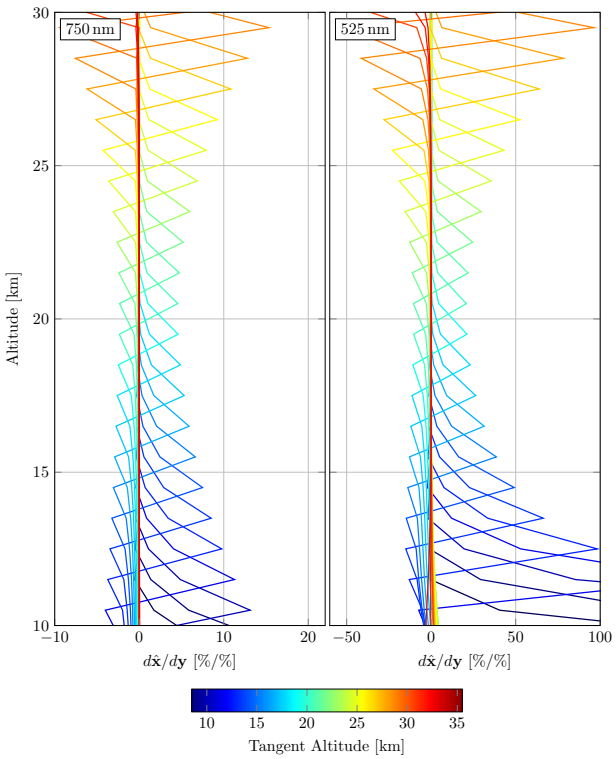

Figure A.1: The left panel shows the gain matrix (retrieved error/radiance error) for a limb scatter retrieval of aerosol at 750 nm. See Bourassa et al. [2007, 2012] reference for details on the retrieval measurement vectors and algorithm. The right panel shows the same results for a retrieval performed at 525 nm. The 525 nm retrieval is much more sensitive to errors in the radiance profile. The color each line represents the tangent altitude of the measurement.

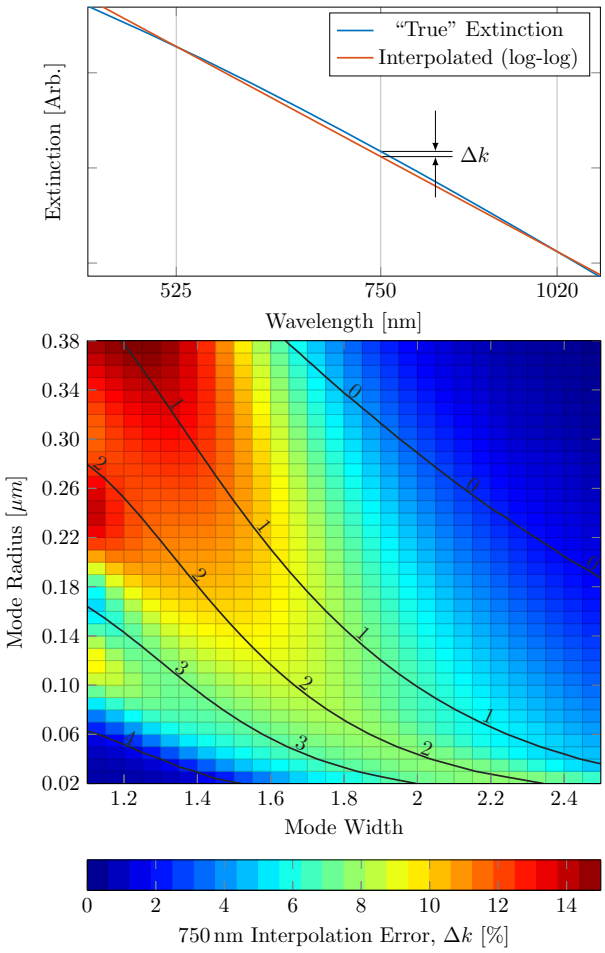

Figure A.2: Panel A shows the extinction as a function of wavelength in blue for a lognormal particle size distribution with a mode radius of 80 nm and mode width of 1.6. The extinction interpolated using an Angstrom coefficient from 525 and 1020 nm wavelengths is shown in red. The interpolated extinction underestimates the "true" extinction by Δk. The magnitude of this underestimation is dependent on the true particle size as shown in panel B. The interpolation error at 750 nm as a function of mode radius and mode width is given by the color scale. The black contours mark lines of constant Ångström coefficient, with typical values lying between 2 and 3 during background conditions.